

Fiber Amplifiers at  $1.5\ \mu\text{m}$  for Laser  
Sources in Next-Generation  
Gravitational Wave Detectors

Der Fakultät für Mathematik und Physik  
der Gottfried Wilhelm Leibniz Universität Hannover

zur Erlangung des akademischen Grades  
Doktor der Naturwissenschaften

**Dr. rer. nat.**

genehmigte Dissertation von

**M.Sc.-Eng. Omar de Varona Ortega**

2018

Referent: Prof. Dr. Detlev Ristau  
Korreferenten: Prof. Dr. Benno Willke  
Prof. Dr. Volker Quetschke  
Tag der Promotion: 11.02.2019

*The Universe behaves like  
a playful child trying  
to hide its secrets*



## Kurzfassung

Nach der ersten direkten Detektion von Gravitationswellen (GW) im Jahre 2015 besteht nun ein großes Interesse daran, die GW-Astronomie als ergänzende Standard-Methode zur Beobachtung astrophysikalischer und kosmologischer Prozesse zu etablieren. Die Weiterentwicklung der GW-Astronomie setzt den Aufbau hochempfindlicher Detektoren voraus. Ein Vorschlag zur Steigerung der Sensitivität künftiger Generationen von Gravitationswellendetektoren (GWD) besteht in der Verwendung kryogenisch gekühlter optischer Komponenten, um so das thermische Rauschen zu reduzieren. Hierzu werden Substrate aus kristallinem Silizium benötigt und infolgedessen Laserstrahlquellen, die bei einer Wellenlänge um  $1,5\ \mu\text{m}$  betrieben werden. Daher ist die Entwicklung von einfrequente Hochleistungsstrahlquellen bei  $1,5\ \mu\text{m}$  mit einem hohen TEM<sub>00</sub>-Modenanteil erforderlich. In der vorliegenden Arbeit werden daher Er<sup>3+</sup>-dotierte und Er<sup>3+</sup>:Yb<sup>3+</sup>-kodierte Faserverstärker (EDFA und EYDFA) für die nächste Generation von GWD untersucht.

Er<sup>3+</sup> ist ein weit verbreiteter Dotand in Faserverstärkern für den Wellenlängenbereich von  $1,5\ \mu\text{m}$  bis  $1,6\ \mu\text{m}$ . Dennoch gibt es bisher kein analytisches Modell, welches die optischen Transferfunktionen unter Berücksichtigung der bei einer Anregungswellenlänge von  $976\ \text{nm}$  beteiligten Energieniveaus (<sup>4</sup>I<sub>11/2</sub>, <sup>4</sup>I<sub>13/2</sub>, <sup>4</sup>I<sub>15/2</sub>) beschreibt. In dieser Arbeit wird daher ein solches Modell für EDFA entwickelt und zur Untersuchung der Verstärkung und der Phasendynamik herangezogen. Die Ergebnisse verdeutlichen den Einfluss strahlungsloser Übergänge in optischen Transferfunktionen und zeigen einen linearen Zusammenhang zwischen der Ausgangsleistung und der effektiven Lebensdauer des metastabilen Energieniveaus <sup>4</sup>I<sub>13/2</sub>. Die Vorhersagen des Modells stimmen mit den experimentellen Messungen überein.

Eine Kodotierung von Er<sup>3+</sup>-dotierten Fasern mit Yb<sup>3+</sup>-Ionen führt zu einer drastischen Verbesserung der Pumplichtabsorption und damit einer höheren optischen Effizienz und Verstärkung. Jedoch sind EYDFA, die bei hohen Pumpleistungen betrieben werden, anfällig für die Ausbildung von verstärkter Spontanemission im Yb<sup>3+</sup> Emissionsband zwischen  $1,0\ \mu\text{m}$  und  $1,1\ \mu\text{m}$ , wodurch die Ausgangsleistung um  $1,5\ \mu\text{m}$  limitiert ist und Instabilitäten entstehen können. In diesem Zusammenhang wurden die Vorteile des sogenannten *off-peak*-Pumpens (also einer Wahl der Pumpwellenlänge neben dem Absorptionsmaximum) untersucht. Ein bei  $940\ \text{nm}$  gepumpter Doppelkern-EYDFA wurde aufgebaut und charakterisiert. Erstmals konnte eine Ausgangsleistung von  $100\ \text{W}$  in der einfrequente, linear polarisierten TEM<sub>00</sub>-Mode bei  $1,5\ \mu\text{m}$  aus einem vollständig monolithischen Faserverstärker demonstriert werden.

Im Vergleich zu mantelgepumpten Systemen kann die Pumplichtabsorption in kerngepumpten Faserverstärkern wegen der optimalen räumlichen Überlappung des Pumplichts mit dem Verstärkungsmedium deutlich verbessert werden. Hierfür werden allerdings einmodige-Pumpdioden benötigt. Die Ausgangsleistung solcher Dioden liegt derzeit bei maximal etwa  $1\ \text{W}$ , sodass auch die Ausgangsleistung von kerngepumpten Faserverstärkern limitiert ist. In der vorliegenden Arbeit wurde erstmals ein Faserlaser bei  $1018\ \text{nm}$  als Pumpquelle für einen kerngepumpten, einfrequente EYDFA mit einer Emissionswellenlänge von  $1556\ \text{nm}$  verwendet. Dieses System wurde ebenfalls *off-peak* mit einer Wellenlänge gepumpt, die oberhalb des Absorptionsmaximums liegt, statt - wie sonst üblich - darunter. Außerdem wurde in einem EYDFA bei  $1,5\ \mu\text{m}$  auch ein Effekt, der dem Photodarkening ähnlich ist, beobachtet. Damit stellt Kernpumpen eine vielversprechende Alternative für einmodige Faserverstärker mit Leistungen von einigen  $10\ \text{W}$  dar.

**Schlagwörter:** Faserverstärker, einfrequente, Gravitationswellendetektor



## Abstract

After the first direct detection of gravitational waves (GWs) in 2015, the feasibility of GW-astronomy as a complementary method to carry out astrophysical and cosmological observations on a regular basis has been reaffirmed. However, ultra-sensitive detectors are required to reliably develop GW-astronomy. A major upgrade proposed to increase the sensitivity of next-generation gravitational wave detectors (GWDs) relies on cryogenically cooling of the optical components to reduce the thermal noise. This upgrade requires the substrate material to be crystalline silicon and this, in turn, requires laser sources at wavelengths above 1.5  $\mu\text{m}$ . In this context, research and development of single-frequency high-power laser sources with high TEM<sub>00</sub> mode content must be carried out. This thesis is focused on the investigation of Er<sup>3+</sup>-doped and Er<sup>3+</sup>:Yb<sup>3+</sup>-codoped fiber amplifiers (EDFAs and EYDFAs) around 1.5  $\mu\text{m}$  for next-generation GWDs.

Er<sup>3+</sup> is widely used as an active dopant in fiber amplifiers in the region between 1.5  $\mu\text{m}$  and 1.6  $\mu\text{m}$  due to its convenient emission spectrum. However, an analytical model to describe its optical transfer functions considering the involved energy levels when pumped at 976 nm (i.e., <sup>4</sup>I<sub>11/2</sub>, <sup>4</sup>I<sub>13/2</sub> and <sup>4</sup>I<sub>15/2</sub>) had not been reported yet. In this thesis, an analytical model to describe the optical-to-optical transfer functions of EDFAs is developed and used to study the gain and phase dynamics of the amplifier. The results prove the influence of the non-radiative transition in the optical transfer functions and a linear relation between the output power and the effective lifetime of the meta-stable energy level <sup>4</sup>I<sub>13/2</sub>. The predictions of the model were in good agreement with the experimental measurements.

When Er<sup>3+</sup>-doped fibers are codoped with Yb<sup>3+</sup>, the pump power absorption is dramatically enhanced, enabling higher optical efficiency and gain levels. However, at high pump power levels, EYDFAs are prone to develop excess amplified spontaneous emission in the Yb<sup>3+</sup> emission band (i.e., between 1.0  $\mu\text{m}$  and 1.1  $\mu\text{m}$ ), which limits the output power at 1.5  $\mu\text{m}$  and can turn the system unstable. In this regard, the benefits of the so-called *off-peak* pumping scheme (i.e., pump at a wavelength different from that of the maximum absorption) were investigated in this thesis. A double-clad EYDFA pumped at 940 nm was built and characterized considering the requirements of GWDs. For the first time, an output power of 100 W in the linearly-polarized TEM<sub>00</sub> mode at 1.5  $\mu\text{m}$  was achieved in single-frequency operation using an all-fiber setup.

Core-pumping fiber amplifiers effectively increases the pump absorption with respect to cladding-pumped systems due to a perfect spatial overlap of the pump light with the gain medium. Nonetheless, it requires single-mode pump sources. To date, single-mode diodes at 9xx nm only provide a maximum power of around 1 W, which relegates the implementation of core-pumped fiber amplifiers to low power systems. In this thesis, a fiber laser at 1018 nm has been used to core-pump a single-mode and single-frequency EYDFA at 1556 nm for the first time. The method is equivalent to an *off-peak* pumping scheme in which the pump wavelength is longer than the maximum absorption peak wavelength rather than shorter. Additionally, a photodarkening-like phenomenon was observed for the first time in an EYDFA at 1.5  $\mu\text{m}$ . The core-pump concept with high pump power levels is a promising alternative for purely single-mode amplifiers up to tens of watts.

**Key words:** Fiber amplifiers, single-frequency, gravitational wave detectors





---

## Contents

---

<b>1</b>	<b>Introduction</b>	<b>1</b>
<b>2</b>	<b>Laser Sources for Interferometric Gravitational Wave Detectors</b>	<b>5</b>
<b>3</b>	<b>Fundamentals of Fiber Amplifiers</b>	<b>11</b>
3.1	Optical Fibers as Waveguides . . . . .	11
3.2	Er <sup>3+</sup> -Doped Fiber Amplifiers . . . . .	13
3.3	Er <sup>3+</sup> :Yb <sup>3+</sup> -Codoped Fiber Amplifiers . . . . .	17
3.4	Limitations in Single-Frequency Fiber Amplifiers . . . . .	19
3.4.1	Yb <sup>3+</sup> -band Amplified Spontaneous Emission . . . . .	19
3.4.2	Stimulated Brillouin Scattering . . . . .	20
<b>4</b>	<b>Gain Dynamics of Er<sup>3+</sup>-Doped Fiber Amplifiers</b>	<b>23</b>
4.1	Analytical Model . . . . .	23
4.2	Experiments . . . . .	28
4.2.1	Pump-to-Signal Transfer Function . . . . .	28
4.2.2	Pump-to-Phase-Shift Transfer Function . . . . .	31
4.2.3	Summary . . . . .	34
4.3	Further Analysis Using the Model . . . . .	35
4.4	Conclusion . . . . .	39
<b>5</b>	<b>Off-Peak Pumped High Power Fiber Amplifier Oriented to Next-Generation GWDs</b>	<b>41</b>
5.1	Simulations . . . . .	42
5.2	Experiments . . . . .	44
5.2.1	Optical Slope and Spectrum . . . . .	46
5.2.2	Power and PER Stability . . . . .	46
5.2.3	Modal Content Analysis . . . . .	47
5.2.4	Relative Power Noise . . . . .	50
5.2.5	Frequency Noise . . . . .	51
5.2.6	Stimulated Brillouin Scattering . . . . .	52
5.3	Conclusion . . . . .	53
<b>6</b>	<b>Er<sup>3+</sup>:Yb<sup>3+</sup>-Codoped and Er<sup>3+</sup>-Doped Fiber Amplifiers Core-Pumped at 1018 nm</b>	<b>55</b>
6.1	Experimental Setup . . . . .	56

---

6.2 Mid-Power Fiber Amplifier . . . . .	58
6.3 Low-Power Fiber Amplifier . . . . .	61
6.4 Er <sup>3+</sup> -Doped Yb <sup>3+</sup> -Free Fiber Amplifier Pumped at 1018 nm . . . . .	62
6.5 Conclusion . . . . .	64
<b>7 Summary and Outlook</b>	<b>67</b>
<b>Bibliography</b>	<b>69</b>
<b>Publications</b>	<b>81</b>
<b>Curriculum Vitae</b>	<b>85</b>

# CHAPTER 1

---

## Introduction

---

In 1916 Albert Einstein predicted the existence of gravitational waves within the theory of general relativity [Ein16]. Gravitational waves can be described as wave-like ripples in the space-time lattice that propagate away from their source at the speed of light. Although in theory any mass in motion with variable acceleration can produce GWs (excluding spherically and rotationally symmetric motion), only very powerful events can radiate a significant amount of energy as gravitational waves. These events usually involve the interplay between large masses gravitationally bound such as binary systems composed by black holes or neutron stars that eventually merge. Some other events, like the formation of cosmic structures in the early universe shortly after the Big Bang, supernovae explosions and certain processes in fast-rotating massive bodies such as pulsars are believed to produce GWs as well. Unlike photons, gravitational waves interact very weakly with matter and can travel very long distances practically unchanged. This is an important characteristic to consider GW astronomy as a revolution in the understanding of the universe because GW sources hidden behind electromagnetically opaque cosmic structures can still be observed and provide information about these regions. By extension, the early universe should have been transparent to GWs, which could allow the study of the inflationary era, as early as  $10^{-36}$  to  $10^{-32}$  seconds after the Big Bang, i.e., the cosmic background of GWs, in a similar way that cosmologists do with the cosmic microwave background originated 380.000 years after the Big Bang.

First attempts to setup a gravitational wave detector were based on resonant metallic bars [Web60]. In 1966, Joseph Weber built a detector consisting of a 3 tons aluminum cylinder hanging from steel wires in a vacuum chamber. Any loud enough gravitational wave impinging on the cylinder would excite mechanical resonances that would be detected by an array of piezoelectric sensors attached to it. Later in the 1990s, a more sophisticated version of Weber's apparatus called ALLEGRO started operating at cryogenic temperatures. ALLEGRO was decommissioned in 2008 without any detection. Interferometric GWDs were first proposed in the 1970s as a very precise method to detect gravitational waves by measuring the small length differences caused by the space strain when a wave passes [Sab70; Wei72]. Nevertheless, they were not available until the end of the 1990s, when TAMA300 started observing. The Japanese GWD TAMA300 was an L-shaped Michelson interferometer which collected data from 1999 to 2004. Later, CLIO (Cryogenic Laser Interferometer Observatory) was the first interferometric detector to use cryogenic technology, paving the way to integrate this technology in future detectors. During the first decade of the 2000s the detectors GEO600 (Hannover, Germany), LIGO (Large Inter-

ferometer Gravitational-Wave Observatory composed of two twin detectors in Hanford and Livingston, USA) and Virgo (Cascina, Italy) simultaneously performed observation runs. After a major upgrade, 2<sup>nd</sup>-generation LIGO detectors (also denominated Advanced LIGO) started operating in 2015, detecting the first direct evidence of gravitational waves in the history the same year [Abb16]. The 2<sup>nd</sup>-generation Virgo detector (also called AdVirgo) operates in conjunction with LIGO and GEO600 since 2017.

Although interferometric GWDs have demonstrated the feasibility of direct detections of gravitational waves, only few events per year are believed to be strong enough to become detectable by the 2<sup>nd</sup>-generation detectors and, besides this, more detectors distributed at different locations around the world are needed to precisely identify the wave's direction. Hence, more sophisticated observatories are necessary to enable precise astronomical investigations. In this context, the Kamioka Gravitational Wave Detector (KAGRA) is under construction in Japan. This 2G detector has two 3 km-long arms and sapphire test mirrors cryogenically cooled at 20 K. KAGRA's laser system will probably consist of two fiber amplifiers coherently combined to deliver  $\sim 80$  W at 1064 nm followed by a solid-state amplifier [Nis14]. Future gradual upgrades of LIGO are also planned: first, LIGO A+ will implement frequency dependent squeezing and new coating technology for the mirrors, among other noise isolation systems. Then, LIGO Voyager will push the sensitivity across the audio-band with a myriad of advanced techniques such as cryogenic cooling systems, new substrate materials and higher laser power at longer wavelength. LIGO's roadmap for future detectors includes the 3<sup>rd</sup>-generation observatory Cosmic Explorer (CE), in which the developed technology in the 2G detectors will be integrated in a totally new facility. CE will use a xylophone strategy with 40 km-long arms, and it is estimated to start operating not before 2035 [Col17]. In this thesis, the 3G observatory taken as a reference is the Einstein Telescope (ET) due to its much more advanced conceptual design status [Tea11]. The topology considered for ET in the conceptual design is a xylophone of 3 pairs of interferometers with 10 km-long arms. Three interferometers will operate at 1064 nm and use fused silica mirror substrates at room temperature to optimize the sensitivity between 10 Hz and  $10^4$  Hz (ET-HF), while the other three interferometers will operate around 1550 nm with silicon mirror substrates at cryogenic temperatures to optimize the sensitivity in the band from 1 Hz to 250 Hz (ET-LF).

A great effort is being made to develop cryogenic technologies for GWDs. However, the R&D required to integrate it in 3G observatories is much more profound than developing the cooling systems. Since fused silica has a low mechanical quality factor at low temperature, a different material must be used for the test masses' substrate [Sch09]. Silicon, in turn, has a much better behavior at cryogenic temperatures and is available in large pieces and high purity. However silicon has too high residual absorption at 1064 nm [Gre95], reason why laser sources at wavelengths larger than 1500 nm are required for next-generation GWDs. Although the laser technology at 1550 nm has dramatically evolved due to relevant industrial and telecommunications applications in the last decades, the exceptional requirements of GWDs demand further research. The detailed requirements of lasers for next-generation GWDs are not fully specified yet, but a suitable laser source must have, among other properties, a very low linewidth, e.g., few kHz, linear polarization and very low intensity noise. Besides this, since GWDs are designed to be resonant for pure  $TEM_{00}$  transversal

modes, any amount of power in higher order modes (HOMs) is filtered out by input mode cleaners and therefore cannot reach the interferometer. Moreover, since the detectors are expected to work for long periods of time without interruptions, long-term stability is important.

This thesis covers important aspects of laser sources for next-generation GWDs. In Chapter 2 the role of the laser source in a GWD is explained and the influence of its most important characteristics is described. The key limitations of the lasers in the current generation are introduced and fiber-based systems are proposed as an alternative to address the requirements of the next generation. The following chapters are dedicated to discuss in more details the operation of fiber amplifiers and present the experimental studies carried out on gain dynamics and power scaling.



# CHAPTER 2

---

## Laser Sources for Interferometric Gravitational Wave Detectors

---

Since GWs alter the space-time as they propagate, the distance between objects changes. To measure this effect, interferometric GWDs are L-shaped Michelson laser interferometers that continuously monitor the length difference between the arms. When a GW passes through the detector, it temporarily stretches one arm while shrinking the other. The way the detector monitors these changes in the lengths difference is the following: A laser beam is coupled into the interferometer and split in two equal parts by a beam splitter. Each beam travels through an arm and is reflected back by a mirror at the end of it. When the two beams are combined again at the beam splitter, they interfere in a way that depends on their differential phases and, therefore, on the difference between the arms lengths. The intensity fluctuations of the resulting interference beam are sensed with a photodiode and the temporal trace is recorded for posterior (or real time) analysis. Although this concept is simple, reaching the sensitivity to detect the small strain levels caused by GWs (which are in the order of  $10^{-22}$ ) is a major challenge. A large amount of sensors, actuators and systems are deployed to monitor, counteract and reduce a variety of noise sources. For this reason, GWDs require carefully and tailored designed subsystems with specific characteristics. Regarding the topic at hand, the laser source must address diverse requirements that, even if these are not concisely specified yet, will be over the state of the art for future detectors. The influence of the most relevant characteristics of the laser source in a GWD is summarized below.

### POWER

One of the key phenomena limiting the sensitivity of GWDs is the quantum noise. It is a direct manifestation of the Heisenberg uncertainty principle and is comprised of the photon shot noise (dominant at high frequency) and the radiation pressure noise (dominant at low frequency). The relative shot noise, i.e., the uncertainty in the photons' arrival time, decreases with the square root of the optical power, whereas the radiation pressure noise, i.e., motion of the detector's mirrors exerted by the photons, increases with optical power. Therefore, a critical trade-off arises here. On the one hand, a high laser power to reduce the shot noise enhances the sensitivity of the detector in the high frequency range, but on the other hand too high power would induce noise due to radiation pressure, which has a negative impact at low frequency. For this reason, ET-LF is designed to work with few watts at  $1.5\ \mu\text{m}$ . However one can expect further suppression of the radiation pressure in future upgrades (e.g., by increasing the weight of the test masses) that would allow the use of lasers with higher power to further enhance the high frequency sensitivity without compromising the low frequency range. Besides this, other future detectors such

as LIGO-Voyager and Cosmic Explorer might be designed to work with high power lasers at  $1.5\ \mu\text{m}$ , especially considering that the low frequency detection range will be covered by future space-borne detectors such as eLISA and DECIGO. The future need of much more power at  $1.5\ \mu\text{m}$  seems likely if we stick to the evolution of the power required by detectors working at  $1\ \mu\text{m}$ , which started with few watts and nowadays require hundreds of watts.

#### BEAM QUALITY

All interferometric GWDs use Fabry-Pérot cavities inside the arms to boost the circulating optical power. These cavities are resonant to the fundamental transversal mode  $\text{TEM}_{00}$ . This fact adds an important constraint to the laser source, which should provide the required power level in that mode. Right before the interferometer, the laser beam is filtered in the so-called pre-mode cleaner (PMC) to ensure that no higher order modes (HOMs) enter the interferometer. Similarly, fluctuations in the modal content are converted in power fluctuations after the PMC even if the power fluctuations before the PMC are very low. Thus, not only high fundamental mode content is desired, but also a reasonable modal stability.

#### POLARIZATION

The properties of the optical components in the interferometer, mode cleaners and other optical systems in GWDs depend on the polarization state of the light. For example, the reflectivity of the mirrors is not exactly the same for  $s$  and  $p$  polarizations. This is especially important for the beamsplitter inside the interferometer because the splitting ratio might not be the same for different polarizations. Apart from this, any fluctuation in the polarization state would be converted into intensity fluctuations in the interferometer due to arms lengths mismatch. To avoid all these problems, the detector requires linearly polarized light.

#### RELATIVE POWER NOISE

The relative power noise (RPN), sometimes also called relative intensity noise (RIN), are the fluctuations of the optical power of the laser beam with respect to its average value. This noise couples to the read-out signal of the photodetector of the interferometer in GWDs. The origin of this noise is usually noise of the pump and/or the seed sources of the laser system, and is important to understand how it couples to the output beam to effectively mitigate it. The laser system must permit the integration of stabilization systems to compensate the RPN via, for example, amplitude modulators or current feedback loops.

#### FREQUENCY NOISE

One of the subsystems in which more efforts are made regarding laser systems for GWDs is the frequency stabilization. This is because frequency noise (FN) induces power noise once the beam is split in the interferometer due to small inequalities in the lengths of the arms, causing power fluctuations that are indistinguishable from a GW. Even in a hypothetical interferometer with perfectly matching arms lengths, the frequency noise would cause additional power noise when a GW change the arms lengths difference. Then, it is important that the seed source of the laser system has a low linewidth, as well as that the amplifying stages maintain this property. Also, similarly to the RPN, the laser source



must provide a way to actuate on its frequency to permit locking to a stable reference.

#### STABILITY

GWDs should work for long periods (ideally years) without interruptions. Therefore, the laser power level should not drift nor fluctuate. Once more, stabilization systems are set to compensate long term fluctuations as well, but the free-running behavior of the laser source must be characterized in advance to properly design the power fluctuations control system. More critical is the presence of long-term drifts like unrecoverable power drifts due to, for example, diodes aging or photodarkening effects, because at some point stabilization loops can run out of gain to compensate them.

#### COMPLEXITY

Even before engineering stages in the developing process, the complexity of the final laser system must be taken into account. In case of failure, it should be relatively easy and fast to identify and repair the issue. From a practical point of view, the systems like thermal management, monitor ports or diagnostics features should be able to provide all the needed information to minimize the down-times. Ideally, individual components should be available from different providers to prevent scarcity of spare parts if needed and their replacement should not require highly specialized procedures. In addition, given the timeframe the detectors are expected to be operative, the architecture should be upgradeable.

The first and the second generation of GWDs have implemented free-space solid state laser (SSL) sources. In aLIGO, for example, a Nd<sup>3+</sup>:YAG non-planar ring oscillator (NPRO) with an output power of 2 W is amplified in a master oscillator power amplification (MOPA) system to 35 W with a 4-stage Nd:YVO amplifier and then injection locked to a Nd:YAG oscillator to over 220 W [Win11]. This configuration presents serious drawbacks to be further power scaled such as high complexity of the thermal management, thermal lensing effects and considerable jitter noise. Besides this, the alignment process becomes overly complex and it is not possible to run it at any desired output power point along the slope, but only at the nominal output power. In this context fiber technology has become very attractive after its evolution in the last decade. In fact, as mentioned earlier in Chapter 1, it is planned to use two Yb<sup>3+</sup>-doped fiber amplifiers coherently combined in KAGRA to boost the power from an NPRO up to 80 W. Fiber systems have attractive features for GWDs. On the one hand they are alignment-free, have virtually no thermal lensing and can be designed to favor the desired beam quality [Bro99]. Furthermore, because of the high surface-to-volume ratio, the thermal management of optical fibers can be performed efficiently with relatively simple cooling systems. Single-frequency high power YDFAs at 1064 nm oriented to GWDs have been reported with an output power of 158 W using core-pump configuration [The16], and 300 W in cladding-pump configuration [The12a]. On the other hand, the power scaling of fiber amplifiers is not free of challenges. Due to the high intensities in the core and the relatively long interaction lengths, high power systems are often limited by the onset of nonlinearities, of which the stimulated Brillouin scattering (SBS) is particularly harmful [Lie03], and amplified spontaneous emission (ASE). To overcome these limitations and permit higher power levels many types of large mode

area (LMA) fibers have been developed in the last decade. By increasing the core size the threshold of nonlinearities is increased. To maintain single-mode operation in LMA fibers, the numerical aperture (NA) must be lowered. Active fibers with NAs as low as 0.06 are widely commercialized and even lower NAs can be fabricated, but at some point further reduction of the NA is technically impossible and increasing the fiber's mode area makes the amplifier prone to guide higher order transversal modes and modal instability (MI) issues can come into play [War12]. Some smartly designed specialty fibers like photonic bandgap fibers (PBG), leakage channel fibers (LCF) or chirally coupled cores (CCC) fibers have demonstrated excellent performances dealing with nonlinearities at high intensities [Che10; Don09; Ola10], but their manipulation (e.g., cleaving, splicing or tapering) is usually very complex and no commercial instrument can handle it. Hence, the manufacture of fiber components matching such specialty fibers is very challenging, which is why these components are not commercialized. This leads to free-space parts in systems based on such fibers, loosing some of the advantages of fiber technology.

Unlike in laser sources at  $1\ \mu\text{m}$ , around  $1.5\ \mu\text{m}$  there are no multi-watts seeders with single-frequency and single-mode polarized output commercially available. Thus, the amplifier must deal with significantly low input seed power levels or a preamplifier stage must be included. In amplifiers between  $1.5\ \mu\text{m}$  and  $1.6\ \mu\text{m}$ ,  $\text{Er}^{3+}$  is used as active dopant due to its convenient emission spectrum.  $\text{Er}^{3+}$  presents an absorption about 10 times lower than that of  $\text{Yb}^{3+}$  at  $976\ \text{nm}$ , besides a significantly high quantum defect. For these reasons, the development of high power EDFAs at  $1.5\ \mu\text{m}$  has been less prominent than high power YDFAs at  $1\ \mu\text{m}$ . The  $\text{Er}^{3+}$  low absorption represents a great challenge when designing high power amplifiers with single-frequency operation since neither the use of longer active fibers nor the increase of the  $\text{Er}^{3+}$  concentrations to achieve higher absorption are good solutions. The first leads to a strong lowering of the SBS threshold, while the latter produces quenching effects due to the tendency of  $\text{Er}^{3+}$  ions to cluster in high concentrations, worsening the optical efficiency among other detrimental effects [Nil93]. An interesting strategy to achieve higher doping concentration before clustering becomes relevant is to use phosphate-based host material instead of silica-based (e.g., phosphosilicates or aluminophosphosilicates) [Jia03]. However, such compounds exhibit important differences in the mechanical and chemical properties that constitute compatibility issues, particularly when integrating in all-fiber setups where silica-based fibers already exist. A much exploited method to power scale fiber amplifiers in C-band (i.e., from  $1530\ \text{nm}$  to  $1565\ \text{nm}$ ) is to codope EDFAs with  $\text{Yb}^{3+}$ .  $\text{Er}^{3+}:\text{Yb}^{3+}$ -codoped fiber amplifiers (EYDFAs) benefit from a much higher absorption at  $976\ \text{nm}$  than EDFAs due to the higher  $\text{Yb}^{3+}$  absorption cross section. In addition,  $\text{Yb}^{3+}$  also behaves as a solvent for  $\text{Er}^{3+}$ , increasing its solubility and allowing higher  $\text{Er}^{3+}$  doping concentrations [Kir15]. This enables higher optical efficiencies and output power levels in shorter fiber lengths but introduces the new limitation of  $\text{Yb}^{3+}$ -band ASE (i.e.,  $\text{Yb}^{3+}$  amplified spontaneous emission between  $1\ \mu\text{m}$  and  $1.1\ \mu\text{m}$ ). The power scaling of EYDFAs is a very active object of research and many techniques such as co-seeding [Ste14a] and resonant pumping of  $\text{Er}^{3+}$  [Jeb14; Sup12] have been proposed to mitigate  $\text{Yb}^{3+}$ -band ASE.

The gain dynamics of EYDFAs has been studied in [Ste15]. It was found that a full analytical solution for the optical transfer functions does not exist, and it is necessary to resort to numerical analysis to solve the system. Although  $\text{Er}^{3+}:\text{Yb}^{3+}$  systems cannot be

---

modelled as a mere combination of only- $\text{Er}^{3+}$  and only- $\text{Yb}^{3+}$  ones, studying  $\text{Er}^{3+}$  and  $\text{Yb}^{3+}$  systems separately can help to understand EYDFAs up to some extent skipping its complexity. The case of YDFAs has been thoroughly studied in [Tün12c]. In the Chapter 4 of this thesis the gain dynamics of EDFAs is studied and an analytical model of the optical transfer functions is reported for the first time. In Chapter 5 the *off-peak* pumping technique is investigated as a method to improve the  $\text{Yb}^{3+}$ -to- $\text{Er}^{3+}$  energy transfer efficiency to reduce  $\text{Yb}^{3+}$ -band ASE [Cre16]. It is applied to a high power laboratory prototype EYDFA oriented to GWDs. The experiment demonstrated for the first time an all-fiber EYDFA with more than 100 W in the linearly-polarized  $\text{TEM}_{00}$  mode. This is a very promising result and invites to keep investigating this technique. From these results, a new idea pops up: to apply the *off-peak* pumping technique at a wavelength that could be generated at high power in the core of a purely single-mode fiber. The goal is to investigate whether the benefits of both strategies, i.e., *off-peak* and core-pumping, can be combined in an all-fiber and purely single-mode amplifier at 1.5  $\mu\text{m}$ . This experiment is presented in Chapter 6. The results demonstrate a performance comparable to similar systems pumped at the maximum absorption wavelength but with different limitations that could, in principle, be tackled by a variety of approaches. Within this experiment, an evidence of photodarkening in EYDFAs at 1.5  $\mu\text{m}$  has been observed for the first time.



# CHAPTER 3

## Fundamentals of Fiber Amplifiers

This chapter introduces important concepts and characteristics of single-frequency fiber amplifiers in four sections. The first provides the fundamental theory of light guidance in optical fibers and briefly explains the main fabrication process. In the second and third sections, the operation principle of  $\text{Er}^{3+}$ -doped and  $\text{Er}^{3+}:\text{Yb}^{3+}$ -codoped fibers is described, including the physical mechanisms occurring during their operation in amplifiers. Besides this, the corresponding rate equations governing these mechanisms are presented. The fourth section is dedicated to the most important limiting effects hindering the power scaling of single-frequency fiber amplifiers around  $1.5\ \mu\text{m}$ .

### 3.1 Optical Fibers as Waveguides

The simplest type of optical fiber consists of a glass cylinder with refractive index  $n_1$  surrounded by a material with lower a refractive index  $n_2$ . In practice this is made, for example, by surrounding a silicate core with a pure silica layer. In such step index fiber, the light is confined in the core due to the total internal reflection effect. This is illustrated in

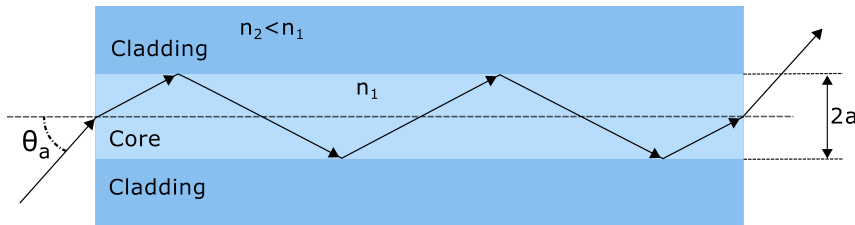


**Figure 3.1:** Illustration of the total reflection effect in a step-index optical fiber.  $n_1$  is the refractive index of the material and  $a$  is the radius of the core.

Fig. 3.1. One of the most important parameters that characterize a fiber is its numerical aperture (NA), which is defined as

$$\text{NA} = \sin(\theta_a) = \sqrt{n_1^2 - n_2^2}, \quad (3.1)$$

where  $\theta_a$  is half of the angle of acceptance (i.e., maximum angle respect to the longitudinal axis of the fiber at which the light is guided) and  $n_1$  and  $n_2$  are the refractive indices of the core and the cladding respectively. The typical core diameter of optical fibers is in the range from few to tens of micrometers. This is small enough to support the guidance of a finite number of transversal modes for a given frequency  $\omega$ , whose spatial distributions are

solutions of the Helmholtz wave equation, given in cylindrical coordinates as [Agr07]

$$\frac{d^2 u_m(r)}{dr^2} + \frac{1}{r} \frac{du_m(r)}{dr} + \left( n^2(r) k_0^2 - \beta^2 - \frac{m^2}{r^2} \right) u_m(r) = 0, \quad (3.2)$$

where  $r$  is the radial distance from the center of the fiber core,  $u_m(r)$  is the discrete transversal mode distribution,  $n(r)$  is the refractive index profile,  $\beta$  is the propagation constant,  $k_0$  the wavenumber and  $m$  an integer index. Eq. 3.2 is a differential equation for Bessel functions that gives rise to a set of Bessel functions  $u(r) = J_m(r f(\beta, k_0, n_1))$  and modified Bessel functions  $u(r) = K_m(r g(\beta, k_0, n_2))$  for the core and the cladding. The solutions exist only for discrete values of the propagation constant  $\beta_{m,n}$ , where  $m$  and  $n$  are integers, leading to a limited number of electric field distributions that can be guided in the fiber, the so-called LP<sub>mn</sub> modes.

A single-mode fiber (SMF) is a fiber that only guides the LP<sub>01</sub> mode, namely the fundamental mode. The solution of the transversal mode distribution,  $u(r)$ , depends on the wavenumber  $k_0$ , and therefore on the wavelength  $\lambda = 2\pi/k_0$ , such that there is a shortest wavelength at which the fiber can still be single-mode. This is called the *cut-off* wavelength,  $\lambda_c$ , and is an important characteristic that manufacturers can tune via the design parameters of core radius,  $a$ , and refractive index difference  $\Delta = n_1 - n_2$ . In this regard, a very useful parameter called the *normalized frequency* is defined as

$$V = k_0 a \sqrt{n_1^2 - n_2^2} = \frac{2\pi}{\lambda} a \text{NA}, \quad (3.3)$$

where  $a$  is the core radius.

It can be shown that the normalized frequency, or simply V-number, is approximately 2.405 when  $\lambda = \lambda_c$  [Yeh90]. Thus, a step-index fiber is single-mode when  $V \leq 2.405$ . Another important characteristic in single-mode fibers is the mode field diameter (MFD). The MFD defines the  $1/e^2$  diameter of the intensity distribution of the fundamental mode and is used to determine some practical parameters such as splicing loss, bending loss, etc. It can be expressed as [Trä07]

$$\text{MFD} \simeq 2a \left( 0.65 + \frac{1.619}{V^{3/2}} + \frac{2.879}{V^6} \right) \quad \text{for } 0.8 \leq V \leq 2.5. \quad (3.4)$$

Single-mode fiber lasers and amplifiers can be made by pumping laser-active fibers at the proper wavelength. However to pump the core of a single-mode fiber, a single-mode pump source, e.g., a fiber-coupled pump diode, must be used. State-of-the-art single-mode fiber coupled pump diodes at, for example, 976 nm can deliver around 1 W, which hinders the realization of high power systems. To overcome this limitation, an extra layer (namely the coating) with refractive index  $n_3 < n_2$  can be used to surround the cladding and provide the capability to guide multi-mode light in it. By doing this, multi-mode pump sources can be used instead of single-mode, enabling much higher pump power levels. Such fibers are called double-clad fibers and are widely used in both single-mode and multi-mode systems where cladding-pumping is required. The trade-off of this pumping method is a

significantly lower pump absorption per unit length compared to core-pumped systems. This is due to the lower overlap between the pump light in the cladding and the active media confined in the core.

The most common material used in the fabrication of optical fibers is SiO<sub>2</sub> due to its optical and mechanical properties, availability and price. The different refractive indices of the core and cladding are achieved by adding dopants to the SiO<sub>2</sub> host. Dopants such as GeO<sub>2</sub>, P<sub>2</sub>O<sub>5</sub> and Al<sub>2</sub>O<sub>3</sub> are used to rise the refractive index of the core, while B<sub>2</sub>O<sub>3</sub> and F can be used to lower it in the cladding [Kyo93; Yeh90]. The investigations of new dopants and different combinations and concentrations of them attract a lot of attention because they have a high impact on a number of characteristics of the fiber, e.g., the mechanical and thermal properties, the solubility of other dopants or the resistance to ionizing radiation. Fiber lasers and amplifiers require active fibers, also called gain fibers, which are doped with rare-earth ions to provide gain to the fiber. The specific rare-earth dopant depends on the desired emission spectrum. Common examples are Yb<sup>3+</sup> if gain between 1 μm and 1.1 μm is desired, Er<sup>3+</sup> if the output is between 1.5 μm and 1.6 μm, Tm<sup>3+</sup> for emission between 1.7 μm and 2.1 μm and Ho<sup>3+</sup> if the band of interest is around 2.1 μm.

The fabrication of optical fibers involves two main processes. The first is the fabrication of the preform with the same composition and structure of the final fiber but with a larger diameter of a few centimeters. The most common method to produce the preform is the *Modified Chemical Vapor Deposition* (MCVD)[Yeh90]. It consists on vaporizing the materials inside a hollow SiO<sub>2</sub> tube while heating it with a flame moving longitudinally to make the soot deposit on the inner surface. The second process consists on drawing and coating the fiber from the preform. This is done in so-called fiber drawing towers. The preform is fed at the top of the tower to take advantage of the gravitational force. It passes through a furnace while shrunk in diameter and extended in length by controlled forces. A variety of parameters can be monitored in real time to adjust the pulling speed and/or the temperature of the furnace. Once the fiber has the designed diameter, it passes through the coating stage, where is coated with a curable polymer whose properties depend on the application for which the fiber is meant (e.g., low index polymer for double-clad fibers).

### 3.2 Er<sup>3+</sup>-Doped Fiber Amplifiers

Er<sup>3+</sup>-doped fiber amplifiers consist of a combining device that merges the light from a pump laser source and a seed laser source into the active fiber. Essentially, the Er<sup>3+</sup> ions present in the fiber absorb energy at the pump wavelength and reemit it at the seed wavelength. The physical mechanisms occurring at the atomic level are rather complex and must be modelled from a quantum point of view as a set of absorption and emission spectral structures defined by atomic probability distributions. These processes are described by the Judd-Ofelt theory [Jud62; Ofel62] and the details are out of the scope of this thesis. A diagram of the most important electronic energy levels and transitions of Er<sup>3+</sup> is shown in Fig. 3.2. The Stark splittings of each energy level strongly depend on the material in which the Er<sup>3+</sup> ions are hosted. For this reason the energy of the individual absorption and emission transitions between the Stark splitted electronic energy levels, and consequently the corresponding absorption and emission spectra, can vary significantly from fiber to fiber. The transitions of interest when amplification around 1.55 μm is desired is that from

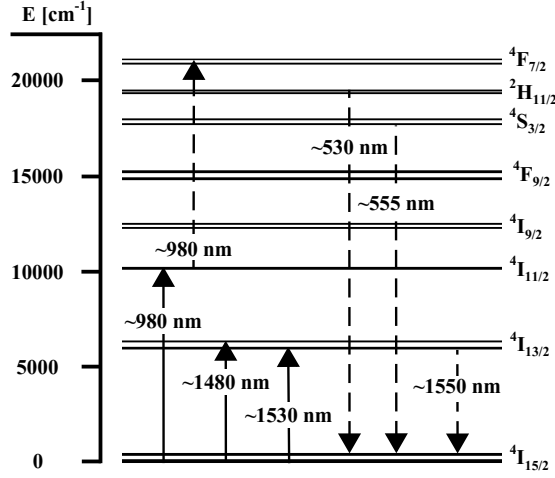


**Figure 3.2:** Most relevant energy levels and transitions in an Er<sup>3+</sup>-doped fiber at C-band. Solid lines represent the most common pumped transitions and dashed lines represent spontaneous transitions.

the energy level  ${}^4I_{13/2}$  to the ground energy level  ${}^4I_{15/2}$ . Depending on the Stark splits, the emission wavelength can be as long as  $1.6 \mu\text{m}$  [Bec99].

Er<sup>3+</sup>-doped fiber amplifiers are commonly pumped around 980 nm due to the relatively high absorption at this wavelength, which actually pumps the ground energy level  ${}^4I_{15/2}$  to the  ${}^4I_{11/2}$ . The excited ions relax to the state  ${}^4I_{13/2}$  after  $\sim 9 \mu\text{s}$  [Lay77] via a nonradiative process that releases multiple phonons responsible of heating the fiber. The lifetime of the metastable state  ${}^4I_{13/2}$  is  $\sim 10 \text{ ms}$  [San93]. Then, the ions spontaneously relax to the ground state by emitting photons around  $1.55 \mu\text{m}$ . The  ${}^4I_{13/2} \rightarrow {}^4I_{15/2}$  transition can be stimulated by seeding the amplifier, in which case the effective lifetime becomes shorter, the higher the output power is [Var16].

The absorption and emission spectra of an Er<sup>3+</sup>-doped fiber amplifier are determined by the absorption and emission cross sections, labelled  $\sigma^{\text{abs}}$  and  $\sigma^{\text{em}}$  respectively, as:

$$P_{\text{abs}}(\lambda) = \sigma^{\text{abs}}(\lambda) I(\lambda) (\beta - 1)p \quad (3.5a)$$

$$P_{\text{em}}(\lambda) = \sigma^{\text{em}}(\lambda) I(\lambda) \beta p, \quad (3.5b)$$

where  $P_{\text{abs}}(\lambda)$  and  $P_{\text{em}}(\lambda)$  are the absorbed and emitted power levels at a given wavelength,  $I(\lambda)$  is the optical intensity per unit area and  $\sigma^{\text{abs}}$  and  $\sigma^{\text{em}}$  are the absorption and emission cross sections of the fiber, which are proportional to the probability of their corresponding atomic transitions,  $\beta$  is a parameter between 0 and 1 that represents the ion inversion level (i.e., the number of excited ions with respect to the total number of ions), and  $p$  is the doping concentration. The cross sections of a typical Er<sup>3+</sup>-doped aluminosilicate fiber are shown in Fig. 3.3 (a).

Looking at Fig. 3.3 (a), one can expect the gain spectra not to be flat, but spectrally shaped depending on the emission and absorption cross sections. Indeed, a simplified



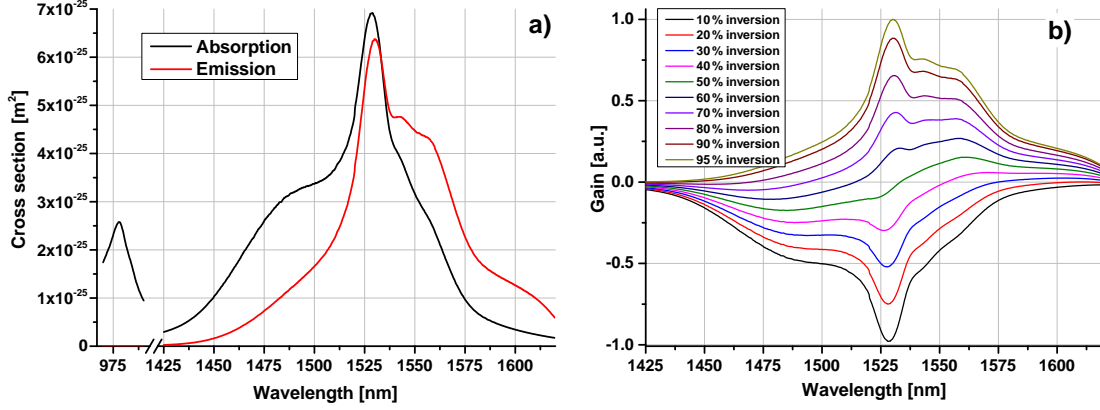


**Figure 3.3:** (a): Er<sup>3+</sup> absorption and emission cross sections. (b): Normalized gain spectra in an Er<sup>3+</sup>-doped amplifier for different inversion levels.

expression of the gain spectrum is

$$g(\lambda) = \left( \beta \sigma^{\text{em}}(\lambda) - (1 - \beta) \sigma^{\text{abs}}(\lambda) \right) pL, \quad (3.6)$$

where  $L$  is the length of the active fiber. The gain spectra at different inversion levels are depicted in Fig. 3.3 (b).

It seems logical to think that the gain of Er<sup>3+</sup>-doped fibers increases with the doping concentration if sufficient pump power is available. Although this is true at low doping concentration levels, at high levels important energy dissipation processes can occur [Dig01]. Due to their tendency to cluster at high doping concentrations, Er<sup>3+</sup> ions end up very close to each other, enabling cooperative up-conversion due to a dipole-dipole interaction. During this process, two excited ions in the  $^4I_{13/2}$  energy state interact in such a way that the donor relaxes nonradiatively to the ground state  $^4I_{15/2}$ , while the acceptor is excited to the upper level  $^4I_{9/2}$ . The latter then returns to the state  $^4I_{13/2}$  via a multiphonon emission relaxation process which generates heat in the fiber. This detrimental phenomenon dramatically reduces the efficiency of amplifiers, since it dissipates energy without any emission at 1.5  $\mu\text{m}$ . At high pump power levels at 980 nm, a similar process can drive ions already excited in the  $^4I_{11/2}$  level to the  $^4F_{7/2}$ . Once there, the ions relax via a complex (albeit fast) chain of consecutive processes that generate heat and emission of green light (i.e., between 520 nm and 550 nm). In Fig. 3.4 the most relevant dynamic processes that take place within the energy states of Er<sup>3+</sup>-doped fiber amplifiers at 1.5  $\mu\text{m}$  pumped at 9xx nm are depicted. In the diagram,  $n_i$  is the relative population density in the  $i$ -th energy level,  $W_{ji}$  is the rate of the transition from the level  $j$  to the level  $i$ ,  $\tau_{ji}$  is the lifetime of the level  $j$  and  $C_{\text{up}}$  is the up-conversion coefficient. In this scenario, the corresponding rate

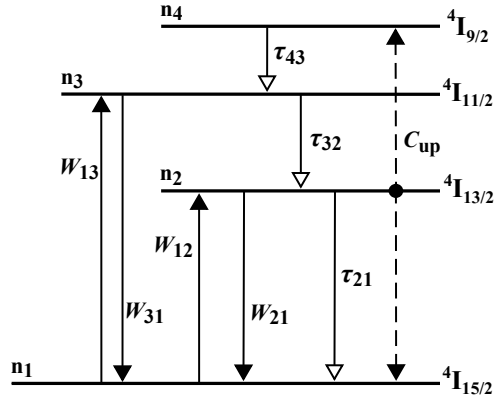


**Figure 3.4:** Illustration of the most relevant transitions involved in the gain process of Er<sup>3+</sup>-doped fiber amplifiers at 1.5  $\mu$ m pumped at 9xx nm.

equations can be written as:

$$\frac{\partial n_1}{\partial t} = -n_1 W_{13} + n_3 W_{31} - n_1 W_{12} + n_2 W_{21} + \frac{n_2}{\tau_{21}} + C_{up} N_{Er} n_2^2 \quad (3.7a)$$

$$\frac{\partial n_2}{\partial t} = n_1 W_{12} - \frac{n_2}{\tau_{21}} - n_2 W_{21} + \frac{n_3}{\tau_{32}} - 2C_{up} N_{Er} n_2^2 \quad (3.7b)$$

$$\frac{\partial n_3}{\partial t} = n_1 W_{13} - n_3 W_{31} - \frac{n_3}{\tau_{32}} + \frac{n_4}{\tau_{43}} \quad (3.7c)$$

$$\frac{\partial n_4}{\partial t} = -\frac{n_4}{\tau_{43}} + C_{up} N_{Er} n_2^2 \quad (3.7d)$$

$$n_1 = 1 - n_2 - n_3 - n_4, \quad (3.7e)$$

where  $N_{Er}$  is the absolute Er<sup>3+</sup> doping concentration.

As represented in Fig. 3.2, Er<sup>3+</sup>-doped fibers can also be pumped in-band at around 1.53  $\mu$ m as well as at around 1.48  $\mu$ m. In these pumping methods the energy level  $4I_{13/2}$  is populated directly, skipping the transition  $4I_{11/2} \rightarrow 4I_{13/2}$ . Therefore, the quantum defect is much lower than if pumped at 980 nm ( $\sim 5\%$  when pumping at 1.48  $\mu$ m versus  $\sim 36\%$  if pumping at 980 nm) which has two advantages. On the one hand higher optical conversion efficiencies are achieved. On the other hand, the heat load is reduced, leading to an easier thermal management of the amplifier. However, pump diodes at 1.48  $\mu$ m and 1.53  $\mu$ m are limited to relatively low power and systems pumped at such wavelength often resort to cascaded Raman fiber lasers as pump sources. This involves an extra degree of complexity and reduces the overall efficiency. Nonetheless, remarkable achievements have been reported with these methods. In [Zha11], an output power of 88 W with an optical efficiency of 69% was demonstrated from an Er<sup>3+</sup>-doped amplifier in-band pumped at 1532 nm. Furthermore, in [Fuj15], up to 11.6 W was obtained with an efficiency of 67.3% in a single-frequency amplifier at 1.54  $\mu$ m pumped by a 1480 nm cascaded Raman fiber laser. In laser configuration, over 100 W has been reported at 1550 nm pumping at 1480 nm with a Raman fiber laser [Sup12].

### 3.3 Er<sup>3+</sup>:Yb<sup>3+</sup>-Codoped Fiber Amplifiers

A major limitation to power scale Er<sup>3+</sup>-doped fiber amplifiers is its relatively low absorption at the wavelengths at which high power pump diodes are available, i.e., at  $\sim 980$  nm. As stated before, increasing the doping concentration eventually leads to loss of efficiency. If larger core fibers are used to increase the number of ions the beam quality can be severely reduced. Furthermore, using longer fibers can trigger deleterious nonlinear effects as will be described later. To overcome such limitations Er<sup>3+</sup>-doped fibers can be codoped with Yb<sup>3+</sup> to form Er<sup>3+</sup>:Yb<sup>3+</sup>-codoped fiber amplifiers. The most interesting property of Yb<sup>3+</sup> in these systems is its absorption cross section, which is approximately a factor of ten higher than in Er<sup>3+</sup>. The typical cross sections of an Yb<sup>3+</sup>-doped fiber are shown in Fig. 3.5. For the sake of comparison, the cross sections of Er<sup>3+</sup> within the same spectral range are included. Yb<sup>3+</sup> is widely used as single active dopant in lasers and amplifiers between

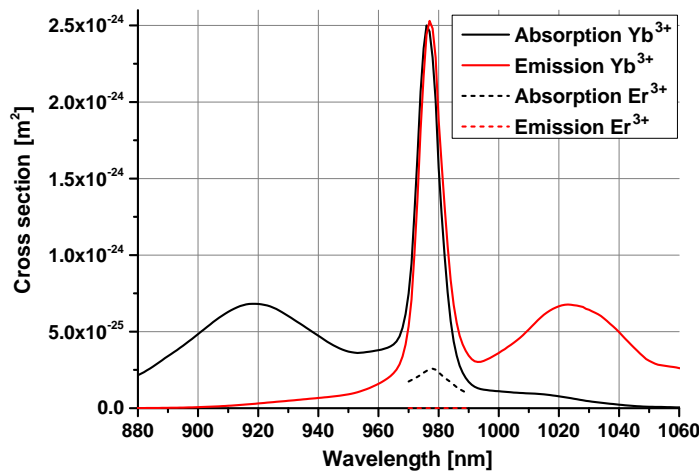


**Figure 3.5:** Typical absorption and emission cross sections of Yb<sup>3+</sup>-doped and Er<sup>3+</sup>-doped fibers.

1  $\mu\text{m}$  and 1.1  $\mu\text{m}$ . When it is used as codopant with Er<sup>3+</sup>, a channel for energy transfer from Yb<sup>3+</sup> to Er<sup>3+</sup> and viceversa is established via dipole-dipole interactions. This allows the excitation of Er<sup>3+</sup> ions by pumping the Yb<sup>3+</sup> ions, and therefore permits to achieve higher absorption. Besides this, Yb<sup>3+</sup> also behaves as a solvent for Er<sup>3+</sup>, which in turn increases up to some extent the feasible Er<sup>3+</sup> doping concentration in the fiber without the detrimental effect of ion clustering [Wag93]. The most relevant energy levels and transitions participating in an Er<sup>3+</sup>:Yb<sup>3+</sup>-codoped fiber amplifier pumped at 9xx nm are depicted in Fig. 3.6. The primary populated levels when the codoped fiber is pumped are the  $^2F_{5/2}$  level in Yb<sup>3+</sup>. The pump light absorbed by Er<sup>3+</sup> ions can be neglected because of two reasons: the absorption of Yb<sup>3+</sup> over Er<sup>3+</sup>, which is about 10 times higher, and the feasible Yb<sup>3+</sup> doping concentration, which is approximately 10 times higher than the Er<sup>3+</sup> doping concentration. In total, the absorption of Yb<sup>3+</sup> is roughly 100 times higher than the absorption of Er<sup>3+</sup>. Then, due to the aforementioned resonant dipole-dipole interaction between Yb<sup>3+</sup> and Er<sup>3+</sup>, the energy is nonradiatively transferred to an Er<sup>3+</sup> ion in its

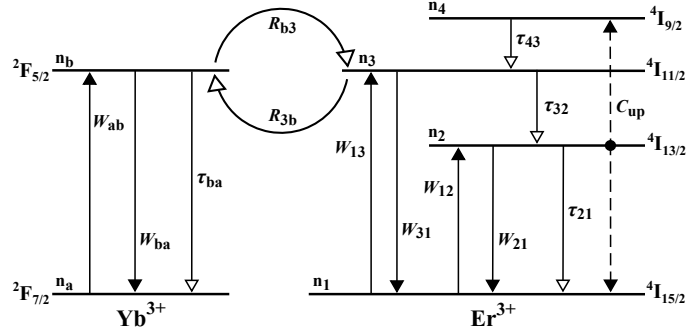


**Figure 3.6:** Illustration of the most relevant transitions involved in the gain process of  $\text{Er}^{3+}:\text{Yb}^{3+}$ -codoped fiber amplifiers at  $1.5\ \mu\text{m}$  pumped at  $980\ \text{nm}$ .

ground state, which will then get excited to the  $4I_{11/2}$  level. From this point,  $\text{Er}^{3+}$  ions behave as described in the subsection 3.2. Similarly to the  $\text{Er}^{3+}$ -doped  $\text{Yb}^{3+}$ -free case, the stored energy is finally spontaneously emitted around  $1.5\ \mu\text{m}$  following the emission cross section spectral distribution (and a significant amount of heat) or, if the system is seeded within this spectral band, the emission will be stimulated at the seeded wavelength. This process can be described by means of the rate equations as [Kar97]

$$\frac{\partial n_1}{\partial t} = -n_1 W_{13} + n_3 W_{31} - n_1 W_{12} + n_2 W_{21} + \frac{n_2}{\tau_{21}} + C_{\text{up}} N_{\text{Er}} n_2^2 - n_b n_1 R_{b3} N_{\text{Yb}} + n_3 n_a R_{3b} N_{\text{Yb}} \quad (3.8a)$$

$$\frac{\partial n_2}{\partial t} = n_1 W_{12} - \frac{n_2}{\tau_{21}} - n_2 W_{21} + \frac{n_3}{\tau_{32}} - 2C_{\text{up}} N_{\text{Er}} n_2^2 \quad (3.8b)$$

$$\frac{\partial n_3}{\partial t} = n_1 W_{13} - n_3 W_{31} - \frac{n_3}{\tau_{32}} + \frac{n_4}{\tau_{43}} + n_b n_1 R_{b3} N_{\text{Yb}} - n_3 n_a R_{3b} N_{\text{Yb}} \quad (3.8c)$$

$$\frac{\partial n_4}{\partial t} = -\frac{n_4}{\tau_{43}} + C_{\text{up}} N_{\text{Er}} n_2^2 \quad (3.8d)$$

$$n_1 = 1 - n_2 - n_3 - n_4 \quad (3.8e)$$

$$\frac{\partial n_a}{\partial t} = -n_a W_{ab} + n_b W_{ba} + \frac{n_b}{\tau_{ba}} + n_b n_1 R_{b3} N_{\text{Er}} - n_3 n_a R_{3b} N_{\text{Er}} \quad (3.8f)$$

$$\frac{\partial n_b}{\partial t} = n_a W_{ab} - n_b W_{ba} - \frac{n_b}{\tau_{ba}} - n_b n_1 R_{b3} N_{\text{Er}} + n_3 n_a R_{3b} N_{\text{Er}} \quad (3.8g)$$

$$n_a = 1 - n_b, \quad (3.8h)$$

where  $n_i$  is the population density of the  $i$ -th energy level,  $\tau_{ij}$  is the lifetime of the  $i$ -th energy level with respect to the transition to the  $j$ -th level.  $W_{ij}$  is the stimulated transfer rate of the transition from the energy level  $i$  to the energy level  $j$ ,  $N_{\text{Yb}}$  is the  $\text{Yb}^{3+}$  ion concentration and  $R_{ij}$  represents the energy transfer rate between  $\text{Yb}^{3+}$  and  $\text{Er}^{3+}$ . The  $R$ -parameters depend on the integral overlap between the donor  $\text{Yb}^{3+}$  and acceptor

$\text{Er}^{3+}$  absorption cross sections as:

$$R_{b3} \propto \int \sigma_{\text{Yb}}^{\text{em}}(\lambda) \sigma_{\text{Er}}^{\text{abs}}(\lambda) d\lambda \quad (3.9a)$$

$$R_{3b} \propto \int \sigma_{\text{Er}}^{\text{em}}(\lambda) \sigma_{\text{Yb}}^{\text{abs}}(\lambda) d\lambda. \quad (3.9b)$$

These parameters are of enormous importance because of their impact on the overall performance of  $\text{Er}^{3+}:\text{Yb}^{3+}$  fiber lasers and amplifiers, especially at high pump power levels [Hwa00; Lar06; Sef04].

### 3.4 Limitations in Single-Frequency Fiber Amplifiers

The fact that GWDs require laser beams with high fundamental mode content and single-frequency operation introduces an extra level of difficulty to the power scaling of such laser systems. A clear example of this condition is observed in fiber amplifiers at  $1 \mu\text{m}$ , whose state-of-the-art is much more mature than at  $1.5 \mu\text{m}$ . Nowadays, power levels of  $400 \text{ W}$  have been demonstrated around  $1 \mu\text{m}$  in all-fiber and near diffraction-limited systems with linewidths of few tens of kHz [Hua17], while amplifiers where such narrow linewidth is not required reach the multi-kW scale [Fan14]. Focusing back to  $1.5 \mu\text{m}$ , the limitations due to the  $\text{Er}^{3+}$  low absorption are overcome by codoping with  $\text{Yb}^{3+}$  as described in Section 3.3. Nonetheless, a new restrictive phenomenon arises, as it is the  $\text{Yb}^{3+}$ -band amplified spontaneous emission (ASE). In addition, the stimulated Brillouin scattering (SBS) is also a process limiting the power scaling of single-frequency fiber amplifiers.

#### 3.4.1 $\text{Yb}^{3+}$ -band Amplified Spontaneous Emission

When  $\text{Er}^{3+}:\text{Yb}^{3+}$ -codoped fibers are pumped at high power levels, the  $\text{Yb}^{3+}$ -to- $\text{Er}^{3+}$  energy transfer saturates as the  $\text{Er}^{3+}$  ground energy level gets depleted. The lifetime of the excited  $\text{Yb}^{3+}$  energy level  ${}^2\text{F}_{5/2}$  is approximately  $1 \text{ ms}$ . Thus, if an excited  $\text{Yb}^{3+}$  ion does not transfer the energy to an  $\text{Er}^{3+}$  ion within this time it will, very likely, spontaneously relax to the  ${}^2\text{F}_{7/2}$  state, releasing the stored energy as a photon with wavelength depending on the  $\text{Yb}^{3+}$  emission cross section, i.e., in the  $1 \mu\text{m}$  band. Such event can, in turn, trigger a stimulated process, which leads to the generation of parasitic lasing or pulsing. This is represented in Fig. 3.6 as  $\tau_{\text{ba}}$  (spontaneous relaxation) and  $W_{\text{ba}}$  (stimulated process), and contemplated in the rate equations at Eq. 3.8g. This behavior can be interpreted as a bottlenecking effect of the energy transfer from  $\text{Yb}^{3+}$  to  $\text{Er}^{3+}$ . There are two main causes that trigger  $\text{Yb}^{3+}$ -band ASE in  $\text{Er}^{3+}:\text{Yb}^{3+}$ -doped fiber amplifiers. The first is the shortage of  $\text{Er}^{3+}$  ions in the  ${}^4\text{I}_{15/2}$  state that can happen either because the amplifier is pumped with too high power or because the fiber has a low concentration of  $\text{Er}^{3+}$  ions compared to  $\text{Yb}^{3+}$  ions. The second possible cause of excess  $\text{Yb}^{3+}$ -band ASE is a too low seed power. In this case the  ${}^4\text{I}_{13/2} \rightarrow {}^4\text{I}_{15/2}$  transition in  $\text{Er}^{3+}$  is poorly stimulated, resulting in a low availability of  $\text{Er}^{3+}$  ions in the ground state, which has a negative impact on the  $\text{Yb}^{3+}$ -to- $\text{Er}^{3+}$  energy transfer. As  $\text{Yb}^{3+}$ -band ASE increases, the risk of parasitic lasing increases. Such parasitic lasing is quite often very unstable and can eventually damage the system.

It is possible to take control of the stimulated process at 1  $\mu\text{m}$  by intentionally coseeding the amplifier with a signal at a wavelength within the ASE spectral range [Ste14a]. By coseeding, the excess energy is removed from the  $\text{Yb}^{3+}$  ions, resulting in a controlled auxiliary signal. In-band pumping of  $\text{Er}^{3+}$  in  $\text{Er}^{3+}:\text{Yb}^{3+}$  fibers has also demonstrated better results than similar methods based on  $\text{Er}^{3+}$ -doped  $\text{Yb}^{3+}$ -free fibers due to the higher concentration of  $\text{Er}^{3+}$  ions in codoped fibers compared to single dopant fibers [Sup12] and is not affected by  $\text{Yb}^{3+}$ -band ASE. The so-called *off-peak* pumping technique (i.e., pumping the  $\text{Yb}^{3+}$  with a wavelength different to its maximum absorption one) has also been reported to be effective to increase the threshold of  $\text{Yb}^{3+}$ -band ASE, reaching up to 200 W of output power at 1560 nm in a single-frequency amplifier [Cre16]. This method takes advantage of the fact that the pump power is absorbed more homogeneously along the fiber, allowing more  $\text{Er}^{3+}$  ions to get excited before the onset of bottlenecking effects [Cre16; Var18b].

### 3.4.2 Stimulated Brillouin Scattering

Spontaneous Brillouin scattering is a linear phenomenon that occurs when an incident photon interacts inelastically with a phonon, i.e., vibrations of the material molecules. The resulting scattered photons propagate in both directions with downshifted frequency as a consequence of the energy and momentum conservation. The backscattered Stokes wave interferes with the input light and generates an acoustic wave through electrostriction (i.e., the change of the medium density when exposed to an intense light). The result is a density grating that scatters the photons in the backward direction [Kob10]. If the intensity of the input light increases, the amplitude of the acoustic wave increases as well and the process becomes stimulated. The process is illustrated in Fig. 3.7, where  $\omega_p$  is the frequency of the incident light,  $\Omega_B$  is the frequency of the acoustic wave, and  $\omega_s = \omega_p - \Omega_B$  is the frequency of the resulting Stokes wave. It can be demonstrated that the frequency

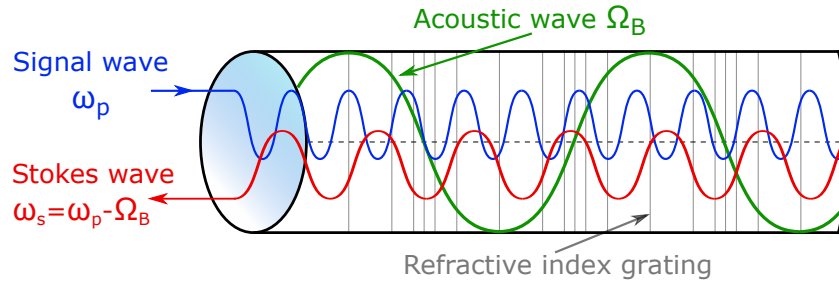


**Figure 3.7:** Illustration of spontaneous Brillouin scattering in optical fibers. The incident photons with frequency  $\omega_p$  interact with the thermally induced acoustic waves of frequency  $\Omega_B$ . The resulting Stokes wave frequency is then  $\omega_s = \omega_p - \Omega_B$ .

shift of the Brillouin scattering in optical fibers with respect to the incident optical signal is given by [Agr07]

$$\nu_B = \frac{2n_p\nu_A}{\lambda_p}, \quad (3.10)$$

where  $n_p$  is the refractive index,  $\nu_A$  is the acoustic velocity and  $\lambda_p$  is the wavelength of the propagating light that originates the process. In standard fused silica fibers the Brillouin shift is  $\approx 11.1$  GHz at  $1.55 \mu\text{m}$ .

When the spontaneous effect becomes stimulated, the phenomenon turns nonlinear [Dam03]. The intensity (or power) value at which this happens is denominated the stimulated Brillouin scattering (SBS) threshold, and is usually defined as the power that makes 50 % of the light backscatter. For passive fibers, such power threshold can be calculated as [Agr07]

$$P_{\text{th}} = \frac{21A_{\text{eff}}}{g_{\text{B}}(\Omega_{\text{B}})L_{\text{eff}}}, \quad (3.11)$$

where  $A_{\text{eff}}$  is the effective mode area and  $L_{\text{eff}}$  is the effective interaction length

$$L_{\text{eff}} = \frac{1}{\alpha(1 - \exp(-\alpha L))}, \quad (3.12)$$

where  $\alpha$  is the loss in the fiber and  $L$  the actual fiber length. In Eq. 3.11, the parameter  $g_{\text{B}}(\Omega_{\text{B}})$  is the peak value of the Brillouin gain spectrum. This value depends on the material properties as

$$g_{\text{B}}(\Omega_{\text{B}}) = \frac{8\pi^2\gamma_e^2}{n_p\lambda_p^2\rho_0c\nu_A\Gamma_{\text{B}}}, \quad (3.13)$$

where  $\gamma_e$  is the electrostrictive constant,  $\rho_0$  is the material density,  $c$  is the speed of light in vacuum and  $\Gamma_{\text{B}}$  is the phonon lifetime.

In fiber amplifiers the SBS threshold can be significantly different than in passive fibers. The reason is that the SBS peak spectrum falls within the emission cross section of the fiber and thus, the amplifier's gain influences the SBS gain spectrum along the fiber in a rather complex way. Although analytical studies and approximated expressions have been reported [Kov05], a conclusive close solution is not available. In these cases the SBS threshold can be experimentally estimated by observing the power of the back propagating signal versus the forward propagating signal. The SBS process is triggered at the power at which this curve losses the linearity. This is illustrated in Fig. 3.8. The lost of linearity in the monitored power levels occurs significantly before the 50 % of the power is backscattered, making this threshold definition much more restrictive than the defined in Eq. 3.11.

There are several ways how SBS affects negatively in a single-frequency fiber amplifier. The Brillouin scattered signal is not only pumped by the signal that triggers the process, but also experiences the amplifier's gain. Under such circumstances the backward propagating SBS signal contributes to the depopulation of the excited energy levels as it builds up and leads to a reduction of efficiency and loss of linearity of the desired output signal. Besides this, the SBS imprints a broadband excess noise on the output signal [Hor97]. The potential effects of the backward propagating signal, which can produce serious damage to the optical components, can also become an important issue. Therefore, the suppression of SBS is a key factor in single-frequency amplifiers to enable further power scaling and many

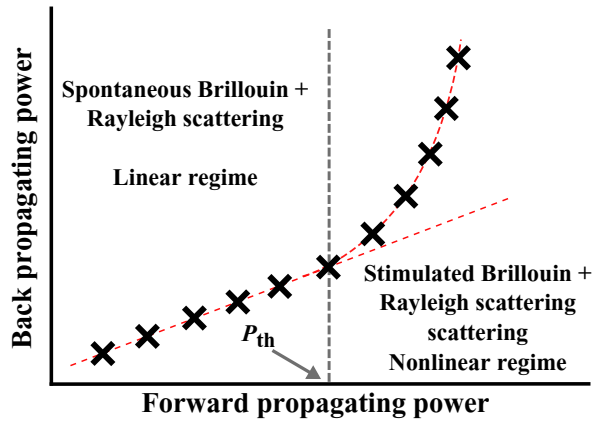


**Figure 3.8:** Typical backward propagating signal below the SBS threshold (linear regime) and above the SBS threshold (nonlinear regime).  $P_{th}$  indicates the SBS threshold.

methods have demonstrated to be effective in this regard. Since the SBS gain depends on the material properties as seen in Eq. 3.13, the fiber design can be tuned to disfavor it. However, the fiber properties are usually constricted to obtain the desired NA, MFD, etc. The increase in size of the core to reduce the light intensity is a commonly used method to push the threshold of SBS and other nonlinearities. Nevertheless, as it was described in Section 3.1, the core size is restricted when single mode output is desired. A more convenient method is to expose the fiber to different temperatures [Han01], which has been successfully demonstrated in high power fiber amplifiers at  $1\ \mu\text{m}$  [The12a]. Another studied technique consists on applying strain forces along the fiber [Yos93]. These methods are essentially based on changing the acoustic velocity in the fiber, which impacts the SBS frequency shift as seen in Eq. 3.10.



# CHAPTER 4

---

## Gain Dynamics of Er<sup>3+</sup>-Doped Fiber Amplifiers

---

The knowledge of the temporal dynamics of laser systems can be a supporting tool to design, optimize, and tune stabilization systems (e.g., power stabilization) and setting actuating strategies (e.g., in coherent beam combination (CBC) systems). More specifically, there are two important concepts with potential applicability in fiber-based lasers for GWDs for which the study of the pump-to-output-signal frequency response is interesting. First, modelling the transfer function permits to forecast how the intensity noise from the pump diodes will couple to the output signal. In principle this could enable tailored strategies to optimize a hypothetical stabilization system. Thus, the response of the amplifier to a power stabilization strategy acting on the pump power can be known in advance for a fiber with a given set of parameters. This can be applied to optimize a local power stabilization in, for example, a preamplifier stage without free-space components. Secondly, predicting the influence of the pump power on the phase noise of the output signal can be exploited in all-fiber CBC systems using fiber amplifiers as phase actuators [Fot09; Tün12a; Tün11].

The dynamics of Er<sup>3+</sup>:Yb<sup>3+</sup>-doped fiber amplifiers have been extensively investigated [Ste15]. However, the case of Er<sup>3+</sup>-doped Yb<sup>3+</sup>-free fiber amplifiers had not been studied so far. In this chapter, an analytical model of the pump-to-output-signal transfer function is developed in Section 4.1. Next, in Section 4.2 the model is validated experimentally, for which the pump-to-output-power and pump-to-phase-shift transfer functions were measured in two different experiments. Combining the experimental data and the analytical model, the spontaneous lifetime of the Er<sup>3+</sup> energy levels <sup>4</sup>I<sub>11/2</sub> and <sup>4</sup>I<sub>13/2</sub> were estimated to be 7.9 μs and 8.7 ms, showing a fairly good agreement with the values available in the literature. In Section 4.3, the frequency response beyond the possibilities of the experimental setup is studied using the model.

The results presented in this Chapter have partially been published [Var16].

### 4.1 Analytical Model

The relevant energy levels and transitions shown in Fig. 3.4 of Chapter 3 can be simplified to a 3-level system if up-conversion is neglected. This is a good approximation in most cases given that the manufacturers design their fibers to reduce Er<sup>3+</sup> clustering as much as possible. In any case, the transition <sup>4</sup>I<sub>9/2</sub>→<sup>4</sup>I<sub>11/2</sub>, subjected to the occurrence of up-conversion, would not produce noticeable effects on the temporal dynamics in the frequency range under study in this chapter and only a small impact on the population of the energy levels <sup>4</sup>I<sub>11/2</sub> and <sup>4</sup>I<sub>15/2</sub> would be relevant at high pump power levels. Thus, neglecting

up-conversion, the set of Eqs. (3.7) can be reduced to

$$\frac{\partial n_2}{\partial t} = n_1 W_{12} - \frac{n_2}{\tau_{21}} - n_2 W_{21} + \frac{n_3}{\tau_{32}} \quad (4.1a)$$

$$\frac{\partial n_3}{\partial t} = n_1 W_{13} - n_3 W_{31} - \frac{n_3}{\tau_{32}} \quad (4.1b)$$

$$0 = p - n_1 - n_2 - n_3. \quad (4.1c)$$

Here,  $n_i$  represents the absolute population density of the energy levels (in ions per m<sup>3</sup>) and  $p$  is the ion concentration of the fiber ( $p = n_1 + n_2 + n_3$ ). Eq. (3.7a) has been omitted since it provides redundant information. The transition rates  $W_{ij}$  can be expressed as

$$W_{13} = \frac{\Gamma_p \sigma_p^{\text{abs}} P_p(z,t)}{A_c} \quad (4.2a) \quad W_{12} = \frac{\Gamma_s \sigma_s^{\text{abs}} P_s(z,t)}{A_c} \quad (4.2c)$$

$$W_{31} = \frac{\Gamma_p \sigma_p^{\text{em}} P_p(z,t)}{A_c} \quad (4.2b) \quad W_{21} = \frac{\Gamma_s \sigma_s^{\text{em}} P_s(z,t)}{A_c}, \quad (4.2d)$$

where the cross sections  $\sigma$  are labeled with the superscripts *abs* and *em* to denote absorption and emission at both, seed and pump wavelengths.  $P_p(z,t)$  and  $P_s(z,t)$  are the pump and seed power levels in photons per second,  $A_c$  is the core area and the parameters  $\Gamma_p$  and  $\Gamma_s$  are the overlap factors of the pump and seed fields with the core area expressed as

$$\Gamma_{p,s} = 1 - \exp\left(\frac{-2r_c^2}{\omega_{p,s}^2}\right), \quad (4.3)$$

where  $r_c$  is the core radius and  $\omega_{p,s}$  the mode radius at the pump and seed wavelengths

$$\omega_{p,s} \simeq r_c \left(0.65 + \frac{1.619}{V_{p,s}^{1.5}} + \frac{2.879}{V_{p,s}^6}\right). \quad (4.4)$$

The evolution of the seed and pump power along the fiber at a given time is

$$\frac{\partial P_s}{\partial z} = \Gamma_s \left(n_2 \sigma_s^{\text{em}} - n_1 \sigma_s^{\text{abs}}\right) P_s = A_c (W_{21} n_2 - W_{12} n_1) \quad (4.5a)$$

$$\frac{\partial P_p}{\partial z} = \Gamma_p \left(n_3 \sigma_p^{\text{em}} - n_1 \sigma_p^{\text{abs}}\right) P_p = A_c (W_{31} n_3 - W_{13} n_1). \quad (4.5b)$$

If we now substitute Eqs. (4.5a) and (4.5b) in Eqs. (4.1a) and (4.1b), and perform the integration along the fiber

$$\int_0^L \frac{\partial n_2}{\partial t} dz = -\frac{1}{A_c} \int_0^L \frac{\partial P_s}{\partial z} dz - \int_0^L \frac{n_2}{\tau_{21}} dz + \int_0^L \frac{n_3}{\tau_{32}} dz \quad (4.6a)$$

$$\int_0^L \frac{\partial n_3}{\partial t} dz = -\frac{1}{A_c} \int_0^L \frac{\partial P_p}{\partial z} dz - \int_0^L \frac{n_3}{\tau_{32}} dz, \quad (4.6b)$$

then yields

$$\frac{\partial N_2}{\partial t} = P_s(z=0) - P_s(z=L) - \frac{N_2}{\tau_{21}} + \frac{N_3}{\tau_{32}} \quad (4.7a)$$

$$\frac{\partial N_3}{\partial t} = P_p(z=0) - P_p(z=L) - \frac{N_3}{\tau_{32}}. \quad (4.7b)$$

Here,  $N_i = A_c \int_0^L n_i dz$  is the absolute number of ions in the  $i$ -th energy level within the whole fiber length. The pump and seed power levels at the output of the fiber can be written as functions of the levels at the input as

$$P_s(z=L) = P_s(z=0) e^{B_s N_2 - C_s + \frac{\Gamma_s \sigma_s^{\text{abs}}}{A_c} N_3} \quad (4.8a)$$

$$P_p(z=L) = P_p(z=0) e^{B_p N_3 - C_p + \frac{\Gamma_p \sigma_p^{\text{abs}}}{A_c} N_2}, \quad (4.8b)$$

with  $B_{p,s}$  and  $C_{p,s}$  coefficients

$$B_p = \frac{\Gamma_p}{A_c} (\sigma_p^{\text{abs}} + \sigma_p^{\text{em}}) \quad (4.10a) \quad C_p = \Gamma \sigma_p^{\text{abs}} p \quad (4.10c)$$

$$B_s = \frac{\Gamma_p}{A_c} (\sigma_s^{\text{abs}} + \sigma_s^{\text{em}}) \quad (4.10b) \quad C_s = \Gamma \sigma_s^{\text{abs}} p. \quad (4.10d)$$

Using the Eqs. (4.8a) and (4.8b) to remove the dependency on the output power of Eqs. (4.7a) and (4.7b) gives

$$\frac{\partial N_2}{\partial t} = P_s(z=0) - \left( 1 - \exp \left( B_s N_2 - C_s + \frac{\Gamma_s \sigma_s^{\text{abs}}}{A_c} N_3 \right) \right) - \frac{N_2}{\tau_{21}} + \frac{N_3}{\tau_{32}} \quad (4.11a)$$

$$\frac{\partial N_3}{\partial t} = P_p(z=0) - \left( 1 - \exp \left( B_p N_3 - C_p + \frac{\Gamma_p \sigma_p^{\text{abs}}}{A_c} N_2 \right) \right) - \frac{N_3}{\tau_{32}}. \quad (4.11b)$$

Eqs. (4.11a) and (4.11b) express the temporal evolution of the total ion population densities in the energy levels  ${}^4I_{13/2}$  and  ${}^4I_{11/2}$ . To deduct the corresponding transfer functions, let the input pump power be

$$P_p(z=0, t) = P_{p, \text{in}} (1 + m_p e^{i\omega t}), \quad (4.12)$$

where  $m_p \ll 1$  is the (small) modulation depth. Thus, the small ( $\delta_2, \delta_3 \ll 1$ ) modulations of the population densities around their steady state solutions  $N_2^0$  and  $N_3^0$  can be written as

$$N_2(t) = N_2^0 \left( 1 + \delta_2 e^{i(\omega t + \phi_2)} \right) \quad (4.13a)$$

$$N_3(t) = N_3^0 \left( 1 + \delta_3 e^{i(\omega t + \phi_3)} \right). \quad (4.13b)$$

Substituting Eqs. (4.12)-(4.13b) in (4.11b) yields

$$\begin{aligned} \frac{\partial N_3}{\partial t} = & P_{p,\text{in}} (1 + m_p e^{i\omega t}) \\ & \cdot \left( 1 - e^{B_p N_3^0 - C_p + \frac{\Gamma_p \sigma_p^{\text{abs}}}{A_c} N_2^0} e^{B_p N_3^0 \delta_3 \exp(i(\omega t + \phi_3))} e^{\frac{\Gamma_p \sigma_p^{\text{abs}}}{A_c} N_2^0 \delta_2 \exp(i(\omega t + \phi_2))} \right) \\ & - \frac{N_3^0}{\tau_{32}} - \frac{N_3^0}{\tau_{32}} \delta_3 e^{i(\omega t + \phi_3)}. \end{aligned} \quad (4.14)$$

Since  $\delta_2$  and  $\delta_3$  are small, we can apply the approximation  $e^{\delta_k \dots} \approx 1 + \delta_k \dots$  and neglect the higher order terms  $\delta_2^2$  and  $\delta_2 \delta_3$ . Using Eq. (4.8b) it follows

$$\begin{aligned} \frac{\partial N_3}{\partial t} \approx & \underbrace{P_p^0(z=0) - P_p^0(z=L) - \frac{N_3^0}{\tau_{32}}}_{=0 \text{ since it is steady state}} + (P_p^0(z=0) - P_p^0(z=L)) m_p e^{i\omega t} \\ & - P_p^0(z=L) B_p N_3^0 \delta_3 e^{i(\omega t + \phi_3)} + P_p^0(z=L) \frac{\Gamma_p \sigma_p^{\text{abs}}}{A_c} N_2^0 \delta_2 e^{i(\omega t + \phi_2)} \\ & - \frac{N_3^0}{\tau_{32}} \delta_3 e^{i(\omega t + \phi_3)}. \end{aligned} \quad (4.15)$$

If we now introduce Eq. (4.13b) and multiply by  $\frac{e^{-i\omega t}}{m_p}$ , then Eq. (4.15) becomes

$$\frac{N_3^0 \delta_3}{m_p} e^{i\phi_3} = \frac{P_p^0(z=0) - P_p^0(z=L) \left( 1 - \frac{\Gamma_p \sigma_p^{\text{abs}}}{A_c} \frac{N_2^0 \delta_2}{m_p} e^{i\phi_2} \right)}{i\omega + B_p P_p^0(z=L) + \frac{1}{\tau_{32}}}. \quad (4.16)$$

Eq. (4.16) represents the transfer function of the population density of the upper energy level  ${}^4\text{I}_{11/2}$ , where  $N_3^0 \delta_3$  is the magnitude around its steady state,  $m_p$  is the modulation depth of the input signal and  $e^{i\phi_3}$  is a phase term. A simplification of Eq. (4.16) is possible if we assume full pump power absorption, which is a reasonable approximation in practical amplifiers. Hence, if  $P_p^0(z=L) \approx 0$ , Eq. (4.16) is reduced to

$$\frac{N_3^0 \delta_3}{m_p} e^{i\phi_3} = \frac{P_p^0(z=0)}{i\omega + \frac{1}{\tau_{32}}}. \quad (4.17)$$

Therefore, the transfer function of the population density of the upper energy level is a single low-pass with cutoff frequency at  $\frac{1}{\tau_{32}}$ . Similarly, using Eq. (4.11a), it can be shown that the transfer function of the meta-stable level  ${}^4\text{I}_{13/2}$  is

$$\frac{N_2^0 \delta_2}{m_p} e^{i\phi_2} = \frac{\frac{1}{\tau_{32}} - P_s^0(z=L) \frac{\Gamma_s \sigma_s^{\text{abs}}}{A_c}}{i\omega + B_s P_s^0(z=L) + \frac{1}{\tau_{21}}} \frac{N_3^0 \delta_3}{m_p} e^{i\phi_3}. \quad (4.18)$$

It can be seen that  $\frac{N_2^0 \delta_2}{m_p} e^{i\phi_2}$  contains  $\frac{N_3^0 \delta_3}{m_p} e^{i\phi_3}$ . Thus, the transfer function of the energy level  ${}^4I_{13/2}$  is a double low-pass with two different cutoff frequencies; one at  $\frac{1}{\tau_{32}}$  that depends on the lifetime of the energy level  ${}^4I_{11/2}$ , and another at  $B_s P_s^0(z=L) + \frac{1}{\tau_{21}}$  that depends on the cross sections at the seed wavelength, the fiber geometry and the output power. To obtain the transfer function of the output signal we proceed in a similar way using Eq. (4.8a). Again, we assume the population densities  $N_2(t)$  and  $N_3(t)$  and the seed power  $P_s(z=L)$  are modulated around their steady state solutions as

$$N_2(t) = N_2^0 \left( 1 + \delta_2 e^{i(\omega t + \phi_2)} \right) \quad (4.19a)$$

$$N_3(t) = N_3^0 \left( 1 + \delta_3 e^{i(\omega t + \phi_3)} \right) \quad (4.19b)$$

$$P_s(z=L) = P_s^0(z=L) \left( 1 + m_s e^{i(\omega t + \phi_s)} \right) \quad (4.19c)$$

Then, substituting Eqs. (4.19) in Eq. (4.8a), applying again the approximation  $e^{\delta_k \dots} \approx 1 + \delta_k \dots$  and neglecting the terms  $\delta_2^2$  and  $\delta_2 \delta_3$ , yields

$$P_s^0(z=L) \left( 1 + m_s e^{i(\omega t + \phi_s)} \right) = P_s^0(z=L) \left( 1 + B_s N_2^0 \delta_2 e^{i(\omega t + \phi_2)} + \frac{\Gamma_s \sigma_s^{\text{abs}}}{A_c} N_3^0 \delta_3 e^{i(\omega t + \phi_3)} \right). \quad (4.20)$$

Canceling the terms  $P_s^0(z=L)$  and multiplying by  $\frac{e^{-i\omega t}}{m_p}$  yields

$$\frac{m_s}{m_p} e^{i\phi_s} = B_s \frac{N_2^0 \delta_2}{m_p} e^{i\phi_2} + \frac{\Gamma_s \sigma_s^{\text{abs}}}{A_c} \frac{N_3^0 \delta_3}{m_p} e^{i\phi_3}. \quad (4.21)$$

Eq. (4.21) is the transfer function of the amplified signal. It is expressed as function of the previously calculated transfer functions  $\frac{N_2^0 \delta_2}{m_p} e^{i\phi_2}$  and  $\frac{N_3^0 \delta_3}{m_p} e^{i\phi_3}$ . If we substitute them in Eq. (4.21), it becomes

$$\frac{m_s}{m_p} e^{i\phi_s} = \frac{P_P^0(z=0) \frac{\Gamma_s \sigma_s^{\text{abs}}}{A_c}}{\underbrace{\frac{1}{\tau_{32}} + i\omega}_{\omega_2}} \left( \frac{\overbrace{\frac{B_s A_c}{\Gamma_s \sigma_s^{\text{abs}}} \frac{1}{\tau_{32}} + \frac{1}{\tau_{21}} + i\omega}_{\omega_3}}{\underbrace{B_s P_s^0(z=L) + \frac{1}{\tau_{21}}}_{\omega_1} + i\omega} \right) \quad (4.22)$$

which can be written more compactly as

$$\frac{m_s}{m_p} e^{i\phi_s} = \frac{K}{\omega_2 + i\omega} \left( \frac{\omega_3 + i\omega}{\omega_1 + i\omega} \right) \quad (4.23)$$

where  $K$ ,  $\omega_1$ ,  $\omega_2$  and  $\omega_3$  are given by

$$K = P_p^0(z=0) \frac{\Gamma_s \sigma_s^{\text{abs}}}{A_c} \quad (4.24a)$$

$$\omega_1 = B_s P_s^0(z=L) + \frac{1}{\tau_{21}} \quad (4.24b)$$

$$\omega_2 = \frac{1}{\tau_{32}} \quad (4.24c)$$

$$\omega_3 = \frac{B_s A_c}{\Gamma_s \sigma_s^{\text{abs}}} \frac{1}{\tau_{32}} + \frac{1}{\tau_{21}}. \quad (4.24d)$$

Therefore, the pump-to-output-signal transfer function is a single low-pass  $\frac{1}{\omega_2 + i\omega}$  multiplied by the term  $\frac{\omega_3 + i\omega}{\omega_1 + i\omega}$ , which is a damped low-pass if  $\omega_3 > \omega_1$  or a damped high-pass if  $\omega_1 > \omega_3$ . For a given fiber, this condition depends exclusively on the power of the output signal. The power threshold which changes the condition can be calculated by comparing Eqs. (4.24b) and (4.24d), and its value, in watts, is

$$P_s^0(z=L) \begin{cases} \text{if } \omega_3 > \omega_1 \\ \lesseqgtr \\ \text{if } \omega_1 > \omega_3 \end{cases} \frac{A_c}{\tau_{\text{mp}} \Gamma_s \sigma_s^{\text{abs}}} \frac{h c}{\lambda_s}, \quad (4.25)$$

where  $h$  is the Planck constant,  $c$  is the speed of light in vacuum and  $\lambda_s$  is the wavelength of the seed signal.

## 4.2 Experiments

This section is dedicated to the experimental validation of the analytical model developed in Section 4.1 by means of the pump-to-signal and pump-to-phase-shift frequency responses. The transfer functions of an Er<sup>3+</sup>-doped fiber amplifier are measured and analyzed using the model to estimate the values of  $\tau_{32}$  and  $\tau_{21}$ , which correspond to the spontaneous lifetimes of the energy levels  $^4I_{11/2}$  and  $^4I_{13/2}$ .

### 4.2.1 Pump-to-Signal Transfer Function

The experimental arrangement to measure the pump-to-signal transfer function is shown in Fig. 4.1. An Er<sup>3+</sup>-doped fiber amplifier was set-up with 14 m of a commercial single-mode silica fiber with core and cladding diameters of 8.5  $\mu\text{m}$  and 125  $\mu\text{m}$ . The amplifier was seeded at 1572 nm by a distributed feedback (DFB) diode with MHz-scale linewidth and core-pumped at 976 nm by a single-mode pump diode. The pump and seed light were coupled into the core of the active fiber through a 976/1572 nm wavelength division multiplexer (WDM). The available power at the beginning of the fiber was 65 mW at 1572 nm and 530 mW at 976 nm. Another 976/1572 nm WDM was attached to the output in order to filter out any potential residual pump light. Additionally, a bandpass filter centered at 1570 nm with a bandwidth of 12 nm was used to remove any ASE. The output signal was detected using an InGaAs photodetector (DET01CFC, *Thorlabs*) with 1.2 GHz bandwidth and measured by a network analyzer. The sweep signal from the network analyzer was used to modulate the current driven to the pump diode with a modulation depth of  $m_p = 10\%$  (peak to peak). The small amount of pump light in the secondary

port of the input WDM, also measured with a DET01CFC photodetector, was fed to the network analyzer as reference signal. The use of this reference ensures that the transfer functions of the current driver and pump diode do not influence the measurements. The

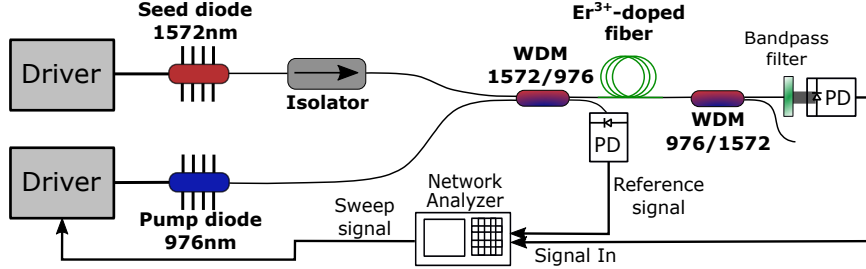


**Figure 4.1:** Experimental setup to measure the pump-to-output-signal transfer function of an  $\text{Er}^{3+}$ -doped fiber amplifier. WDM: wavelength division multiplexer, PD: photodiode.

network analyzer calculated the magnitude of the transfer function as  $20 \log_{10} (V_{\text{in}}/V_{\text{ref}})$ . The maximum output power at the seed wavelength was 250 mW.

In Fig. 4.2 the transfer functions measured at different output power levels are presented. In agreement with Eq. (4.24b), the cutoff frequency shifts with the output power. Besides this, the curves reach a slope of -40 dB/dec, which is compatible with a double low-pass function. The phase plot shows a maximum phase shift of approximately  $150^\circ$ . In principle, one could expect a phase shift of  $180^\circ$  given the double low-pass of the magnitude. However, as demonstrated in Section (4.1) (see Eq. (4.22)), the transfer function is a single low-pass multiplied by a term that can either be a damped high-pass or a damped low-pass, depending on the output power. This, in conjunction with the fact that the poles of the transfer function manifest in the phase about one decade before than in the magnitude, suggests that the actual term multiplying the low-pass might be a damped low-pass. In such case this would also indicate that the output power levels are below the threshold established in Eq. (4.25), and therefore the amplifier would be in the regime where  $\omega_3 > \omega_1$ . Unfortunately, the sensitivity of the network analyzer limited the measurement to approximately 150 kHz and consequently the impact of  $\omega_3$  is not clearly resolved. The fit of the model in Eq. (4.22) to the transfer function at the output power of 250 mW is shown in Fig. 4.3. The frequency axis has been extended to show the fit function up to 1 MHz. At around 400 kHz the slope of the magnitude becomes less steep and the phase shift is reduced by approximately  $40^\circ$  within 1 decade between 100 kHz and 1 MHz. This damped low-pass behavior might have beneficial consequences when designing stabilization systems. For example, a hypothetical feedback loop to the current of the pump diodes would be possible without the need to design electronics to compensate phase shifts  $\gtrsim 180^\circ$ . Additionally, the capability to change the damped low-pass term to a damped high-pass by acting on the output power could potentially be exploited in the design of control systems. The spontaneous lifetime of the energy levels  ${}^4\text{I}_{11/2}$  and  ${}^4\text{I}_{13/2}$  can be estimated using the expressions of the inverse

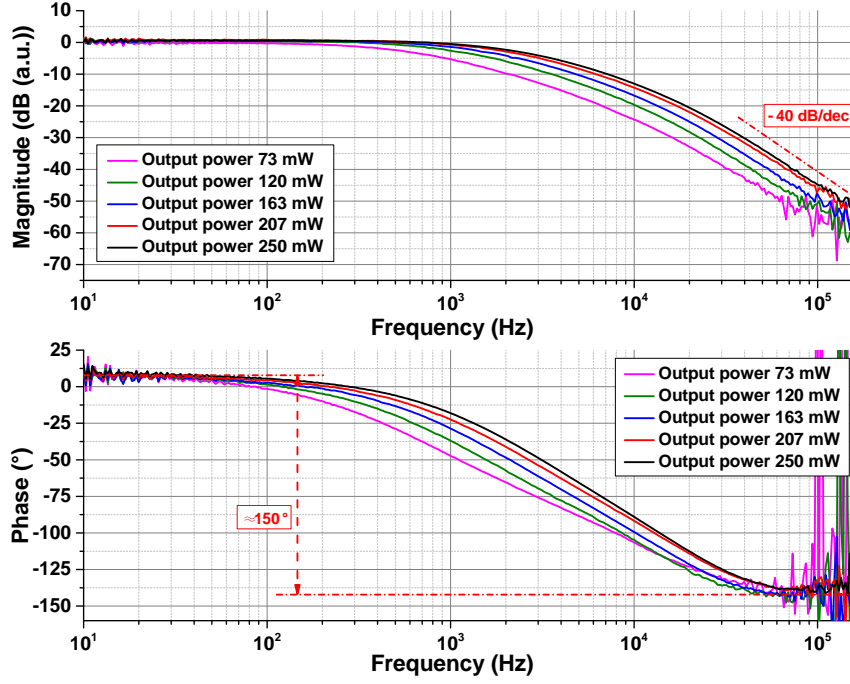


**Figure 4.2:** Measured pump-to-output-signal transfer functions for different output power levels. Top: magnitude. Bottom: phase. The magnitude has been calculated as  $20 \times \log_{10}(\frac{V_{in}}{V_{ref}})$ , where  $V_{in}$  and  $V_{ref}$  are the voltage signals from the output photodiode and the reference photodiode (see Fig. 4.1).

effective lifetimes calculated in Section 4.1, which are given by

$$\omega_1 = \frac{1}{\tau_1} = B_s P_s^0 (z = L) + \frac{1}{\tau_{21}} \quad (4.26a)$$

$$\omega_2 = \frac{1}{\tau_2} = \frac{1}{\tau_{32}}, \quad (4.26b)$$

where  $\omega_1$  is the inverse of the spontaneous lifetime  $\tau_{21}$  plus an offset dependent on the output power and  $\omega_2$  is the inverse of the spontaneous lifetime  $\tau_{32}$ . Table 4.1 contains the values of  $\tau_1$  and  $\tau_2$  of the model fit to the transfer functions at different output power levels. The mean value of the estimated spontaneous lifetime of the upper energy level was  $\tau_{32} = 7.9 \mu\text{s}$ . Although the data set consisted only of 5 traces, and the measurement bandwidth of  $\sim 150 \text{ kHz}$  was not sufficiently high to have a complete measurement of all

**Table 4.1:** Effective lifetimes  $\tau_1$  and  $\tau_2$  for each measured output signal power level, corresponding to the energy levels  ${}^4I_{13/2}$  and  ${}^4I_{11/2}$ .

	Output power in mW					Mean	Std. dev.
	73	12	163	207	250		
Eff. lifetime $\tau_1$ in $\mu\text{s}$	221.6	145.8	113.5	83.7	69.2	not relevant	not relevant
Eff. lifetime $\tau_2$ in $\mu\text{s}$	8.3	9.1	8.4	6.9	6.8	7.9	1.007



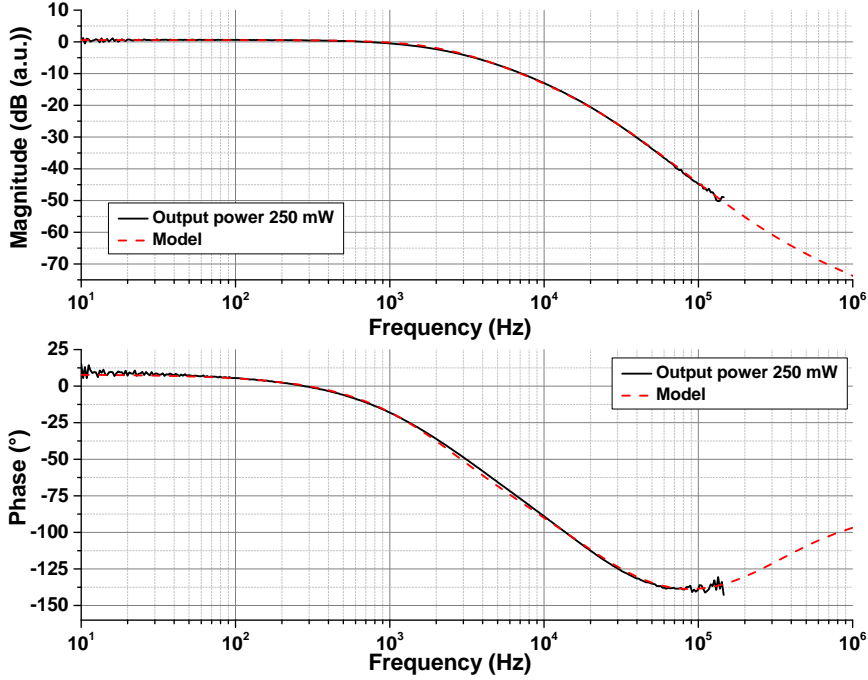


**Figure 4.3:** Pump-to-output-signal transfer function with an output power of 250 mW (black solid line) and corresponding model fit (red dashed line). Top: magnitude. Bottom: phase. The frequency axis is shown up to 1 MHz to observe the model prediction at frequencies higher than measured.

the frequency features, the estimated value is in fair agreement with the value of around  $9 \mu\text{s}$  typically reported in literature [Lay77]. It is worth to mention that  $\tau_{32}$  depends on the glass in which the  $\text{Er}^{3+}$  ions are hosted, and varies significantly for different fibers. The evolution of the cutoff frequency  $\omega_1$  with power is shown in Fig. 4.4. By fitting the expression of  $\omega_1$  shown in Eq. (4.26b) to the data points, the value of  $\tau_{21}$  can be estimated as the inverse of the offset  $\tau_{21} = \omega_1^{-1}$  when  $P_s^0(z = L) = 0$ . In this case the estimated value was  $\tau_{21} = \omega_1^{-1} \approx 8.69 \text{ ms}$ , which is in fairly good agreement with the values commonly reported in literature, which are 8 - 10 ms [San93].

#### 4.2.2 Pump-to-Phase-Shift Transfer Function

One of the techniques proposed to reach high power levels in next-generation GWDs is to coherently combine the output beam from two or more sources. Following this idea, fiber amplifiers have been demonstrated as phase actuators for CBC systems in [Tün11]. In this approach the relative phases between the individual laser sources determines the level of the combined signal. Therefore, it turns important to understand the mechanisms via which the amplifier influences the output phase. In an  $\text{Er}^{3+}$ -doped fiber amplifier, amplitude fluctuations of the pump light produce the fluctuations of the population density in the energy level  ${}^4\text{I}_{11/2}$  as explained in Section 4.1. Given that the transition  ${}^4\text{I}_{11/2} \rightarrow {}^4\text{I}_{13/2}$  is responsible of multiphonon emission due to the quantum defect, the multiphonon rate becomes modulated too. This process leads to a modulation of the heat generated in

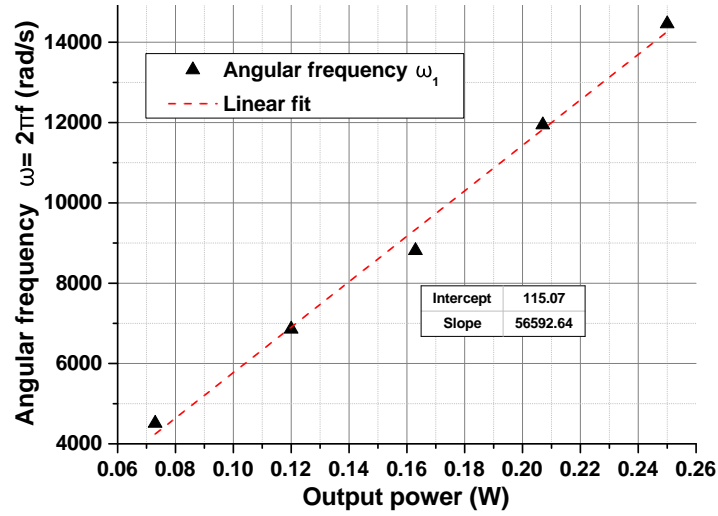


**Figure 4.4:** Evolution of  $\omega_1$  with output power (black triangles) and linear fit (red dashed line).

the fiber, which in turn produces refractive index changes via the thermo-optical effect. Because the optical length depends on the refractive index, it slightly varies, introducing a phase shift to the output signal whose magnitude depends on the transfer function of the population density in the level  ${}^4I_{11/2}$ , on the fiber geometry and on its thermal properties [Bro01; Tün12b]. In order to measure the pump-to-phase-shift transfer function, the experimental setup sketched in Fig. 4.5 was used. A fiber-based Mach-Zehnder interferometer was built with the  $\text{Er}^{3+}$ -doped fiber amplifier described in Section 4.2.1 in one arm and a 40 m-long fiber stretcher (PZ2-PM2-0-131P, *Optiphase*) in the other arm.

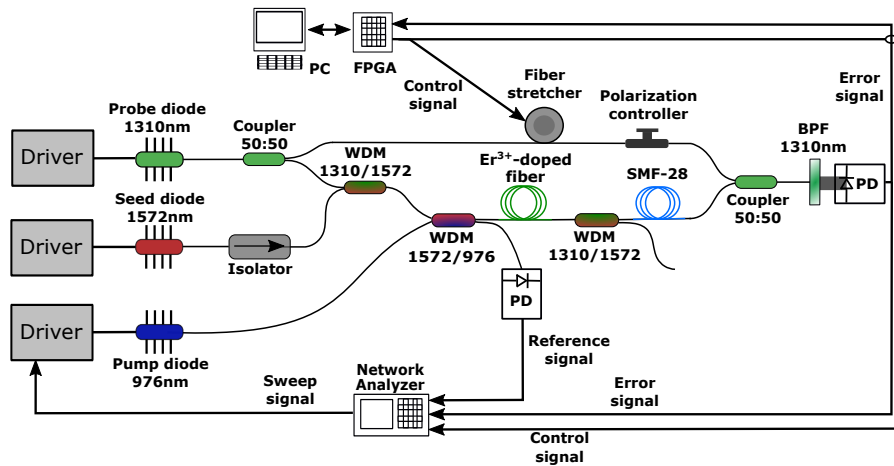


**Figure 4.5:** Experimental setup to measure the pump-to-phase-shift transfer function. FPGA: Digilock field programmable gate array, WDM: wavelength division multiplexer, PD: photodiode, BPF: bandpass filter.

The light from a DFB diode at 1310 nm and MHz-scale linewidth was coupled as a probe signal to both arms by a 50:50 tap coupler. In order to separate the amplifier signal at 1572 nm from the probe signal at 1310 nm, an outcoupling WDM was spliced behind the amplifier. In addition, a piece of  $\sim 26$  m of single-mode passive fiber (SMF-28) was spliced to compensate the difference of the arms lengths and reduce the coupling of frequency noise from the probe signal to the interferometer output. In the passive arm, a polarization controller was included to enhance the interference contrast. Finally, the interferometer was closed with another 50:50 tap coupler. A bandpass filter centered at 1310 nm with a bandwidth of 12 nm was used to suppress any residual pump or seed light from the amplifier. Finally, the intensity of the interference signal, which depends on the relative phases of the probe signal between the arms, was sensed with an InGaAs photodetector (DET01CFC, *Thorlabs*) with a 1.2 GHz bandwidth. Similar to the setup in Section 4.2.1, the sweep signal from the network analyzer was used to modulate the current of the pump diode, and the small amount of pump light in the secondary port of the incoupling WDM was detected by another InGaAs photodetector (DET01CFC, *Thorlabs*) as a reference. A commercial feedback controller (Digilock-110, *Toptica Photonics*) was used to stabilize the output power of the interferometer by compensating the differential phase shift via the stretcher. The pump-to-phase-shift transfer function was measured using a sample of the control signal fed to the stretcher in the frequency range where the stabilization loop had gain to lock the interferometer, whilst the error signal from the photodiode was used at frequencies at which the stabilization loop did not have enough gain to lock the interferometer. Hence, the maximum measurable frequency was limited by the sensitivity of the photodiode to discern the modulation in the signal. Besides the measurements, a simulation of the temperature-induced phase shift in the amplifier was performed using a simulation tool previously developed in the Laser Development Department at LZH [Tün12b]. The simulation assumed a modulated heat generation in the core of the fiber and calculates its radial propagation depending on the geometry and thermal properties of the fiber. The physical mechanism that originates the heat is ignored as well as other mechanisms not related to temperature such as Kramers-Kronig relations (KKR) [Dig97].

The magnitude of the measured phase shift is plotted together with the simulated temperature-induced phase shift in Fig. 4.6(a). The simulation matches quite well the experimental measurement up to approximately 20 kHz. This demonstrates that the phase shift is temperature-induced, and therefore attributable to the population inversion modulation of the energy level  $^4I_{11/2}$ . A clear mismatch between simulation and measurement can be observed at frequencies above 20 kHz. Although the frequency response of the phase shift depends on many parameters that were not accurately known (e.g., thermal conductivity, heat transfer coefficient, core/cladding disuniformities along the fiber, etc), this behavior could not be reproduced by the simulation with any realistic combination of these parameters. Fig. 4.6(b) shows more closely the frequency range of this phenomenon. The disagreement between the measurement and the simulation occurs because, as mentioned before, the simulation does not take into account the physical process that generates the heat, but only its radial propagation in the fiber. Therefore, it can be assumed that this effect is due to a lower modulation of the heat generated in the fiber as a consequence of a lesser reaction of the population in the upper energy level to the pump modulation. In

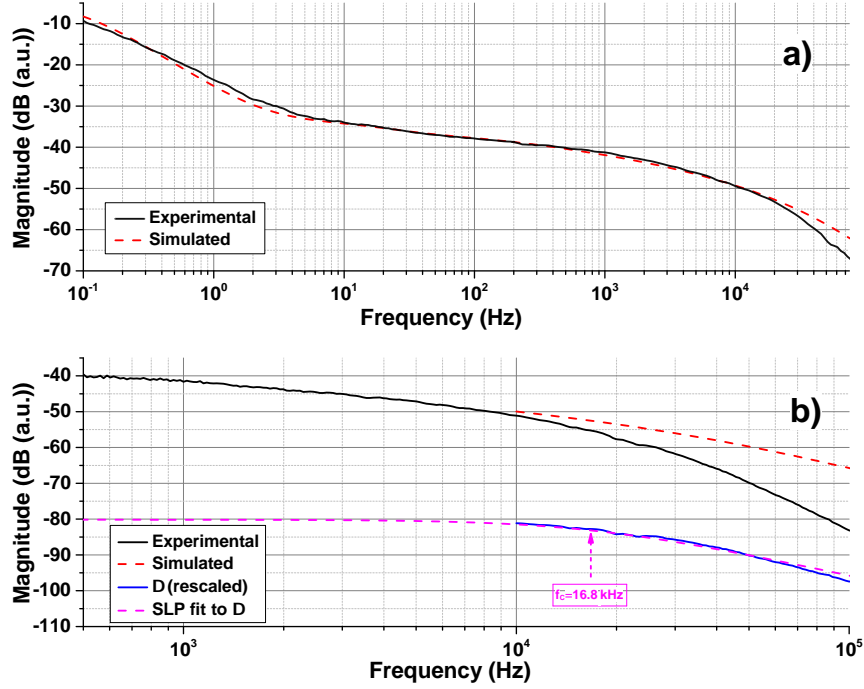


**Figure 4.6:** Magnitude of the pump-to-phase-shift transfer function. Top: measured phase shift (black solid line) and simulated temperature-induced phase shift (red dashed line). Bottom: detail of the disagreement between experimental data and simulation, difference between them (blue solid line) and a single low-pass fit to it (magenta dashed line).

other words, the difference between the measured and the simulated transfer functions is a good approximation of the transfer function of the population density of the energy level  ${}^4I_{11/2}$ . As calculated in Section 4.1, this transfer function corresponds to a single low-pass (the first term of Eq. 4.22) with cutoff frequency  $f_c = \frac{1}{2\pi\tau_{32}}$ . Fig. 4.6(b) includes the calculated difference (named  $\Delta$ ) between the simulated and the measured transfer functions, and a single low-pass function fit to it (named *SLP*). The cutoff frequency was  $f_c \approx 16.8$  kHz, equivalent to a lifetime of  $\tau_{32} \approx 9.4$   $\mu$ s.

#### 4.2.3 Summary

In this section, the suitability of the analytical model developed in Section 4.1 has been validated, and some aspects of the temporal dynamics of Er<sup>3+</sup>-doped fiber amplifiers have been studied. It was demonstrated that the pump-to-output-signal transfer function is a low-pass multiplied by a damped low-pass at the power levels achieved in the experiments. Moreover, the effective lifetime of the metastable energy level  ${}^4I_{13/2}$  decreases with increasing output power as the model predicts, increasing the cutoff frequency of the transfer functions accordingly. This feature was exploited to estimate the value of the spontaneous lifetime as a resource to validate the reliability of the model. The estimate of the spontaneous lifetime was 8.69 ms, which is in agreement with the available data from literature. It is

worth to mention the possibility of estimating the parameter  $B_s$  (see Eqs. 4.24b and 4.24d) if the effective lifetime is known (by measuring it). Although this feature was not studied in detail in the frame of this thesis, it would, in principle, allow the estimation of the  $\sigma_s^{\text{abs}}$  and  $\sigma_s^{\text{em}}$  cross sections. The lifetime of the energy level  ${}^4\text{I}_{11/2}$  was also estimated to verify the model. Using the measured pump-to-output-signal transfer functions the value of  $\tau_{32}$  was  $7.9 \mu\text{s}$ , which is also within the common values reported in the literature.

The comparison of the pump-to-phase-shift transfer function with the simulations revealed that the phase shift in an  $\text{Er}^{3+}$ -doped fiber amplifier is induced by temperature generated due to the quantum defect in the core of the fiber up to  $\approx 20\text{kHz}$ . Up to this frequency, the magnitude of the phase shift depends on how the heat propagates in the fiber, and therefore on the geometry and thermal properties of it. The crosscheck with the simulations suggested that above  $\approx 20\text{kHz}$  the transfer function of the energy level  ${}^4\text{I}_{11/2}$  becomes dominant. This allowed to estimate the lifetime of this energy level also by means of the pump-to-phase-shift transfer function, which resulted to be  $\approx 9.4 \mu\text{s}$ . Although the difference of the values of  $\tau_{32}$  estimated from the pump-to-output transfer function and the pump-to-phase-shift is not negligible, both values are within the range commonly reported in literature. The experiments have shown that the simplification of the rate equations by neglecting the up-conversion is a good approximation. Also, the phase shift induced by KKR has been ignored. KKR is expected to have a noticeable impact at sufficiently high frequencies [Dig97]. In any case, the analytical model presented here reflects the temporal dynamics of  $\text{Er}^{3+}$ -doped fiber amplifiers fairly well, and can be a useful tool to predict their temporal behavior.

### 4.3 Further Analysis Using the Model

In Section 4.2 it was experimentally demonstrated that the cutoff frequency of the pump-to-output transfer function has a linear dependency on the output power. However, as can be inferred from Eq. 4.22, the frequency response also depends on the cross sections  $\sigma_s^{\text{abs}}$  and  $\sigma_s^{\text{em}}$ , and therefore on the seed wavelength. More specifically, the seed wavelength directly influences the value of  $\omega_3$  and  $\omega_1$  via the parameter  $B_s$ . The impact of seeding with different wavelengths could not be observed using the setup shown in Fig. 4.1 since the seed wavelength was not tunable. Other interesting effects, e.g., the conditions  $\omega_1 = \omega_2$  and  $\omega_1 = \omega_3$ , could also not be tested. In this section, the aforementioned conditions that could not be experimentally observed are studied using the analytical model developed in Section 4.1 to simulate the pump-to-output-signal transfer function of  $\text{Er}^{3+}$ -doped fiber amplifiers.

As a reminder, Eq. 4.22 can be expressed compactly as

$$\frac{m_s}{m_p} e^{i\phi_s} = \frac{K}{\omega_2 + i\omega} \left( \frac{\omega_3 + i\omega}{\omega_1 + i\omega} \right) \quad (4.27)$$

where  $K$ ,  $\omega_1$ ,  $\omega_2$  and  $\omega_3$  are given by

$$K = P_p^0(z=0) \frac{\Gamma_s \sigma_s^{\text{abs}}}{A_c} \quad (4.28a)$$

$$\omega_1 = B_s P_s^0(z=L) + \frac{1}{\tau_{21}} \quad (4.28b)$$

$$\omega_2 = \frac{1}{\tau_{32}} \quad (4.28c)$$

$$\omega_3 = \frac{B_s A_c}{\Gamma_s \sigma_s^{\text{abs}}} \frac{1}{\tau_{32}} + \frac{1}{\tau_{21}}. \quad (4.28d)$$

Representing the evolution of  $\omega_1, \omega_2$  and  $\omega_3$  with output power, three regimes can be distinguished depending on their values: Regime 1 where  $\omega_1$  is lower than  $\omega_2$ . Regime 2 where  $\omega_1$  falls between  $\omega_2$  and  $\omega_3$ . And regime 3 where  $\omega_1$  is higher than  $\omega_3$ . As a result, the power thresholds  $P_{\text{th1}}$  and  $P_{\text{th2}}$  can be defined as the power levels at which  $\omega_1 = \omega_2$  and  $\omega_1 = \omega_3$ , which correspond to the conditions in which the term  $\frac{\omega_3 + i\omega}{\omega_1 + i\omega}$  in Eq. 4.27 becomes a damped low-pass and a damped high-pass. This is illustrated in Fig. 4.7(a). Note that this

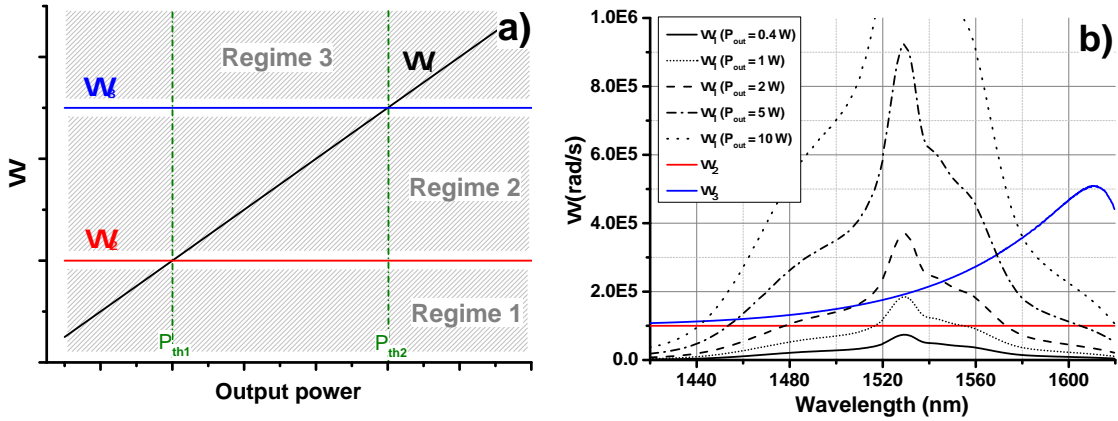


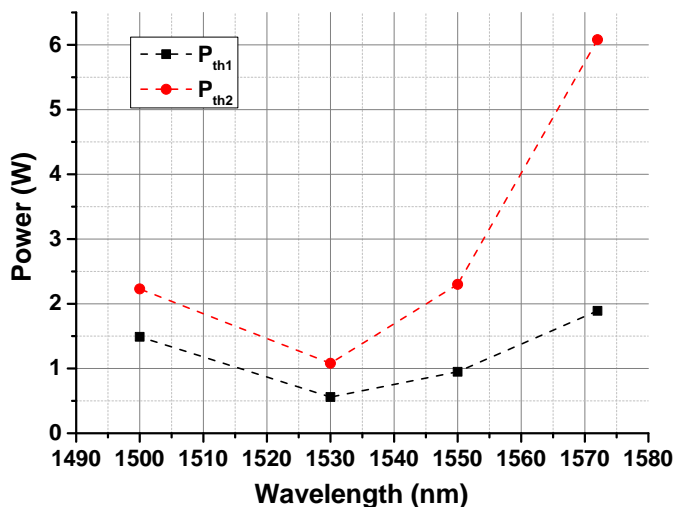
**Figure 4.7:** (a): Evolution of  $\omega_1, \omega_2$  and  $\omega_3$  with output power. The different regimes are shaded and the power thresholds at which  $\omega_1 = \omega_2$  and  $\omega_1 = \omega_3$  are marked. (b): Evolution of  $\omega_1$  (at different output power levels),  $\omega_2$  and  $\omega_3$  with seed wavelength.

representation is valid for a certain seed wavelength because  $\omega_2$  and  $\omega_3$  are independent of the output power but not of the seed wavelength. Such relation taking into account the seed wavelength is represented in Fig. 4.7(b) at different output power levels for the sake of completeness. Hence,  $P_{\text{th1}}$  and  $P_{\text{th2}}$  are not constant but vary with seed wavelength. Their values were computed setting the condition  $\omega_1 = \omega_2$  and  $\omega_1 = \omega_3$  for four different wavelengths. Table 4.2 contains the value of the parameters used in the simulations. The power thresholds  $P_{\text{th1}}$  and  $P_{\text{th2}}$  that make the term  $\frac{\omega_3 + i\omega}{\omega_1 + i\omega}$  become either a damped low-pass or a damped high-pass are shown in Fig. 4.8 as a function of the seed wavelength. A noticeable difference in their evolution becomes evident the longer the wavelength is. As an illustrative example let us assume an application where the pump-to-output-signal frequency response of a fiber amplifier is desired to be a single low-pass in a wide frequency range and the wavelength can be chosen to favor this feature. In this context  $\omega_1 = \omega_3$

**Table 4.2:** Fiber parameters used in the computation of  $P_{th1}$ ,  $P_{th2}$  and transfer functions.

Parameter	Value			
$\lambda_s$	1500 nm	1530 nm	1550 nm	1572 nm
$\sigma_s^{abs}$	$3.37 \times 10^{-25} \text{ m}^2$	$6.83 \times 10^{-25} \text{ m}^2$	$3.16 \times 10^{-25} \text{ m}^2$	$1.18 \times 10^{-25} \text{ m}^2$
$\sigma_s^{em}$	$1.66 \times 10^{-25} \text{ m}^2$	$6.38 \times 10^{-25} \text{ m}^2$	$4.47 \times 10^{-25} \text{ m}^2$	$2.61 \times 10^{-25} \text{ m}^2$
$\Gamma_s$	1			
$A_c$	$56.74 \mu\text{m}^2$ ( $d_c = 8.5 \mu\text{m}$ )			
$\tau_{32}$	10 $\mu\text{s}$			
$\tau_{32}$	10 ms			

would effectively cancel the effect of both,  $\omega_1$  and  $\omega_3$ , reducing the transfer function to a single low-pass at the output power of  $P_{th2}$ . Here, an amplifier at 1530 nm would require an output power of only 1.08 W, whereas at 1572 nm the goal would be 6.08 W. Of course other factors that should be considered in a real system come into play. For example how challenging it is to obtain 1.08 W at 1530 nm versus 6.08 W at 1572 nm in a purely single mode fiber given its cross sections and the available pump power. Also, the application for which the amplifier is designed might require more than 1.08 W but less than 6.08 W, in which case an amplifier at 1572 nm could be implemented followed by power tuning stage. In any case, setting the output power aiming to obtain the desired transfer function

**Figure 4.8:** Evolution of  $P_{th1}$  and  $P_{th2}$  with seed wavelength.

can increase the complexity the system. Thus, it is also interesting to know in advance how the frequency response behaves for different sets of wavelength and output power. To simulate this, the output power was set such that  $\omega_1$  was within the different regimes shown in Fig. 4.7(a). The results are shown in Fig. 4.9 for different seed wavelengths and different output power levels. As mentioned before and experimentally demonstrated in Section 4.2, amplifiers operating at higher output power levels yield transfer functions with cutoff frequencies at higher frequencies. This happened also for the other simulated

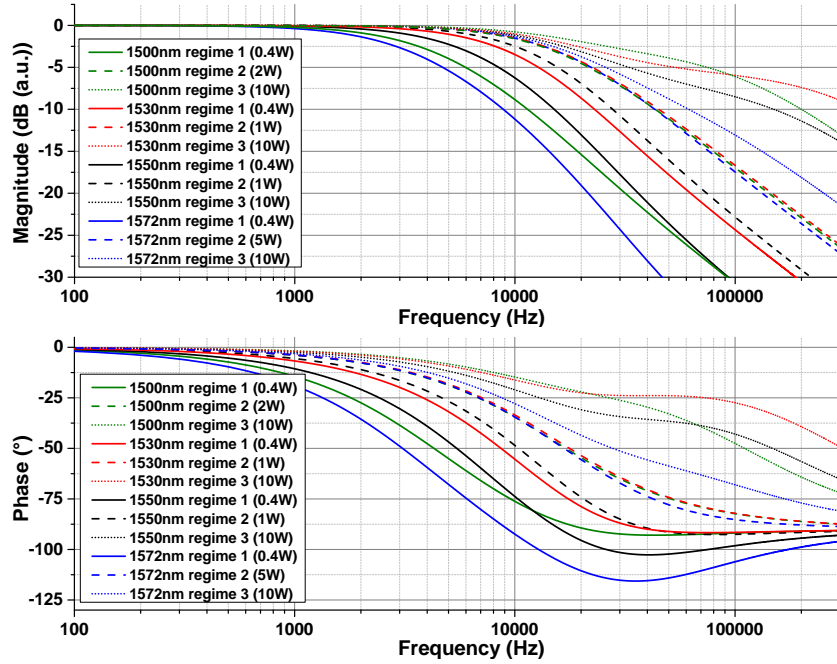


**Figure 4.9:** Computed pump-to-output-signal transfer functions in an Er<sup>3+</sup>-doped fiber amplifier for different seed wavelengths and regimes. Top: magnitude. Bottom: phase. The legend includes the output power in each case.

wavelengths as can be seen in Fig. 4.9. Besides this, there is not a linear trend between the signal wavelength and the bandwidth of the frequency response, but it seems that the bandwidth is larger the closer the wavelength is to 1530 nm. This can be also inferred from Fig. 4.7(b) and is a consequence of the Er<sup>3+</sup> cross sections. The shape of the transfer function also changes significantly. This is particularly visible in amplifiers operating in the regime 3, i.e., when  $\omega_1 > \omega_3$  (in Fig. 4.9 all at 10 W). In this case there is a plateau effect that reduces the falling slope for some hundreds of kHz. In the simulations, the transfer function of the amplifier at 1500 nm kept having a higher magnitude up to 100 kHz. Above this frequency the magnitude of the amplifier at 1530 nm was noticeably higher. Regarding the phase, it is easily demonstrable that all cases end with a phase shift of  $-90^\circ$ . However, the maximum phase shift is lower the higher the output power levels are and the closer the seed wavelength is to 1530 nm. For example, the amplifier at 1572 nm operating in the regime 1 exhibits a maximum phase shift of  $\approx -115^\circ$  and a phase damping effect, whereas at 1530 nm the maximum phase shift is  $-90^\circ$  without damping effect. Likewise, any configuration operating in the regimes 2 or 3 do not exhibit phase shifts larger than  $-90^\circ$ . Furthermore, the differences in the frequency responses when the amplifier is in the regime 2 are very small. It can be noted that the behavior at 1500 nm, 1530 nm and 1572 nm are practically identical despite the considerable different power levels of 2 W, 1 W and 5 W, respectively.



#### 4.4 Conclusion

An analytical model of the temporal dynamics of  $\text{Er}^{3+}$ -doped fiber amplifiers has been developed and studied for the first time. It was discovered that the pump-to-output transfer function is a low-pass multiplied by a term that can be a damped low-pass or a damped high-pass depending on the output power. The model has been experimentally verified by two different means. The first consisted on measuring the pump-to-output transfer function for different output power levels and fitting the model to them. The estimated spontaneous lifetimes of the energy levels  ${}^4\text{I}_{11/2}$  and  ${}^4\text{I}_{13/2}$  were in agreement with the results reported by other authors. For the second experimental test, the pump-to-phase-shift transfer function in the  $\text{Er}^{3+}$ -doped fiber amplifier was studied. The comparison with the simulated temperature-induced transfer function permitted a second estimation of the spontaneous lifetime of the  $\text{Er}^{3+}$  energy level  ${}^4\text{I}_{11/2}$ , which was also reasonably close to the values reported by other groups. A small difference between the two estimations of the  ${}^4\text{I}_{11/2}$  lifetime can be attributed to the limitations of the two different experimental setups (i.e., pump-to-output and pump-to-phase-shift transfer functions), especially to the lack of data to fit the model above 150 kHz.

The possibility to simulate the pump-to-output transfer functions allows estimating how the pump fluctuations will couple to the output signal for given certain fiber amplifier parameters. At the same time, it can potentially be used to predict the frequency response of the fiber amplifier to stabilization systems based on feedback loops to the pump power. Thus, in addition to the aforementioned experimental investigations, the model was employed to study the conditions that could not be reproduced in the experiments. The power levels at which the pump-to-output-signal transfer function becomes a single low-pass and a low-pass multiplied by a damped low-pass were calculated for different wavelengths and the transfer function was simulated when  $\omega_1$  (i.e., the inverse of the effective lifetime of the energy level  ${}^4\text{I}_{13/2}$ ) falls within each of the defined regimes at different wavelength. The simulations show that the transfer function can be tailored by selecting the seed wavelength and tuning the output power.



## CHAPTER 5

---

### *Off-Peak* Pumped High Power Fiber Amplifier Oriented to Next-Generation GWDs

---

As aforementioned in Chapter 2, an important limitation regarding the power scaling of  $\text{Er}^{3+}:\text{Yb}^{3+}$ -codoped fiber amplifiers is the  $\text{Yb}^{3+}$ -band ASE that such amplifiers generate at high pump power levels. This happens when the  $\text{Yb}^{3+}$  population inversion is so high that there is not a sufficient number of  $\text{Er}^{3+}$  ions in the ground state to accept energy from excited  $\text{Yb}^{3+}$  ions. The  $\text{Yb}^{3+}$ -to- $\text{Er}^{3+}$  energy transfer efficiency then drops and the energy is released around  $1\ \mu\text{m}$ , i.e., in the  $\text{Yb}^{3+}$  emission band. Besides degradation of the optical efficiency, and consequently a gain limitation, the presence of  $\text{Yb}^{3+}$ -ASE tends to lead to parasitic lasing, self-pulsing and even the formation of giant pulses, which can turn the amplifier unstable at  $1.5\ \mu\text{m}$  [Sob11] and poses a risk to the integrity of the system. This problem cannot be circumvented by increasing the  $\text{Er}^{3+}$  doping concentration without falling into issues related to clustering. Thus, this limitation must be treated differently. In general, the problem primarily arises due to the high absorption cross section of  $\text{Yb}^{3+}$  around  $976\ \text{nm}$ . Therefore it would be more suitable if the pump power absorption were lower, so that it distributes more evenly along the fiber. An interesting approach to achieve this is the *off-peak* pumping scheme [Cre16]. The idea consists in pumping at a wavelength different from that of the maximum absorption in order to locally reduce the  $\text{Yb}^{3+}$  inversion level and distribute the pump light absorption more homogeneously along the fiber. Although reducing the absorption deliberately may seem counterintuitive when pursuing higher power levels, it effectively enhances the  $\text{Yb}^{3+}$ -to- $\text{Er}^{3+}$  energy transfer efficiency and reduces the  $\text{Yb}^{3+}$ -band ASE, which allows to pump with higher power levels [Cre16; Var17a].

In this Chapter the *off-peak* pumping scheme is applied to a high power  $\text{Er}^{3+}:\text{Yb}^{3+}$ -codoped fiber amplifier oriented to next-generation GWDs. Since the most beneficial pump wavelength was not known a priori, the behavior of an EYDFA was numerically simulated considering the wavelength of commercially available high power pump diodes, namely  $915\ \text{nm}$ ,  $940\ \text{nm}$  and  $976\ \text{nm}$ . The results of these simulations are shown in Section 5.1. Then, in Section 5.2 a monolithic laboratory prototype of a high power  $\text{Er}^{3+}:\text{Yb}^{3+}$ -codoped fiber amplifier pumped at  $940\ \text{nm}$  is experimentally demonstrated and thoroughly characterized regarding the relevant aspects of GWDs for the first time. This characterization includes optical efficiency, beam quality, relative power noise, frequency noise and power stability. The experiment demonstrated for the first time up to  $100\ \text{W}$  in a linearly-polarized  $\text{TEM}_{00}$  mode with an all-fiber system free of SBS and  $\text{Yb}^{3+}$ -band ASE.

The results presented in this chapter have been published beforehand [Var17a; Var17b].

## 5.1 Simulations

This section presents the simulation results regarding the output power and the Yb<sup>3+</sup>-band ASE of an Er<sup>3+</sup>:Yb<sup>3+</sup>-codoped fiber amplifier at 1556 nm pumped at 915 nm, 940 nm and 976 nm. The amplifier is cladding-pumped in counterpropagation direction. The goal was to analytically verify the assumption that the *off-peak* pumping scheme has a positive impact on the power scaling and effectively reduces the Yb<sup>3+</sup>-band ASE as well as to choose the pump wavelength to be used in the experimental setup later shown in Section 5.2. The simulation tool used for this analysis has been developed in the Laser Development Department at LZH [Boo18].

The energy level diagram and relevant transitions of an Er<sup>3+</sup>:Yb<sup>3+</sup>-doped fiber amplifier pumped at 9xx nm were shown in Chapter 3 (see Fig. 3.6) and the corresponding rate equations were presented in Eqs. 3.8. For the sake of simplification, the back-transferred energy parameter ( $R_{3b}$ ) can be neglected in the simulations due to its very small impact on the results. The up-conversion ( $C_{up}$ ) coefficient can also be omitted at the expense of the absolute power levels for further simplification. Therefore, from a practical point of view, Eqs. 3.8a, 3.8d and 3.8f provide redundant information and can be neglected. Thus, the set of equations to describe the Er<sup>3+</sup>:Yb<sup>3+</sup>-codoped system can be reduced to

$$\frac{\partial n_2}{\partial t} = n_1 W_{12} - \frac{n_2}{\tau_{21}} - n_2 W_{21} + \frac{n_3}{\tau_{32}} \quad (5.1a)$$

$$\frac{\partial n_3}{\partial t} = n_1 W_{13} - n_3 W_{31} - \frac{n_3}{\tau_{32}} + n_b n_1 R_{b3} N_{Yb} \quad (5.1b)$$

$$n_1 = 1 - n_2 - n_3 \quad (5.1c)$$

$$\frac{\partial n_b}{\partial t} = n_a W_{ab} - n_b W_{ba} - \frac{n_b}{\tau_{ba}} - n_b n_1 R_{b3} N_{Er} \quad (5.1d)$$

$$n_a = 1 - n_b. \quad (5.1e)$$

The power evolution of the pump, seed and Yb<sup>3+</sup>-band ASE signals along the fiber in steady-state condition are given by [Han10]

$$\frac{\partial P_p}{\partial z} = [n_b c_{ba}(\lambda_p) - n_a c_{ab}(\lambda_p) - n_1 c_{13}(\lambda_p)] P_p \quad (5.2a)$$

$$\frac{\partial P_s}{\partial z} = [n_2 c_{21}(\lambda_1) - n_1 c_{12}(\lambda_s)] P_s \quad (5.2b)$$

$$\frac{\partial P_{Yb,k}}{\partial z} = [n_b c_{ba}(\lambda_k) - n_a c_{ab}(\lambda_k) - n_1 c_{13}(\lambda_k)] P_{Yb,k} + \frac{2hc^2}{\lambda_k^3} n_b c_{ba} \Delta\lambda, \quad (5.2c)$$

were  $P_p$  and  $P_s$  are the power levels of the pump and the seed,  $P_{Yb,k}$  is the power of the Yb<sup>3+</sup>-band ASE in the  $k$ -th spectral slot,  $h$  is the Planck constant,  $c$  is the speed of light in vacuum,  $z$  is the longitudinal position in the fiber,  $\Delta\lambda$  is the width of the spectral slot used for computational reasons and  $c_{ij}$  are the wavelength-dependent emission and absorption coefficients defined as

$$c_{12}(\lambda_s) = \Gamma_s \sigma_{\text{Er}}^{\text{abs}}(\lambda_s) N_{\text{Er}} \quad (5.3a)$$

$$c_{21}(\lambda_s) = \Gamma_s \sigma_{\text{Er}}^{\text{em}}(\lambda_s) N_{\text{Er}} \quad (5.3b)$$

$$c_{13}(\lambda_p) = \Gamma_p \sigma_{\text{Er}}^{\text{abs}}(\lambda_p) N_{\text{Er}} \quad (5.3c)$$

$$c_{ba}(\lambda_p) = \Gamma_p \sigma_{\text{Yb}}^{\text{em}}(\lambda_p) N_{\text{Yb}} \quad (5.3d)$$

$$c_{ab}(\lambda_p) = \Gamma_p \sigma_{\text{Yb}}^{\text{abs}}(\lambda_p) N_{\text{Yb}}, \quad (5.3e)$$

where  $\Gamma_{p,s}$  is the spatial overlap of the pump or the seed with the core calculated as shown in Eq. 4.3,  $\sigma_{\text{Yb/Er}}^{\text{abs/em}}(\lambda)$  is the absorption or emission cross section of  $\text{Er}^{3+}$  or  $\text{Yb}^{3+}$  at a given wavelength and  $N_{\text{Yb/Er}}$  is the  $\text{Er}^{3+}$  or  $\text{Yb}^{3+}$  doping concentration.

The length of the active fiber was chosen such that 95 % of the pump power was absorbed, and the pump power was increased as long as the differential optical efficiency was more than 10 % ( $\frac{\Delta P_s}{\Delta P_p} > 0.1$ ). A summary of the parameters used in the simulations of a representative  $\text{Er}^{3+}:\text{Yb}^{3+}$ -codoped fiber amplifier are shown in Table 5.1.

**Table 5.1:** Parameters used in the simulation of the power level in an  $\text{Er}^{3+}:\text{Yb}^{3+}$ -codoped fiber amplifier.

Parameter	Value
$\lambda_s$	1556 nm
$P_s$	2 W
$\lambda_p$	915 nm, 940 nm, 976 nm
$\tau_{21}$	10 ms
$\tau_{32}$	10 $\mu$ s
$\tau_{ba}$	1 ms
$N_{\text{Er}}$	$2.450 \times 10^{25}$ ions $\text{m}^{-3}$
$N_{\text{Yb}}$	$3.526 \times 10^{26}$ ions $\text{m}^{-3}$
$R_{b3}$	$2.371 \times 10^{-22}$ $\text{m}^{-3}$ s/ion [Han10]
$r_{\text{core}}$	12.5 $\mu$ m
$r_{\text{cladding}}$	150 $\mu$ m
$\text{NA}_{\text{core}}$	0.09

The simulation cannot accurately compute the absolute power levels because of two main reasons. First, the exact values of some parameters were not known for the fiber of the experimental setup presented later, and therefore a mismatch can be expected. For example, the absorption and emission cross sections of the active fiber were not provided by the manufacturer. To proceed with the simulations the cross sections from a commercial software (Liekki Application Designer) were used [Reb97]. Another example of a not well known parameter is the  $\text{Yb}^{3+}$ -to- $\text{Er}^{3+}$  energy transfer ( $R_{b3}$ ). This parameter is currently object of investigations and there is no consensus about its value [Lim17; Ste18]. The second reason why the absolute power levels cannot be computed is the aforementioned simplification of the rate equations by neglecting the backtransferred energy ( $R_{3b}$ ) and up-conversion ( $C_{\text{up}}$ ), which can have important effects when highly doped fibers are strongly pumped. In Fig. 5.1 are shown the computed normalized output power and the normalized  $\text{Yb}^{3+}$ -band ASE versus the normalized pump power for the pump wavelengths

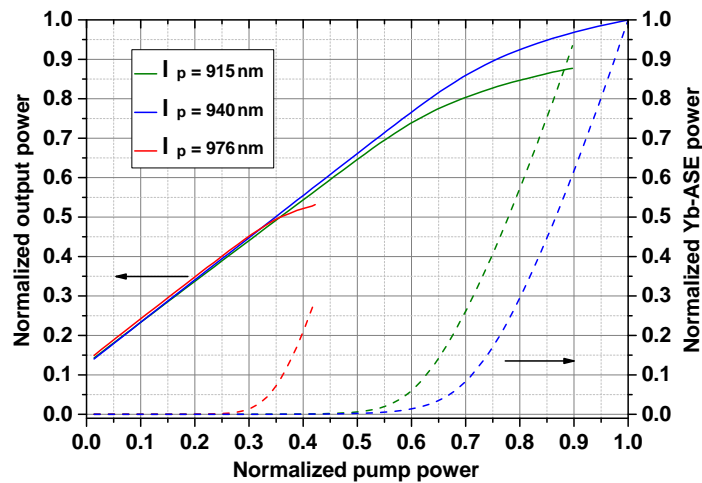


**Figure 5.1:** Results of the simulation for the pump wavelengths of 915 nm, 940 nm and 976 nm in green, blue and red. The solid curves represent the amplifier output power at 1.5  $\mu\text{m}$  (left axis) and the dashed curves are the power levels of the  $\text{Yb}^{3+}$ -band ASE (right axis).

of 915 nm, 940 nm and 976 nm. The output power and  $\text{Yb}^{3+}$ -band ASE were normalized with the maximum output power and ASE of the three cases whereas the pump power was normalized with the maximum pump power. The highest output power  $P_{\text{max}}$  was obtained with the amplifier pumped at 940 nm. In this case the fiber length was 2.9 m. At low pump power levels the slope efficiency was practically the same in the three cases. However, the onset of  $\text{Yb}^{3+}$ -band ASE occurred at a significantly lower pump power level when the amplifier was pumped at 976 nm. Because of this, the ASE builds up earlier and the output power slope starts to roll-off. The maximum output power was  $\sim 0.53P_{\text{max}}$  and the fiber length was 0.7 m. The performance of the amplifier pumped at 915 nm was better than the one pumped at 976 nm, since it provided up to  $\sim 0.87P_{\text{max}}$  with a fiber length of 2 m. The results match with the conceptual idea of the *off-peak* pumping method, which consists on pumping at a wavelength different to that of the maximum absorption to pump with higher power before saturating the  $\text{Yb}^{3+}$ -to- $\text{Er}^{3+}$  energy transfer mechanism. The drawback was the expected: the lower absorption requires the fiber to be longer to obtain the same absolute pump absorption. In any case, the simulation suggests that pumping either at 915 nm or 940 nm provides a benefit in terms of power scaling compared to pumping at the most common wavelength of 976 nm. Thus, the experimental setup, which is presented in the following section, was pumped at 940 nm.

## 5.2 Experiments

The high power  $\text{Er}^{3+}:\text{Yb}^{3+}$ -codoped fiber amplifier shown in Fig. 6.1 was built to verify the aforementioned concept. It consisted of a double-clad  $\text{Er}^{3+}:\text{Yb}^{3+}$ -codoped LMA fiber (LMA-EYDF-25P/300HE, *Nufern*) pumped in counter-propagation direction by two high power pump diodes with an output power of 140 W at 940 nm (LT-Series, *Lumentum*). To seed the amplifier, a fiber laser (Rock, *NP Photonics*) at 1556 nm was used. The seed

module delivered up to 2 W of polarized light ( $\text{PER} > 23 \text{ dB}$ ) and kHz-scale linewidth. The output of the seed module was delivered through a single-mode connectorized fiber, and therefore it was easily integrable in an all-fiber system. However, in order to keep the seed module intact for other future experiments it was free-space coupled to the fiber amplifier. This incoupling stage included an isolator, beam-walking mirrors and mode-matching lenses as shown in Fig. 6.1. The light leaking in transmission from one of the mirrors was used for testing and monitoring purposes. To mimic an all-fiber system, the seed light was coupled to a single-mode fiber instead of the passive matching LMA fiber. This also prevented the excitation of HOMs. An in-home-made mode field adapter (MFA) was used to fit the mode field of the single-mode fiber to the passive LMA fiber. Since the amplifier was pumped in counter-propagation direction, an in-home-made cladding light stripper (CLS) [Wys18] was spliced behind the MFA to remove any residual pump light in the cladding. The available seed power at the  $\text{Er}^{3+}:\text{Yb}^{3+}$ -codoped fiber was  $\sim 1.2 \text{ W}$ . The length of the active fiber was  $\sim 5.5 \text{ m}$ . The pump combiner (PC) was an in-home-made  $(2 + 1) \times 1$  [The12b] with an overall pump coupling efficiency of  $\sim 90\%$  fabricated with the matching passive fiber (LMA-GFD-25/300, *Nufern*). The active fiber was spooled in a V-grooved aluminum coil

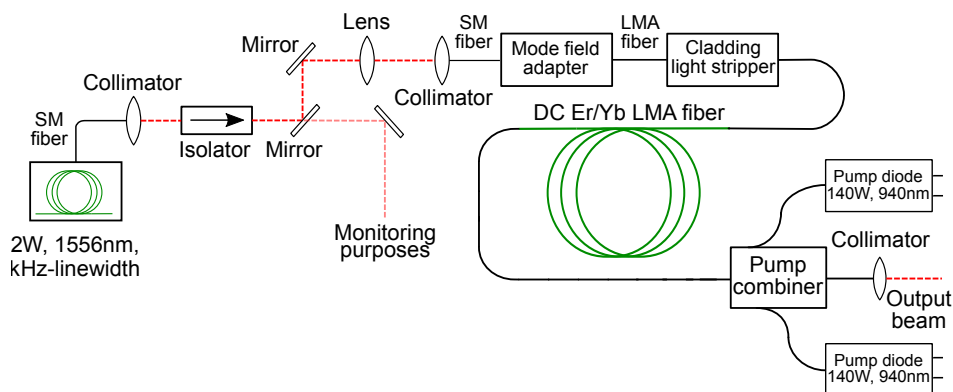


**Figure 5.2:** Experimental setup of the  $\text{Er}^{3+}:\text{Yb}^{3+}$ -codoped fiber amplifier *off-peak* pumped at 940 nm. SM: single-mode, LMA: large mode area, DC: double-clad.

of 30 cm diameter. Approximately 15 cm of the low refractive index polymer coating of the output fiber was removed and substituted by high refractive index optical gel in order to remove any potential light guided in the cladding in forward direction.

The goal of the designed laboratory prototype was to study the suitability of *off-peak* pumped fiber amplifiers as high power stages in laser systems for next-generation GWDs. As it was previously discussed in Chapter 2, a suitable laser source should address not only high output power but a number of different requirements. The following subsections present the measurement results regarding the optical slope and spectrum, power and PER stability, modal content, relative power noise, frequency noise and indications of SBS.

### 5.2.1 Optical Slope and Spectrum

The measured output power versus the pump power available in the active fiber (i.e., considering the 90 % coupling efficiency of the PC) is presented in Fig. 5.3(a). The maximum output power was 111 W, limited by the available pump power. At this power level the gain of the amplifier was 19.7 dB. The optical efficiency was 46.2 %, close to the theoretical quantum limit of  $\sim 60\%$  for pump and seed wavelengths of 940 nm and 1556 nm. Even though the quantum defect is slightly higher for pumping at 940 nm compared to 976 nm, the achieved output power is significantly higher than in  $\text{Er}^{3+}:\text{Yb}^{3+}$ -codoped fiber amplifiers with similar characteristics pumped at 976 nm [Ste14b]. Furthermore, the optical efficiency was also higher than the reported in systems with  $\text{Yb}^{3+}$ -band ASE suppression schemes ( $\sim 40\%$  [Han15]) as well as in  $\text{Er}^{3+}:\text{Yb}^{3+}$ -codoped fiber lasers ( $\sim 43\%$  [She05]). The output

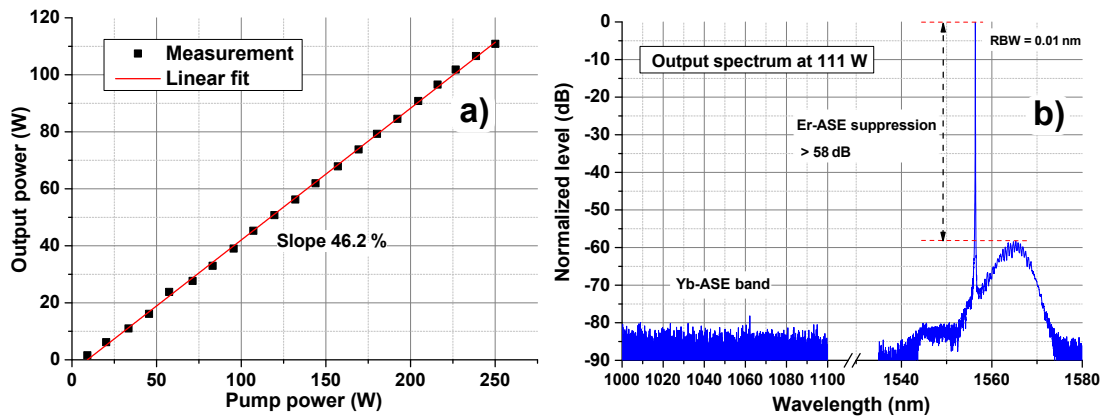


**Figure 5.3:** (a): Optical-to-optical slope. Squares: experimental data. Line: linear fit to the data. The slope efficiency is 46.2%. (b): Output spectrum at the maximum output power with a resolution bandwidth of 0.01 nm. The  $\text{Yb}^{3+}$ -band ASE was below the sensitivity of the optical spectrum analyzer and the  $\text{Er}^{3+}$ -band ASE suppression was more than 58 dB.

spectrum normalized to its highest value is depicted in Fig. 5.3(b). It shows the bands between 1.0  $\mu\text{m}$  and 1.1  $\mu\text{m}$  and between 1540 nm and 1580 nm at the maximum output power. The  $\text{Er}^{3+}$ -ASE suppression was more than 58 dB and the  $\text{Yb}^{3+}$ -band ASE was below the sensitivity level of the spectrum analyzer. As it was explained beforehand, the  $\text{Yb}^{3+}$ -band ASE is the most common limitation in the power scaling of  $\text{Er}^{3+}:\text{Yb}^{3+}$ -codoped fiber amplifiers. Thus, the absence of  $\text{Yb}^{3+}$ -band ASE, together with the linearity of the optical slope, indicates feasibility of further power scaling.

### 5.2.2 Power and PER Stability

The fluctuations of the output power and the polarization extinction ratio (PER) at the maximum output power are shown in Fig. 5.4. The measurements were performed after 1 hour warm-up time such that the amplifier was in thermal equilibrium. The power levels were sampled once per second during 60 minutes using the thermopile detectors F150A-SH-V1 (*Ophir Optronics*) to measure the output power and two 3A-FS (*Ophir Optronics*) to measure the  $p$ - and  $s$ -polarization components to calculate the PER. The



polarization components were previously separated by a polarizing beam splitter (PBS) preceded by a quarter-wave plate and a half-wave plate to align the input polarization. The power fluctuations were approximately  $\pm 0.2\%$ , which is in the scale of the resolution of the utilized thermopile. The PER was approximately 12.5 dB at the beginning of the measurement time and slowly increased during the first 35 minutes up to around 13 dB for the second half of the measurement. A plausible cause of the remaining PER fluctuations

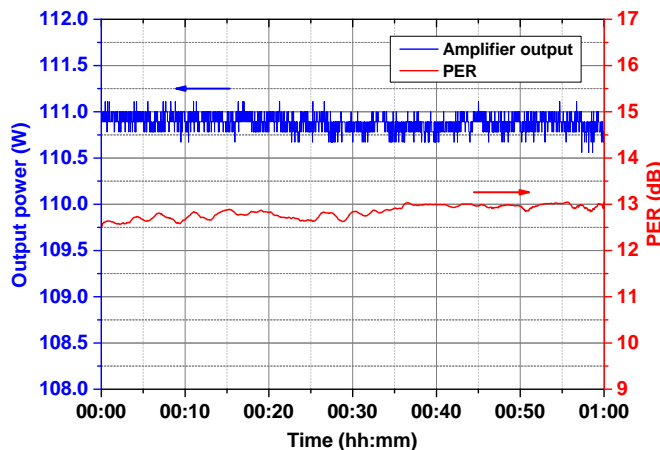


**Figure 5.4:** 1-hour measurement of the maximum output power (blue, left axis) and PER (red, right axis).

are thermal fluctuations in the fiber [Nod86; Zha93] since the active fiber was passively cooled by the aluminum spool but not temperature-stabilized. It is worth to point out that none of the fibers in the setup (neither the single-mode fiber, the active fiber nor the passive matching fiber) were polarization-maintaining (PM) fibers. Therefore, high PER values temporally stable should not be expected. Given this circumstance, the measured maximum PER of 13 dB and the fluctuations of  $\pm 0.3$  dB over 1 hour is a fairly good result. The average PER value was 12.8 dB, which leads to a linearly polarized output power of  $\sim 105$  W at 1556 nm. As this thesis is being written, an engineering prototype of the amplifier is being developed in the Laser Development Department at LZH in collaboration with the Albert Einstein Institute (AEI). This prototype includes, among other important improvements, a full PM design, a more carefully designed thermal management and up to 4 pump ports for further power scaling.

### 5.2.3 Modal Content Analysis

As it was explained back in Chapter 2, a suitable laser source for GWDs should provide an excellent output beam quality. In a fiber-based system this characteristic can be assumed per se when purely single-mode fibers are used, i.e., when the V-number is lower than 2.405. However, in amplifiers based on LMA fibers it may not be always the case. Even if a single-mode beam is coupled to an LMA fiber, an energy transfer from the fundamental mode to HOMs can eventually happen due to microscopic defects in the fiber, ASE, or environmental perturbations. Thus, the beam quality of the output signal of the fiber amplifier under study in this chapter has been characterized. A standard parameter widely

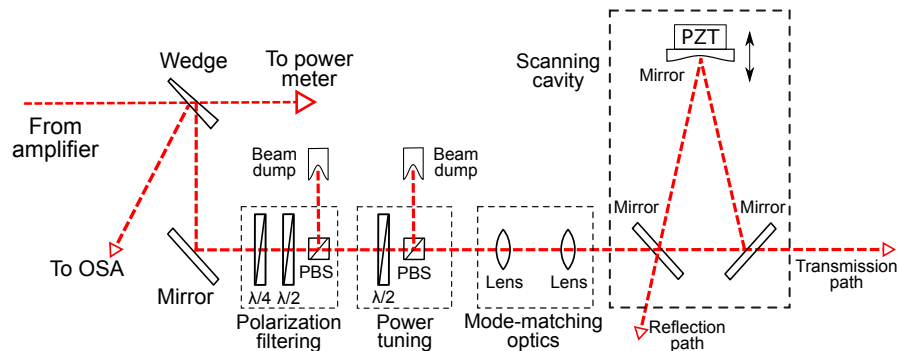


**Figure 5.5:** Experimental setup to measure the modal content.

used to quantify the quality of a Gaussian beam is the  $M^2$  value. This parameter is very popular in industrial applications as it provides a good indication of how much a beam can be focused. Nevertheless, it has been demonstrated that even a low value  $M^2$  of 1.1, which indicates a highly focusable beam, does not guarantee single transversal mode [Wie07]. Besides this, the actual power in the  $TEM_{00}$  mode cannot be determined by means of the  $M^2$ . Therefore, a different method must be used to characterize the beam quality in terms of transversal modes. In Fig. 5.5 the setup used to measure the modal content is depicted. This diagnostics instrument has been developed by the Albert Einstein Institute in Hannover [Kwe07]. It consists of a non-cofocal 3-mirror cavity used to decompose the beam into a set of TEM modes. One of the mirrors is attached to a piezoelectric transducer to change the cavity length by actuating on the piezo signal. A ramp signal fed to the piezo allows to scan the cavity. By doing this, the different TEM modes in the beam are transmitted through the cavity depending on the position of the scanning mirror. A photodiode in the transmission path measures the power of the transmitted modes. The instrument requires low input power ( $< 100$  mW) and a linearly-polarized beam. For this reason, two free-space beam-conditioning stages were setup before the cavity: (i) A polarization filtering stage consisting of a quarter-wave plate, a half-wave plate and a PBS, and (ii) a power control stage made of a half-wave plate and a PBS. To optimize the mode matching to the cavity, a set of two lenses was installed in front of it. The finesse of the cavity was  $\sim 250$  for  $p$ -polarization and the free spectral range (FSR) was  $\sim 714$  MHz. The measurement process is automated and controlled via software by a computer. An average of 100 measured traces is used to fit theoretical functions of the fundamental mode and HOMs to estimate the relative  $TEM_{00}$  mode content [Kwe07].

The details of the modescan at the maximum output power are shown in Fig. 5.6. The vertical axis shows the normalized optical intensity in a logarithmic scale and the horizontal axis represents the normalized frequency. The graph shows the measured relative intensities of the TEM modes, the fit to the data and the theoretical fundamental mode intensity. The  $TEM_{00}$  mode content of the beam at an output power of 111 W was calculated to be  $\sim 94.8\%$ . Taking the PER of 13 dB presented in Section 5.2.2, the total power in a linearly-polarized  $TEM_{00}$  mode at 1556 nm is  $\sim 100$  W. This result represents an improvement

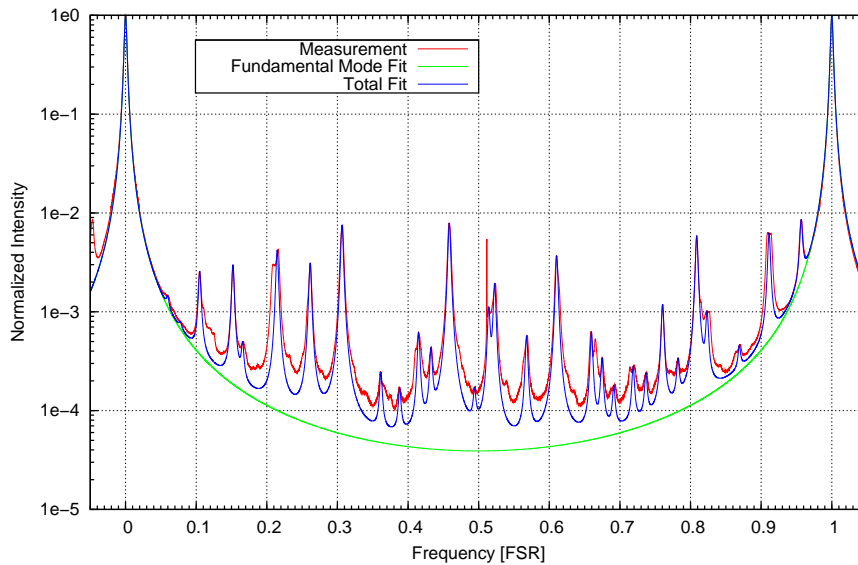


**Figure 5.6:** Modescan at the maximum output power level. The vertical axis is the normalized optical intensity and the horizontal axis is the normalized frequency. Red: 100-times averaged measurement. Blue: fit of a set of TEM modes. Green: Fit of the theoretical TEM<sub>00</sub> mode.

of almost a factor of 2 compared to the highest power records previously reported in single-frequency and single-mode Er<sup>3+</sup>:Yb<sup>3+</sup>-codoped fiber amplifiers at 1.5  $\mu\text{m}$  [Kuh11; Ste14a]. The evolution of the fundamental mode content versus the output power is shown in Fig. 5.7. It can be seen that, in general, there is a small beam quality degradation as the output power increases. The highest TEM<sub>00</sub> mode content was 98.7%, measured at an amplifier output power of 24 W, whereas the lowest value of 93.9% was measured at an output power of 84.5 W.

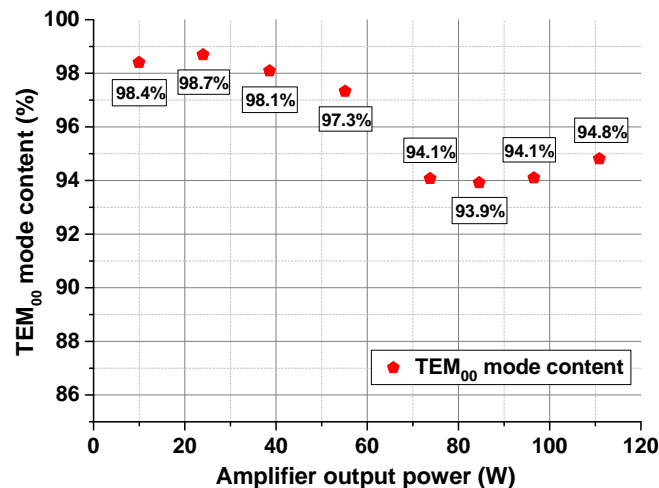


**Figure 5.7:** Evolution of the TEM<sub>00</sub> mode content with the amplifier output power.

### 5.2.4 Relative Power Noise

The RPN of the free-running laser source in a GWD determines important characteristics of the control loop to stabilize it. In fiber-based systems this control loop can either actuate on the seed source or on the pump diodes' current as commented in Chapter 4. In any case, it is important to characterize the excess noise introduced by the amplifier on top of it. The experimental arrangement used to measure the RPN is shown in Fig. 5.8. Again, a polarization filtering and a power tuning stage were installed for signal conditioning. A set of optical density (OD) filters was also used to further attenuate the beam intensity without setting the power tuning stage too close to its minimum transmission point. The signal

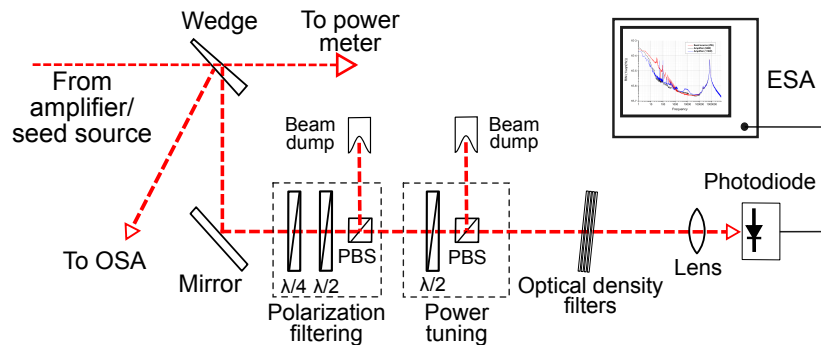


**Figure 5.8:** Experimental setup employed to measure the relative power noise.  $\lambda/4$ : quarter-wave plate,  $\lambda/2$ : half-wave plate, PBS: polarizing beam splitter, OSA: optical spectrum analyzer, ESA: electrical spectrum analyzer.

was detected using an InGaAs photodiode (PDA10CF, *Thorlabs*) with 150 MHz bandwidth and its electrical signal was measured by two different signal analyzers depending on the frequency range: the frequency band from 1 Hz to 100 kHz was recorded by a SR785 (*Stanford Research Systems*) whereas the band from 100 kHz to 6 MHz was covered with an E4440A (*Agilent*). In Fig. 5.9 the RPN at high power (110 W) and at a medium power (55 W) is presented. The RPN of the seed source at 2 W is included in the graph for comparative purposes. It can be seen that the RPN of the amplified signal is lower than the seed RPN at frequencies below 1 kHz. This noise damping is due to the effective high-pass behavior of the seed-to-output transfer function caused by the amplification mechanism [Ste15]. The plot shows a feature at around 10 kHz observed only in the RPN of the high power level. A hypothesis to explain this bump is the effect of cross-coupling light between the pump ports of the pump combiner, producing pump power noise that ultimately couples to the signal in the amplifier. It is important to mention that the measurement of the RPN at 55 W was done with the amplifier pumped only by one diode, and the noise feature at 10 kHz appeared only when both pump diodes were being used at the same time. This strengthens the aforementioned hypothesis. At frequencies above 100 kHz the three RPN curves coincide.

According to these results, it can be stated that the high power amplifier does not add significant excess power noise to the seed signal, and can even partially filter it at low frequencies. The behavior of the RPN when the *off-peak* pumped amplifier is seeded with a

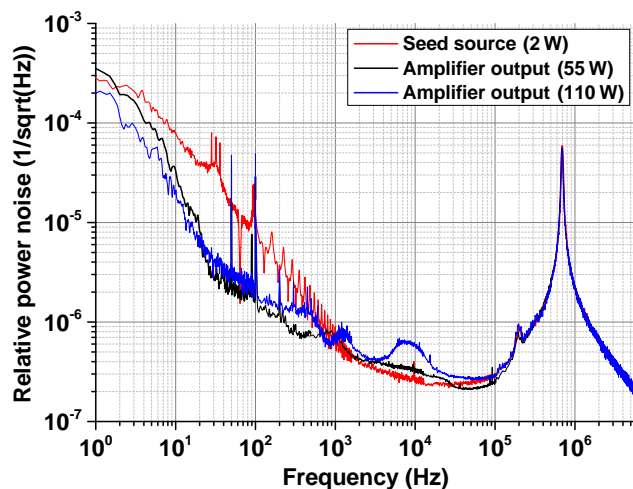


**Figure 5.9:** Relative power noise of the seed source at 2 W (red) and the amplifier at 55 W (black) and at 110 W (blue).

stabilized signal remains uninvestigated and shall be object of study using the engineering prototype being developed to determine whether it has any relevant effect on the RPN of the amplified signal.

### 5.2.5 Frequency Noise

The frequency noise of the amplified signal was also measured at medium (55 W) and high (110 W) power and compared with the seed FN. The measurement setup was described in Section 5.2.3 and shown in Fig 5.5 (see [Kwe07] for further details) with the following procedure: the 3-mirror cavity was locked to the fundamental mode and the signal driven to the piezo required to compensate the frequency fluctuations was recorded for 300 seconds. Then, this time series was used by the diagnostics software to compute the frequency noise, which is shown in Fig. 5.10(a). Apart from small differences, the FN of the amplifier at both power levels, 55 W and 110 W, match the FN of the seed source. This demonstrates that the amplifier does not have any relevant impact on the FN of the signal, which is consequently mainly determined by the seed source.

A common parameter provided by the manufacturers to characterize the frequency noise is the linewidth (also called frequency bandwidth) defined for a given time lapse or frequency. The linewidth can be calculated from the measured frequency noise spectrum as

$$BW(f_0) = \left[ \int_{f_0}^{\infty} [\mathcal{S}(Hz/\sqrt{Hz})]^2 df \right]^{1/2}, \quad (5.4)$$

where  $f_0$  is the inverse of the time at which the linewidth is specified and  $\mathcal{S}$  is the measured frequency noise spectrum. The linewidth curves calculated for the seed source and the amplifier output at 55 W and 110 W are plotted in Fig. 5.10(b) from 1 Hz to 100 kHz (that is, from 10  $\mu$ s to 1 s). Note that due to the absence of data at higher frequencies, the dip around 100 kHz may not be representative. The seed linewidth specified by the

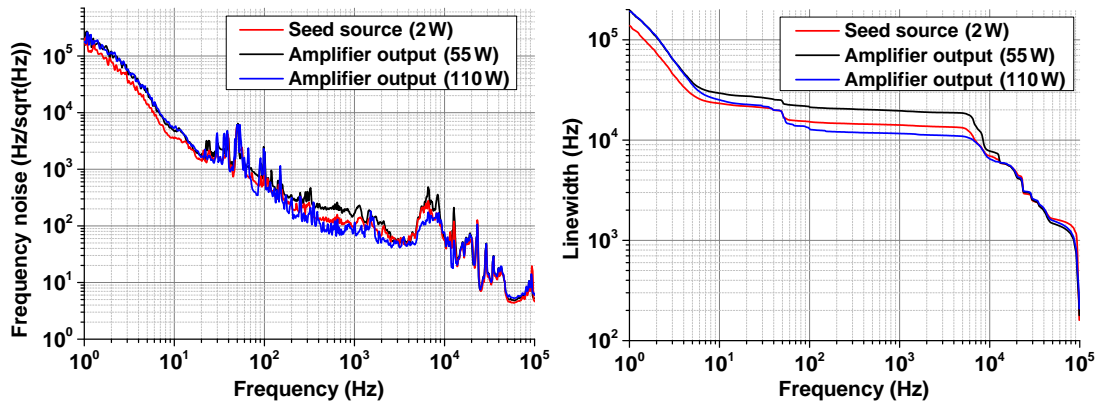


**Figure 5.10:** (a): Frequency noise and (b): calculated linewidth of the seed source at 2 W (red), amplifier at 55 W (black) and at 110 W (blue).

manufacturer is  $< 10$  kHz based on a self-heterodyne measurement with 120  $\mu$ s delay time, and the measured linewidth was  $\sim 8.1$  kHz, for 120  $\mu$ s, in agreement with the specifications.

### 5.2.6 Stimulated Brillouin Scattering

The importance of preventing the onset of SBS in the amplifier was described in Chapter 3. It has been demonstrated that when SBS is triggered, a broadband power noise is imprinted on the amplified signal [Hor97]. In a fiber amplifier this effect can be exploited to detect the onset and build-up of SBS by monitoring the relative power noise looking for a power-dependent noise increase [Hil08]. Fig. 5.11 shows the RPN at different output power levels of the  $\text{Er}^{3+}:\text{Yb}^{3+}$ -codoped fiber amplifier. Using the aforementioned method, the highest

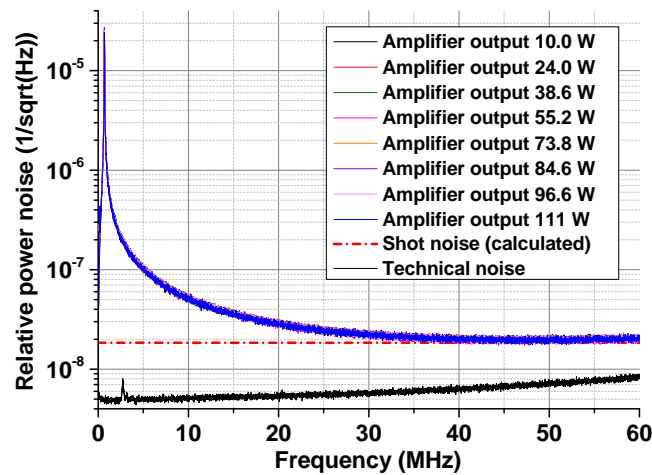


**Figure 5.11:** Relative power noise up to 60 MHz at different output power levels of the  $\text{Er}^{3+}:\text{Yb}^{3+}$ -codoped fiber amplifier. Additionally, the calculated shot noise level (dashed red) and the technical noise (black) are plotted.

sensitivity to the SBS-induced noise is achieved by monitoring the frequency range where the RPN is shot noise limited. In the case at hand the RPN decreases from the relaxation oscillation frequency up to approximately 40 MHz. Thus, the RPNs were recorded up to 60 MHz. The calculated shot noise level as well as the contribution of the technical noise are also plotted in Fig. 5.11. The technical noise was measured by covering the photodiode and includes the dark photocurrent and the instrumentation noise. The RPN measurements were performed with a relatively high signal level at the photodiode in order to minimize the shot noise level, leaving a margin to prevent its saturation (i.e., the electrical signal from the photodiode was  $\sim 9$  V and the saturation voltage was 10 V). The graph shows that all the RPN curves overlap at the shot noise level without any noticeable power-dependent excess noise feature. This proves that the system is most likely SBS-free. This statement is not strictly true since the sensitivity is limited by the shot noise in the photodetector, and it may be that the SBS-induced noise is below this limit. Increasing the sensitivity of the measurement would require a detector capable to manage more power, e.g., a multiphotodiode-based technique [Kwe09]. In any case, the results demonstrate promising power scaling capabilities. It is worth to point out that no SBS-mitigation techniques were implemented (for example temperature gradients [Han01] or strain forces along the fiber [Yos93]). Thus, it can be assumed that there is a great room for SBS-free power scaling. This will be one of the key characteristics to investigate with the engineering prototype currently being developed at LZH.

### 5.3 Conclusion

In this chapter a single-frequency and high-power *off-peak* pumped  $\text{Er}^{3+}:\text{Yb}^{3+}$ -codoped fiber amplifier at 1556 nm has been studied by means of numerical simulations and laboratory experiments. The simulation results suggest that pumping an  $\text{Er}^{3+}:\text{Yb}^{3+}$ -codoped fiber at 940 nm enables higher output power levels compared to pumping at 976 nm and 915 nm. This is due to a better  $\text{Yb}^{3+}$ -to- $\text{Er}^{3+}$  energy transfer efficiency at high pump power levels, which leads to a higher threshold of the  $\text{Yb}^{3+}$ -band ASE. The *off-peak* pumping technique was experimentally tested in a monolithic fiber amplifier and up to 111 W at 1556 nm were obtained, only limited by the available pump power. The system was thoroughly characterized with respect to its application in GWDs. It exhibited good linearity along the entire slope, with a remarkable efficiency of more than 46 %. At the same time, the optical spectrum showed no signs of  $\text{Yb}^{3+}$ -band ASE and an  $\text{Er}^{3+}$ -ASE suppression of more than 58 dB. The power fluctuations were  $\pm 0.2$  % over 1 hour and the polarization extinction ratio was 12.8 dB  $\pm$  0.2 dB. Concerning the beam quality, the amplified signal presented a small (and expected) deterioration of the relative fundamental mode content from 98.7 % at 24 W to 93.9 % at 84.5 W. Nonetheless, at the maximum output power level the amount of power in the  $\text{TEM}_{00}$  mode was 94.8 %. Thus, the maximum (pump-limited) linearly-polarized  $\text{TEM}_{00}$  mode power was  $\sim 100$  W. In terms of relative power noise, the amplifier demonstrated to have a noise-damping effect below 1 kHz. A noise feature present at around 10 kHz might be due to pump noise coupling to the signal, possibly generated due to a cross-coupling effect between the pump ports of the pump combiner. The relative power noise at high frequencies up to 60 MHz was recorded for different power levels without the appearance of power-dependent excess noise features, which demonstrates that

the amplifier is free of SBS. The amplifying process had no impact on the frequency noise of the free-running seed signal.

The results summarized above show the benefits of the *off-peak* pumping technique for high power applications. Not only the achievable maximum power was higher compared to systems with similar characteristics pumped at 976 nm, but also a higher optical efficiency was obtained despite the larger quantum defect. Although the *off-peak* pumping has been proposed as a solution for high power amplifiers, it can be a good alternative also for low power amplifiers and preamplifier stages. Such systems usually deal with very low seed input levels, which exacerbates the Yb<sup>3+</sup>-band ASE issue. In these cases it would be very beneficial to distribute the pump light more homogeneously along the active fiber by pumping at a wavelength where the absorption is lower.

In the experiment presented, no ultimate limiting factor for further power scaling was observed. Although this is promising, the trade-off imposed by the inherent lower absorption is the required longer fiber. Hence, one can speculate that SBS will be the limiting factor as its power threshold decreases with fiber length (see Chapter 2). As it has been discussed in this chapter, the excellent performance of the system motivated the design of a more sophisticated version of it. This engineering prototype will allow to study in more detail its potential use as high power laser source for next-generation GWDs.



## CHAPTER 6

---

### Er<sup>3+</sup>:Yb<sup>3+</sup>-Codoped and Er<sup>3+</sup>-Doped Fiber Amplifiers Core-Pumped at 1018 nm

---

The use of LMA fibers in fiber amplifiers becomes necessary when high output power levels are required. However, LMA fibers have a number of disadvantages that make the use of single-mode fibers preferable if they can reach the required power levels (for example watts-scale). On one hand, LMA fibers are in many cases difficult to splice and cleave and the commercial availability of LMA-based components is relatively poor. These two drawbacks hinder the realization and maintenance of monolithic systems based on LMA fibers. Besides this, the large core of LMA fibers can make the amplifier prone to develop HOMs and modal instabilities (MI) [Jau12; War12], making necessary the implementation of any HOM suppression strategy [Jau13]. In addition, a large core requires higher seed power to saturate the amplifier. This issue is especially relevant when the available seed power level is low. On the other hand, single-mode fibers can be easily and reliably integrated in all-fiber systems via standard processes, there is a wide commercial availability of compatible components and SM fibers are immune to HOMs. The drawback is the inability to obtain high power levels in relatively short lengths due to the low pump light absorption, particularly in cladding pumped systems.

A common strategy to increase the pump light absorption and to reduce the fiber length is to couple the pump light in the core of the active fiber rather than in the cladding. By doing this, the overlap between the pump light and the doped core is maximized, and the pump light intensity and therefore the population inversion becomes higher. Nevertheless, in order to couple the pump light in the core of the fiber, the pump diode must provide sufficiently good beam quality. Unfortunately, the output power of such pump diodes is limited to around 1 W. This constitutes a major limitation for diode-based core-pumped SM fiber amplifiers. To circumvent this obstacle, a variety of core-pumping schemes using fiber-based pump sources have been proposed [Zho17]. Although setting up fiber lasers at 9xx nm has turned out to be complex and inefficient [Liu13; Wan13], a variety of pump wavelengths can be used to pump Er<sup>3+</sup> and Yb<sup>3+</sup> [Zho17]. In [Sup13], a cascaded Raman fiber laser and amplifier at 1480 nm was demonstrated with an output power of 301 W. Such systems have a great potential as pump sources to core-pump Er<sup>3+</sup>-doped fiber amplifiers. The tradeoff was a quite complex and cost-inefficient system architecture, requiring a high power Yb<sup>3+</sup>-doped fiber laser at 1117 nm to pump a Raman amplifier seeded by a multiwavelength source made of another Yb<sup>3+</sup>-doped fiber laser and a Raman resonator. The final system required several tens of meters of fiber, up to 14 fiber Bragg gratings and around 500 W of pump power at 975 nm without including the main amplifier

at 1.5  $\mu\text{m}$ . In [Jeb14], 264 W at 1585 nm was obtained by in-band pumping a 18 m-long  $\text{Er}^{3+}:\text{Yb}^{3+}$ -codoped fiber at 1535 nm. Despite of this astonishing result, the system was highly customized and complex. A specially designed  $\text{Er}^{3+}:\text{Yb}^{3+}$ -codoped fiber was used and up to 36 fiber lasers at 1535 nm were combined to pump the main laser. Furthermore, the output did not have narrow linewidth. In [Fuj15], a single-frequency amplifier at 1539 nm was demonstrated by core-pumping an  $\text{Er}^{3+}$ -doped fiber amplifier at 1480 nm. A high output power of 11.6 W was achieved using a 3.5 m-long active fiber. Nonetheless, the pump source consisted again of a cascaded Raman laser pumped by an  $\text{Yb}^{3+}$ -doped fiber laser at 1117 nm. The high power core-pumping concept has also been successfully demonstrated in single-frequency fiber amplifiers at 1  $\mu\text{m}$ . In [The16], an  $\text{Yb}^{3+}$ -doped laser at 1018 nm was used to pump a single-frequency  $\text{Yb}^{3+}$ -doped fiber amplifier at 1064 nm, achieving up to 158 W with only 1.25 m of  $\text{Yb}^{3+}$ -doped fiber.

In this chapter, a SM  $\text{Er}^{3+}:\text{Yb}^{3+}$ -codoped fiber amplifier is for the first time core-pumped at 1018 nm instead of at any high absorption peak wavelength (i.e., 976 nm, 1480 nm and 1530 nm). The experimental setup did not require Raman lasers and was built using only standard single-mode fibers and components. The resulting architecture is an *off-peak* pump concept where the pump wavelength is longer than that of the maximum absorption at 976 nm rather than lower like in the system demonstrated in Chapter 5. This showed to have a positive impact regarding the suppression of the  $\text{Yb}^{3+}$ -band ASE and permitted an output power of more than 11 W at 1556 nm. The concept was tested with different commercially available SM  $\text{Er}^{3+}:\text{Yb}^{3+}$ -codoped fibers and the results are compared in terms of maximum output power, efficiency and power stability. Besides the experimental demonstration of the concept, a photodarkening-like effect was observed for the first time in an  $\text{Er}^{3+}:\text{Yb}^{3+}$ -codoped fiber amplifier at 1.5  $\mu\text{m}$ . Likewise an  $\text{Er}^{3+}$ -doped  $\text{Yb}^{3+}$ -free fiber amplifier core-pumped at 1018 nm is demonstrated and its performance discussed.

The results presented in this chapter have been partially published in [Var18a; Var18b].

## 6.1 Experimental Setup

The experimental setup is depicted in Fig. 6.1. The pump source at 1018 nm was an  $\text{Yb}^{3+}$ -doped fiber oscillator made of a 2.5 m-long piece of single-mode  $\text{Yb}^{3+}$ -doped fiber LMA-YDF-10/130-M (*Nufern*) which was cladding pumped at 976 nm. Two fiber Bragg gratings at 1018 nm formed the cavity: One with 99.9% reflectivity and 1.8 nm full width half maximum (FWHM) bandwidth and an output coupler (OC) with 20.2% reflectivity and 0.7 nm FWHM bandwidth. A cladding light stripper (CLS) was spliced after the oscillator to remove any residual light at 976 nm. The pump light at 1018 nm was filtered by a cascade of wavelength division multiplexers (WDMs) prior to the main amplifier in order to suppress any potential  $\text{Yb}^{3+}$ -band ASE from the oscillator. The importance of this filtering stage lies in the fact that any spectral component between  $\sim 1020$  nm and 1100 nm would experience gain in the  $\text{Er}^{3+}:\text{Yb}^{3+}$ -codoped fiber amplifier, spoiling its performance at 1.5  $\mu\text{m}$ . The filtering stage consisted of a network of three consecutive WDMs each with a transmission wavelength at 1018 nm and rejection bands centered at 1030 nm, 1040 nm and 1050 nm with 12 nm, 11 nm and 16 nm FWHM bandwidth. Behind the WDM network, the maximum power at 1018 nm was  $\sim 25$  W. A commercial fiber laser (Rock, *NP Photonics*) at 1556 nm with kHz-scale linewidth was used to seed the amplifier. This seed module

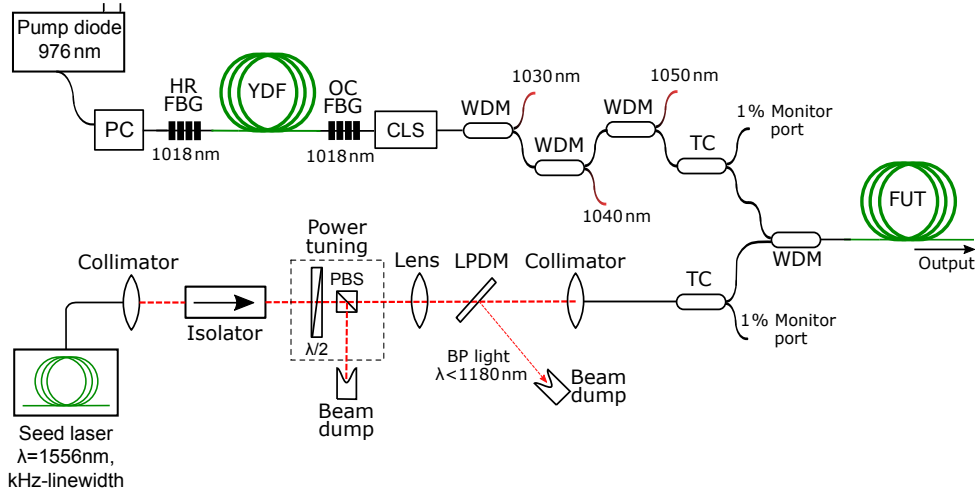


**Figure 6.1:** Experimental setup of the fiber amplifier core-pumped at 1018 nm. PC: pump combiner, HR FBG: high reflection fiber Bragg grating, YDF:  $\text{Yb}^{3+}$ -doped fiber, OC FBG: output coupler fiber Bragg grating, CLS: cladding light stripper, WDM: wavelength division multiplexer, TC: tap coupler,  $\lambda/2$ : half-wave plate, PBS: polarization beam splitter, BP: backpropagating, FUT: fiber under test.

was the same described in Chapter 5 and, similarly, it was free-space coupled to the fiber to keep its output port intact for future use. However, a simple SM-fiber-to-SM-fiber splice would be sufficient to build the entire setup, including seed and pump sources, in a truly all-fiber configuration. For power control and protection purposes, the free-space incoupling stage included an isolator at 1.5  $\mu\text{m}$ , a power tuning stage and a long pass dichroic mirror (LPDM) with cutoff wavelength at 1180 nm. Both, pump and seed signal ports, included a 1% tap coupler to monitor the power available in the amplifier. Finally, a WDM was used to combine the seed and pump signals in the core of the single-mode fiber to which the active fibers under test were spliced. The details of the different  $\text{Er}^{3+}:\text{Yb}^{3+}$ -codoped fibers tested in this setup are summarized in Table 6.1. Although both, pump and seed signals were coupled to the core of the active fibers, the samples DCF-EY-6/125,

**Table 6.1:** Fibers under test in the  $\text{Er}^{3+}:\text{Yb}^{3+}$ -codoped fiber amplifier core-pumped at 1018 nm.  $d_c$ : core diameter, NA: numerical aperture, MFD: mode field diameter,  $\lambda_c$ : cutoff wavelength.

Fiber	$d_c$	NA	MFD <sup>(*)</sup>	$\lambda_c$
<i>CorActive</i> DCF-EY-6/128	5.6 $\mu\text{m}$ <sup>(b)</sup>	0.20 <sup>(a)</sup>	6.43 $\mu\text{m}$ <sup>(b)</sup>	1.46 $\mu\text{m}$ <sup>(b)</sup>
<i>Nufern</i> EY-SMF-6/125-HE	6.0 $\mu\text{m}$ <sup>(a)</sup>	0.18 <sup>(a)</sup>	7.08 $\mu\text{m}$ <sup>(b)</sup>	1.41 $\mu\text{m}$ <sup>(b)</sup>
<i>FiberCore</i> TC1500Y	9.0 $\mu\text{m}$ <sup>(b)</sup>	0.12 <sup>(a)</sup>	10.61 $\mu\text{m}$ <sup>(b)</sup>	1.41 $\mu\text{m}$ <sup>(c)</sup>
<i>CorActive</i> EY-110	5.6 $\mu\text{m}$ <sup>(b)</sup>	0.17 <sup>(c)</sup>	7.84 $\mu\text{m}$ <sup>(c)</sup>	1.15 $\mu\text{m}$ <sup>(b)</sup>

<sup>(\*)</sup> At 1556 nm with Marcuse formula [Mar77];

<sup>(b)</sup> Calculated;

<sup>(a)</sup> Designed;

<sup>(c)</sup> Measured.

EY-SMF-6/125-HE and TC1500Y had low refractive index coatings, i.e., these fibers can guide light in the cladding. Some light reaching the cladding (and thus being guided in it) is unavoidable in the splice. Thus, to prevent guiding any light in the cladding, around 5 cm of coating was removed immediately after the splice and substituted by high refractive index gel. The fibers were spooled on an aluminum mandrel temperature stabilized to 18 °C.

## 6.2 Mid-Power Fiber Amplifier

The amplifiers were seeded with a relatively high power of 621 mW to ensure saturation condition. The fiber length was 250 cm in all cases. The losses in the splice of the active fiber to the passive fiber of the WDM due to the mode field mismatch were calculated in each case to accordingly apply the proper correction factors. Fig. 6.2(a) shows the output power at 1.5  $\mu\text{m}$  and the residual light in the 1  $\mu\text{m}$ -band versus the pump power available in the active fiber. Here, the residual light refers to any spectral component at a wavelength lower than 1180 nm, i.e., given by the cutoff wavelength of the dichroic mirror used to separate the spectral components, which includes the unabsorbed pump light at 1018 nm and the Yb<sup>3+</sup>-band ASE. The highest output power was 11.2 W, obtained with the sample TC1500Y. This was the only fiber that exhibited a linear slope up to the highest measured output power as well as the only one limited by the available pump power. The optical-to-optical efficiency was 45.6%, which is relatively close to the quantum limit of 65.4%. The samples SM-EYDF-6/125-HE, EY-110 and, to a lower extent, the

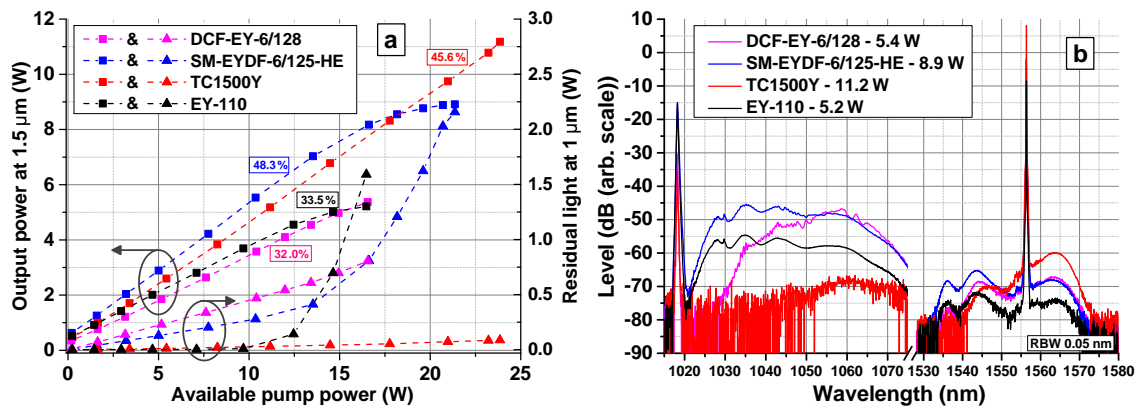


**Figure 6.2:** (a): Output power and residual light vs. pump power available in the fiber under test. The squares represent the output power at 1556 nm and the triangles the residual light at  $\lambda < 1180$  nm (unabsorbed pump light and Yb<sup>3+</sup>-band ASE). The calculated optical efficiency is shown in the same color of the curve it refers to. (b): Optical spectra at the maximum output power for each amplifier. The resolution bandwidth is 0.05 nm

DCF-EY-6/125 presented a roll-off of the output power and a steep increase of the residual light at 1  $\mu\text{m}$ . This effect occurs when the Er<sup>3+</sup> population inversion becomes saturated and the energy cannot be transferred from Yb<sup>3+</sup> ions to Er<sup>3+</sup> ions as fast as it is absorbed by Yb<sup>3+</sup>. Consequently, the extractable power at 1.5  $\mu\text{m}$  is limited and the emission in the Yb<sup>3+</sup>-band ASE increases rapidly. The optical spectrum at the maximum output

power for each of the tested fibers is shown in Fig. 6.2(b). The sample TC1500Y had a very small  $\text{Yb}^{3+}$ -band ASE component, while it was rather high for the other three samples, in concordance with the observations of the optical slopes. The high ASE level with the samples SM-EYDF-6/125-HE, EY-110 and DCF-EY-6/125 was the reason to stop increasing the pump power during the experiment in order to avoid parasitic lasing or pulsing that could compromise the integrity of the system. In [Nuf15], the performance of the fiber SM-EYDF-6/125-XP, very similar to the SM-EYDF-6/125-HE here under test, is analyzed by the manufacturer in an amplifier at  $1.55 \mu\text{m}$  cladding-pumped at  $940 \text{ nm}$ . The reported optical efficiency in that case was  $34\%$  whereas the achieved efficiency of the amplifier made of the fiber SM-EYDF-6/125-HE core-pumped at  $1018 \text{ nm}$  was more than  $48\%$ . Comparatively, this is an enhancement of more than  $40\%$ . It is worth to point out that, according to the manufacturer, the differences between the -XP and the -HE fibers are the designed pump absorption ( $1 \text{ dB/m}$  at  $915 \text{ nm}$  for the -XP and  $0.75 \text{ dB/m}$  for the -HE fiber) and the MFD ( $6.1 \mu\text{m}$  for the -XP and  $6.8 \mu\text{m}$  in the case of the -HE version).

The output power levels were recorded for time periods from 1 to 4 hours. The time traces are shown in Fig. 6.3(a). A sharp deterioration of the output power can be observed with the fiber SM-EYDF-6/126-HE, with up to  $36\%$  power drop after 2 h. A similar effect occurred for the sample DCF-EY-6/128, with a power loss of  $13\%$  after 1 hour. The amplifiers made with the fibers EY-110 and TC1500Y present a fast initial power drop during approximately 15 and 30 minutes that could be identified as a pump power drop until the pump source reached thermal equilibrium. After 2 hours, the power deterioration was  $7\%$  with the fiber EY-110 whereas the TC1500Y maintained the output power constant at  $11 \text{ W}$  until the end of the measurement. Although the exact mechanism causing this

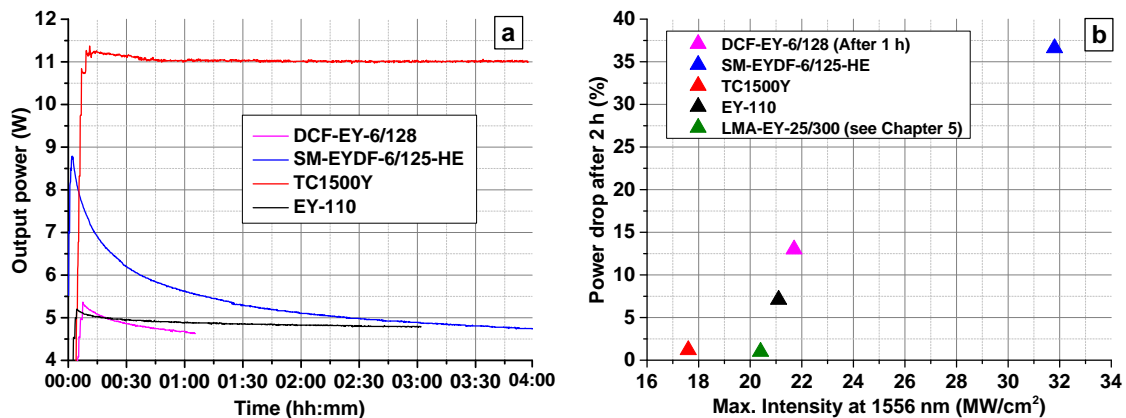


**Figure 6.3:** (a): Evolution of the output power versus time for the fiber amplifiers made of the four different fibers under test. (b): Power drop versus light intensity at  $1556 \text{ nm}$  in the core of the fiber under test. The intensity in the LMA fiber of the experiment presented in Chapter 5 is included.

power degradation could not be identified, it was found to be more pronounced the higher the light intensity at  $1556 \text{ nm}$  in the core of the fiber was. The power drop after 2 hours relative to the maximum output power versus the intensity in the core of each fiber is depicted in Fig. 6.3(b) (after 1 hour in the case of the DCF-EY-6/128). The data of the

fiber amplifier presented in Chapter 5 has also been included even though the system architecture, pump wavelength and fiber type were different. A threshold-like behavior in the power degradation can be seen at the core intensity of  $\sim 21 \text{ MW}/\text{cm}^2$ . Despite of the higher output power, the fibers LMA-EY-25/300 (from Chapter 5) and TC1500Y did not experience a significant power degradation due to their relatively large cores. A plausible explanation for this observation is the photodarkening effect (PD) [Kop07]. PD is the gradual increase of transmission loss when a medium (in this case the fiber core) is irradiated with high intensity at certain optical wavelengths or ionizing radiation. Although the physical mechanism behind PD is complex and still not fully understood, it is attributed to the formation of color centers, i.e., defects in the glass matrix of the fiber [Don95]. It strongly depends on the composition of the fiber [Jet08] and it has been observed that the population inversion also plays an important role in the PD rate and magnitude in  $\text{Yb}^{3+}$ -doped fibers [Kop08; Li14]. In  $\text{Er}^{3+}:\text{Yb}^{3+}$ -codoped fiber amplifiers, PD has not been observed until very recently [Rob18]. Although the origin and mitigation of PD are object of active research work, a detailed investigation is out of the scope of this thesis.

In the measurements shown before the fiber length was 250 cm independently on the fiber under test. This was (most likely) not the optimal length. In Fig. 6.2(a) the amplifier with the sample TC1500Y showed a very low residual light of approximately 87.5 mW at the maximum pump power of 23.7 W. Neglecting the  $\text{Yb}^{3+}$ -band ASE this represents less than 0.4% of unabsorbed pump light. Besides this, the optical spectrum showed an

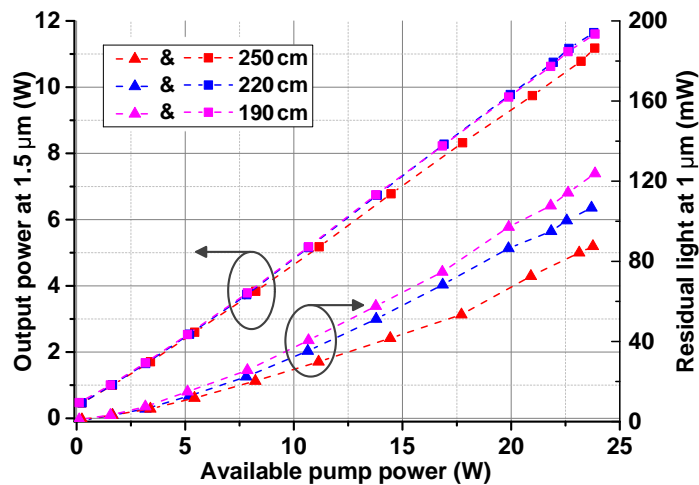


**Figure 6.4:** Output power and residual light vs. the pump power available in the fiber for different length of the sample TC1500Y. The squares represent the output power at 1556 nm and the triangles the residual light at  $\lambda < 1180 \text{ nm}$ , i.e., unabsorbed pump light and  $\text{Yb}^{3+}$ -band ASE.

incipient lobe in the  $\text{Er}^{3+}$ -band ASE at longer wavelengths, which is an indication of excess reabsorption at  $1.5 \mu\text{m}$ . These two features together suggest that the performance of the amplifier can be optimized with a shorter piece of fiber. The output power and residual light for different length of the fiber TC1500Y are shown in Fig. 6.4. As can be seen, the

efficiency (hence the maximum output power) slightly increased reducing the length of the fiber to 220 cm. In this case the maximum output power was 11.6 W (+3.5%), the optical efficiency 48.6%, and the residual light 106.7 mW (+15.7%). With a length of 190 cm the output power slope did not change significantly, nonetheless the residual light increased up to 123.8 mW. This shows the existing trade-off between fiber length and reabsorption: The higher the power is at 1556 nm, the higher the reabsorption of the amplified signal by  $\text{Er}^{3+}$  ions, which provokes the gain to drop.

### 6.3 Low-Power Fiber Amplifier

One of the major advantages of single-mode fibers compared to LMA fibers is their better performance when it comes to the amplification of low seed power levels because their smaller core, and therefore higher light intensity, enhances the excitation of the desired atomic transition at the seed wavelength. This makes SM fibers usually a better option for low power amplifiers or preamplifiers in multistage systems. In this context, the  $\text{Er}^{3+}:\text{Yb}^{3+}$ -codoped fiber amplifier core-pumped at 1018 nm was tested with only 5 mW of seed power, emulating the typical power levels of ultra-narrow linewidth diodes or fiber lasers. The active fiber used for this test was the TC1500Y given its good performance in the previous measurements and the length was 190 cm.

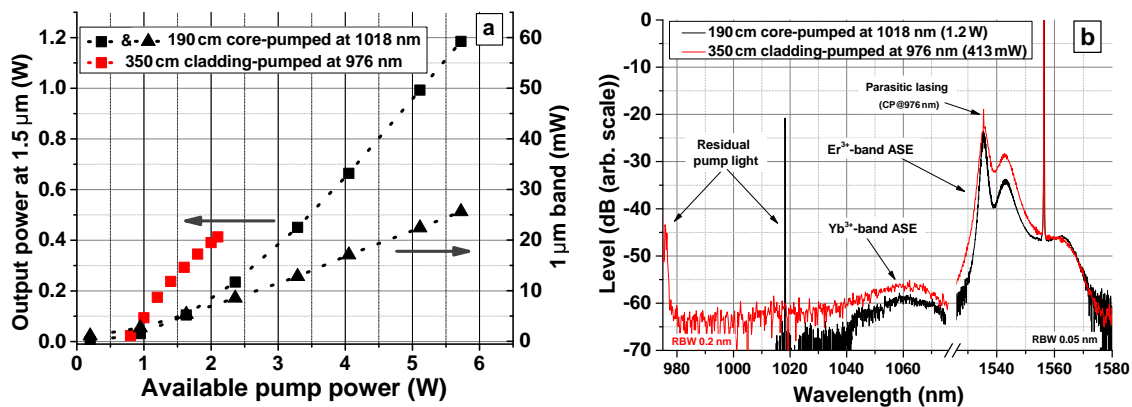
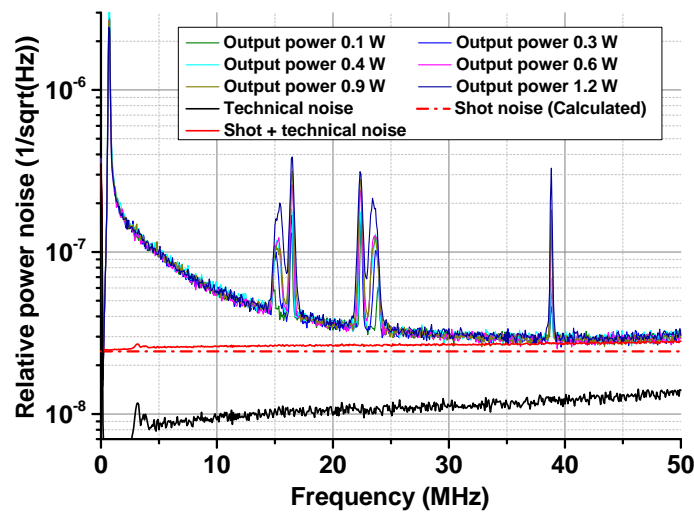


**Figure 6.5:** Comparison between the amplifier core-pumped at 1018 nm and an amplifier cladding-pumped at 976 nm. (a): Output power vs. available pump power. The residual light in the 1  $\mu\text{m}$ -band of the cladding-pumped system could not be measured since it was pumped in counter-propagation direction. (b): Optical spectrum of the 1  $\mu\text{m}$  and 1.5  $\mu\text{m}$  bands. The main spectral features are indicated. CP: cladding-pumped.

In Fig. 6.5 the slope and output spectrum are represented and compared with an  $\text{Er}^{3+}:\text{Yb}^{3+}$ -codoped fiber amplifier also seeded with 5 mW at 1556 nm but cladding-pumped at 976 nm in counter-propagation direction. To achieve sufficient pump power absorption the cladding-pumped amplifier consisted of 350 cm of the EY-EYDF-6/125-HE fiber. The optical-to-optical slopes are plotted in Fig. 6.5(a). The amplifier cladding-pumped at 976 nm had a lower threshold and slightly higher efficiency of 36% versus 30% in the case of the core-pumped system. However, the maximum output power of 1.2 W was significantly higher than the maximum output power of 413 mW achieved with the cladding-pumped

amplifier. In both cases further power scaling was limited by  $\text{Er}^{3+}$ -band ASE as can be seen in Fig. 6.5(b). The optical spectrum at the maximum output power shows that the cladding-pumped system developed parasitic lasing at around 1535 nm. The amplifier core-pumped at 1018 nm also exhibited a high, but without peaks, level of  $\text{Er}^{3+}$ -band ASE at the output power of 1.2 W, but no indications of parasitic lasing.

For the sake of completeness, signs of SBS were searched in the output signal of the core-pumped amplifier. The employed method was the one described in Section 5.2.6. An InGaAs photodiode (PDA10CF, *Thorlabs*) with 150 MHz bandwidth was used to detect the signal and the spectrum analyzer E4440A (*Agilent*) to record the noise spectrum up to 50 MHz. The measured RPN traces at different output power levels are shown in



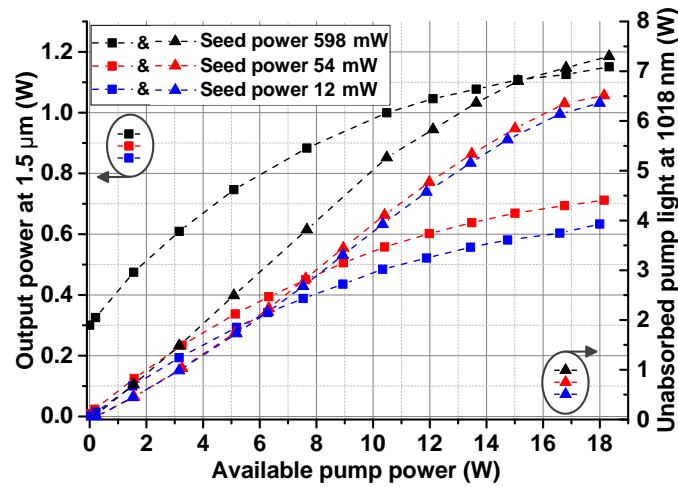
**Figure 6.6:** Relative power noise up to 50 MHz at different output power levels of the  $\text{Er}^{3+}:\text{Yb}^{3+}$ -codoped fiber amplifier seeded with 5 mW. The calculated shot noise level (red dashed), the technical noise (solid black), and the total noise floor (dashed red) are also plotted.

Fig. 6.6. The calculated shot noise level and the contribution of the technical noise are also plotted. It can be seen that all noise spectra are limited by the shot and the technical noise level at frequencies above  $\sim 35$  MHz. No power-dependent broadband noise was observed. Therefore, the amplifier was SBS-free up to 1.2 W. The three peaks at  $\sim 16$  MHz,  $\sim 23$  MHz and  $\sim 38$  MHz are narrowband features originally found in the pump light at the output of the fiber laser at 1018 nm, and are not directly related to the  $\text{Er}^{3+}:\text{Yb}^{3+}$ -codoped fiber amplifier itself.

#### 6.4 $\text{Er}^{3+}$ -Doped $\text{Yb}^{3+}$ -Free Fiber Amplifier Pumped at 1018 nm

Although very small, the absorption cross section of  $\text{Er}^{3+}$  at 1018 nm is not zero. In this section, an  $\text{Er}^{3+}$ -doped  $\text{Yb}^{3+}$ -free fiber is tested in the core-pump setup. The fact that the fiber is  $\text{Yb}^{3+}$ -free permits to study the behavior of  $\text{Er}^{3+}$  when it is pumped at 1018 nm (which also happens to a very little extent in codoped fibers) without the limitation of the  $\text{Yb}^{3+}$ -band ASE. This experiment serves to study an extreme situation of the *off-peak* pumping concept where the absorption is very low but the pump intensity very high.





**Figure 6.7:** Output power and unabsorbed pump light vs. available pump power in the Er<sup>3+</sup>-doped Yb<sup>3+</sup>-free fiber amplifier for seed power levels of 12 mW, 54 mW and 598 mW. The squares represent the output power at 1556 nm and the triangles the unabsorbed pump light at 1018 nm.

The sample under test was a 5 m-long Er30-4/125 (*Liekki*). This Er<sup>3+</sup>-doped fiber has a core diameter of 4 μm with a NA of 0.20. The absorption of the Er30-4/125 was measured with the fiber analyzer OFAS2500 (*Photon Kinetics*), being ~0.7 dB/m at 1018 nm and ~12 dB/m at 1556 nm. The available pump power at the beginning of the fiber was ~18 W, making the maximum pump intensity in the fiber as high as ~143 MW/cm<sup>2</sup>. The output power and residual pump light versus the available pump power are shown in Fig. 6.7 for the seed power levels of 12 mW, 54 mW and 598 mW. The maximum output power were 633 mW, 721 mW and 1.15 W respectively. The residual pump light (now only composed by unabsorbed pump light since there is no Yb<sup>3+</sup>-band ASE) at the maximum pump power was higher the higher the seed power was. This is an unexpected phenomenon since, in general, a higher seed power favors higher pump light absorption, which leads to lower residual pump light at the output. As it was discussed in Chapter 4, higher power at the seed wavelength reduces the effective lifetime of the atomic transition  $^4I_{13/2} \rightarrow ^4I_{15/2}$ . This speeds up the absorption  $\rightarrow$  relaxation cycle and therefore leaves Er<sup>3+</sup> ions available to absorb a new pump photon at a higher rate. In Fig. 6.8 the calculated gain (Fig. 6.8(a)) and pump absorption (Fig. 6.8(b)) versus the pump power are shown for the three seed power levels. It can be observed that with a very low pump power the absorption for a seed power of 54 mW is slightly higher than for a seed power of 12 mW, but significantly higher than for a seed power of 598 mW. In the three cases the pump absorption decreases as the pump power (and consequently also the seed signal) increases. This tendency reverts at the pump power of 12 W for the seed power levels of 54 mW and 12 mW, and at 10 W for the seed power of 598 mW, reaching the minimum absorption level and starting an increasing trend.

These anomalies occurring to the pump power absorption motivated simulations to find the possible physical mechanisms causing them. The simulations calculated numerically

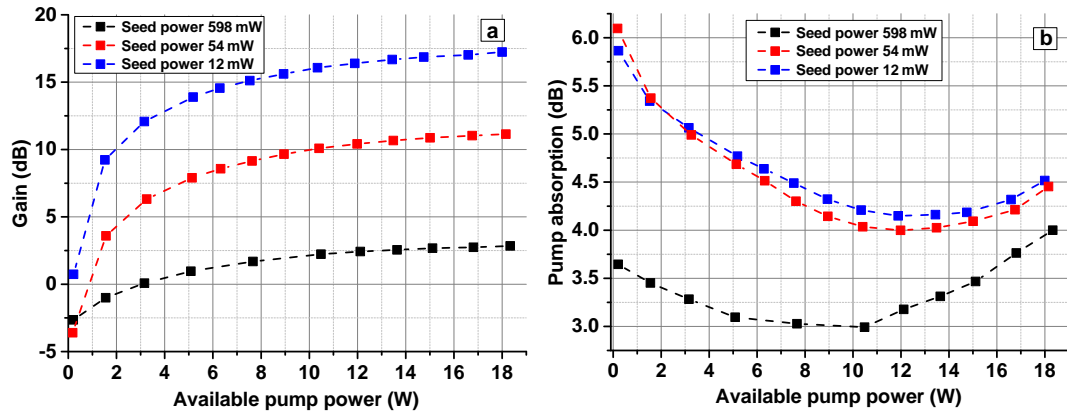


**Figure 6.8:** (a): Gain and (b): pump absorption of the  $\text{Er}^{3+}$ -doped  $\text{Yb}^{3+}$ -free fiber amplifier when the seed power was 12 mW, 54 mW and 598 mW.

the power at the seed and pump wavelengths along the fiber for different pump power levels. The  $\text{Er}^{3+}$ -doped fiber amplifier was modeled as a three-level system, neglecting the influence of energy levels others than  $^4\text{I}_{15/2}$ ,  $^4\text{I}_{13/2}$  and  $^4\text{I}_{11/2}$ . The simulations could not reproduce the laboratory results with realistic values of the lifetimes of the energy levels, absorption and emission cross sections at 1018 nm, fiber length, dopant concentration and seed power. It was only possible to simulate an increase of the pump absorption with a decrease of the seed power in the case of very long active fiber and very low pump power (e.g., 40 m and 0.1 W). However, a number of effects involving higher energy levels were not taken into account in the simulations such as upconversion. Another effect generally associated to high pump light intensity that was not contemplated in the simulations is the excited-state absorption (ESA). ESA occurs when an  $\text{Er}^{3+}$  ion already in the energy level  $^4\text{I}_{11/2}$  absorbs another pump photon and excites the higher energy level  $^4\text{F}_{7/2}$ . The actual probability of these and other non-linear processes are unknown when core-pumping at 1018 nm, and their effects in the gain and absorption of  $\text{Er}^{3+}$ -doped fiber amplifiers are not clear. Therefore, although it was not possible to determine the nature of the unexpected effects shown in Fig. 6.7 and Fig. 6.8, they could be due to processes involving energy levels not included in the simulations, the high intensity and the unusual pump wavelength.

## 6.5 Conclusion

$\text{Er}^{3+}$ -doped and  $\text{Er}^{3+}:\text{Yb}^{3+}$ -codoped fiber amplifiers at 1556 nm core-pumped at 1018 nm have been proposed and demonstrated for the first time. An  $\text{Yb}^{3+}$ -doped fiber laser was employed as the source to pump the main amplifier. The system was monolithic, purely single-mode and was made exclusively with standard components which are commercially available. The setup was tested with four different  $\text{Er}^{3+}:\text{Yb}^{3+}$ -codoped fibers, showing important differences in their performances. Because of the low absorption cross section of the active fibers at 1018 nm, the pump concept corresponds to an *off-peak* pumping, which enables a more homogeneously pump light absorption compared to the common pumping at 976 nm as it was discussed in Chapter 5. This enhances the optical-to-optical efficiency

and reduces the  $\text{Yb}^{3+}$ -band ASE. An output power of 11.6 W at 1556 nm and an efficiency of more than 48 % were achieved with a 1.9 m-long sample of the active fiber TC1500Y. This amplifier was limited by the available pump power. Although the efficiency of the amplifier made of the other three  $\text{Er}^{3+}:\text{Yb}^{3+}$ -codoped fiber samples was relatively good, the power scaling was seriously limited by (i)  $\text{Yb}^{3+}$ -band ASE in the short term and (ii) a strong PD-like power deterioration on the minutes- and hours- scale. The results suggest that such PD effect is a consequence of the high intensities, given the relatively high power levels in the core of the single-mode fibers.

With a low seed power level of 5 mW, the amplifier reached an output power of 1.2 W with an efficiency of 30 %. The comparison with a similar  $\text{Er}^{3+}:\text{Yb}^{3+}$ -codoped amplifier cladding-pumped at 976 nm showed a remarkably better performance with almost half of the fiber length. In this case the limiting factor was the  $\text{Er}^{3+}$ -band ASE while the  $\text{Yb}^{3+}$ -band ASE was not an issue. No signs of SBS were found in the amplified signal up to the maximum output power level.

An  $\text{Er}^{3+}$ -doped  $\text{Yb}^{3+}$ -free fiber amplifier pumped at 1018 nm was also demonstrated for the first time. The amplifier seeded with 12 mW achieved up to 633 mW with a 5 m-long active fiber. In the measurements, the residual pump light was lower the lower the seed power was. Additionally, the pump power absorption dropped as the available pump power increased for the three tested seed power levels. This absorption drop stopped at a certain power level to later start increasing again. These unexpected effects could not be reproduced in simulations and a satisfactory explanation for them was not found.

The experiments presented in this chapter were meant as proof-of-principles. Further investigations must be conducted to better understand the actual potential of the proposed concepts presented here in laser sources for GWDs. It seems feasible to reach power levels up to few tens of watts with optimized core-pumped systems and purely single-mode fibers. This is obviously far from the power levels one can expect from amplifiers based on LMA fibers such as the presented in Chapter 5, but sufficient to fulfill the requirements of, for example, the current conceptual design of the Einstein Telescope [Tea11]. Besides this, the low complexity, intrinsic single-modeness and wide commercial availability of the components favor this type of architecture.

The experiment with the core-pumped  $\text{Er}^{3+}$ -doped  $\text{Yb}^{3+}$ -free fiber amplifier pumped at 1018 nm had the primary goal to test the *off-peak* pumping concept by studying an extreme case. In any case, such kind of amplifier has certain properties desirable in preamplifiers for low seed power. One is the fact that  $\text{Er}^{3+}$ -doped amplifiers do not produce  $\text{Yb}^{3+}$ -band ASE, therefore the risk of introducing  $\text{Yb}^{3+}$ -band ASE in a following  $\text{Er}^{3+}:\text{Yb}^{3+}$ -codoped amplifier is eliminated. Another potential feature is that the amount of unabsorbed pump light would be quite high (since even if the majority of the pump light is not absorbed, it is necessary to achieve a high population inversion level), and already in the core of a single-mode fiber. Therefore it could be recycled to, for example, core-pump a subsequent core-pumped  $\text{Er}^{3+}:\text{Yb}^{3+}$ -codoped amplifier. In such concept the preamplifier output would both seed and pump the main amplifier. Concerning novel pump techniques, the combination of core- and cladding-pump concepts using different pump wavelength in multi-clad fibers is an interesting topic not studied yet.



# CHAPTER 7

---

## Summary and Outlook

---

Most certainly, next-generation GWDs will use cryogenically cooled silicon instead of silica for its optics due to its better mechanical properties. Silicon is not transparent at 1064 nm, thus the laser wavelength will also change to, most probably, around 1550 nm. In this scenario, fiber technology has become a promising option to address the requirements of laser sources for GWDs. In this thesis important aspects of laser sources for next-generation GWDs have been studied, including temporal dynamics of Er<sup>3+</sup>-doped fiber amplifiers and novel pump techniques for power scaling single-frequency and single-mode fiber amplifiers at 1.5  $\mu\text{m}$ .

The dynamics of Er<sup>3+</sup>-doped fiber amplifiers were studied in Chapter 4. An analytical model was presented and experimentally validated. Combining the model and the experimental data, the spontaneous lifetimes of the Er<sup>3+</sup> energy levels  $^4\text{I}_{13/2}$  and  $^4\text{I}_{11/2}$  were estimated to be  $\sim 8.7$  ms and 8-10  $\mu\text{s}$ . It was demonstrated that the pump-to-output-signal transfer function is a low-pass multiplied by a function that can be either a damped low-pass or a damped high-pass. This is a consequence of the dependency of the effective lifetime of the metastable energy level  $^4\text{I}_{13/2}$  on the output power. It was also shown that the pump-to-phase-shift transfer function is induced by the temperature generated due to the quantum defect, and filtered by the transfer function of the energy level  $^4\text{I}_{11/2}$ . Once the suitability of the model was validated, it was used to simulate a variety of different scenarios depending on the output power and seed wavelength. Three operation regimes were defined depending on the action of the term that multiplies the low-pass in the pump-to-output-signal transfer function. The power thresholds that make this term a damped low-pass and a damped high-pass were computed, and their evolution with wavelength was studied. The transfer function was simulated at each regime for different seed wavelengths to show to what extent the transfer function can be changed by tuning the output power. The simulation of the transfer functions can be a tool to estimate how pump fluctuations will couple to the amplified signal. The model can also be used to assist in the design of control systems based on feedback to the pump power. The shape of the transfer function can potentially be tuned to limit the noise coupling from the pump source. This, in turn, can set a criterion to the choice of a final wavelength in next-generation GWDs in the case where Er<sup>3+</sup>-doped fiber amplifiers were used in, for example, preamplifiers. The model can also provide information about the pump-to-phase-shift transfer function, which might be potentially useful in the design of actuating and control strategies in CBC systems. Up-conversion and KKR demonstrated to have a negligible impact at low power levels but their influence at high power levels remains uninvestigated.

In Chapter 5, the so-called *off-peak* pump concept was applied to a high power all-fiber  $\text{Er}^{3+}:\text{Yb}^{3+}$ -codoped amplifier. The output power was pump-power limited at 111 W, from which  $\sim 100$  W were in the linearly-polarized  $\text{TEM}_{00}$  mode. The concept demonstrated to distribute the pump power (and therefore the absorption) more homogeneously along the fiber compared to pumping at 976 nm. This has a beneficial impact on the  $\text{Yb}^{3+}$ -to- $\text{Er}^{3+}$  energy transfer efficiency which leads to an effective suppression of  $\text{Yb}^{3+}$ -band ASE. The optical-to-optical slope efficiency was 46 % and the  $\text{Er}^{3+}$ -band ASE suppression was more than 54 dB. Despite of the non-PM fibers used in the setup, the PER was 12.8 dB. Very small power fluctuations of  $\pm 0.2$  % were measured in 1 hour of operation. The relative power noise characterization showed that the amplifier has a noise-damping effect at frequencies below 1 kHz. No impact on the frequency noise was detected and the amplified signal was SBS-free up to the maximum output power. After having studied the benefits of the *off-peak* pumping in high power  $\text{Er}^{3+}:\text{Yb}^{3+}$ -codoped fiber amplifiers, it seems a very promising concept to apply in laser sources for GWDs. The studies presented in this thesis motivated the development of an engineering prototype in collaboration with the AEI to further investigate its potential as a high power amplifier for single-frequency signals at 1.5  $\mu\text{m}$ . Important improvements are being considered in the design of the enhanced version such as the use of PM fibers, a splice-free design and higher pump power.

A combination of the *off-peak* pump and the core-pump concepts was presented in Chapter 6. A purely single-mode  $\text{Er}^{3+}:\text{Yb}^{3+}$ -codoped fiber amplifier core-pumped at 1018 nm was demonstrated. The test of four different active fibers revealed important differences in their performances. With a seed power of 624 mW, up to 11.6 W output power at 1556 nm was obtained with more than 48 % efficiency. An important degradation was observed in the output power when the intensity of light at 1556 nm exceeded approximately 21  $\text{MW}/\text{cm}^2$  in the fiber core. Such effect was, likely, the manifestation of photodarkening. Seeding with low power, the amplifier was compared with a standard  $\text{Er}^{3+}:\text{Yb}^{3+}$ -codoped fiber amplifier cladding pumped at 976 nm. When seeded with only 5 mW, the amplifier core-pumped at 1018 nm exhibited higher output power using a shorter piece, reaching up to 1.2 W output power with 190 cm of fiber. The applicability of core-pumped single-mode amplifiers lies in the fact that they can likely provide moderate power levels without suffering from issues related to HOMs. Hence, the results presented here invite to keep investigating the properties and scalability of such amplifiers. In particular, the study of photodarkening and techniques to mitigate it. An extreme case of low absorption and high pump intensity was studied by core-pumping an  $\text{Er}^{3+}$ -doped  $\text{Yb}^{3+}$ -free fiber amplifier at 1018 nm. It was demonstrated that it is possible to pump  $\text{Er}^{3+}$  at 1018 nm. An output power level of 633 mW was obtained when the seed power was 12 mW. It was observed that the pump absorption decreases as the pump power increases, and continues to increase after a certain power level even without significant increase of the amplified signal. This represents a trade-off between the output power and the efficiency since a relevant amount of energy is lost due to up-conversion and heat. The fact that  $\text{Er}^{3+}$ -doped fiber amplifiers do not produce 1  $\mu\text{m}$ -band ASE may be an interesting feature in preamplifiers before high power  $\text{Er}^{3+}:\text{Yb}^{3+}$ -codoped fiber amplifiers. Using fiber lasers as pump sources instead of diodes enables other options such as to core-pump  $\text{Er}^{3+}$  (either with or without  $\text{Yb}^{3+}$ -codoping) in-band at 15xx nm. This alternative can be an interesting future line of investigation regarding laser sources for next-generation GWDs.

---

## Bibliography

---

- [Abb16] B. P. Abbott and et. al., ‘GW151226: Observation of Gravitational Waves from a 22-Solar-Mass Binary Black Hole Coalescence’. *Phys. Rev. Lett.* **116**, p. 241103 (2016) (cit. on p. 2).
- [Agr07] G. P. Agrawal, *Nonlinear fiber Optics*. 4th ed. Academic Press (2007) (cit. on pp. 12, 20, 21).
- [Bec99] P. Becker, A. Olsson, and J. Simpson, *Erbium-Doped Fiber Amplifiers*. 1st ed. Academic Press (1999) (cit. on p. 14).
- [Boo18] P. Booker, R. Caspary, J. Neumann, D. Kracht, and M. Steinke, ‘Pump wavelength dependence of ASE and SBS in single-frequency EYDFAs’. *Opt. Lett.* **43** (19), pp. 4647–4650 (2018) (cit. on p. 42).
- [Bro99] N. G. R. Broderick, H. L. Offerhaus, D. J. Richardson, R. A. Sammut, J. Caplen, and L. Dong, ‘Large Mode Area Fibers for High Power Applications’. *Optical Fiber Technology* **5** (2), pp. 185–196 (1999) (cit. on p. 7).
- [Bro01] D. C. Brown and H. J. Hoffman, ‘Thermal, stress, and thermo-optic effects in high average power double-clad silica fiber lasers’. *IEEE Journal of Quantum Electronics* **37** (2), pp. 207–217 (2001) (cit. on p. 32).
- [Che10] H. Chen, T. Sosnowski, C. Liu, L. Chen, J. R. Birge, A. Galvanauskas, F. X. Kärtner, and G. Chang, ‘Chirally-coupled-core Yb-fiber laser delivering 80-fs pulses with diffraction-limited beam quality warranted by a high-dispersion mirror based compressor’. *Opt. Express* **18** (24), pp. 24699–24705 (2010) (cit. on p. 8).
- [Col17] LIGO Scientific Collaboration, *Instrument Science White Paper*. Technical Note. LIGO (2017) (cit. on p. 2).
- [Cre16] D. Creeden, H. Pretorius, J. Limongelli, and S. D. Setzler, ‘Single frequency 1560 nm Er: Yb fiber amplifier with 207 W output power and 50.5% slope efficiency’. *Proc. SPIE*. Vol. 9728, p. 97282L (2016) (cit. on pp. 9, 20, 41).
- [Dam03] M. J. Damzen, V. I. Vlad, V. Babin, and A. Mocofanescu, *Stimulated Brillouin Scattering. Fundamentals and Applications*. 1st ed. Institute of Physics Publishing (2003) (cit. on p. 21).
- [Dig01] M. J. G. Dignonnet, *Rare-Earth-Doped Fiber Lasers and Amplifiers*. Marcel Dekker, Inc. (2001) (cit. on p. 15).

- [Dig97] M.J.F. Digonnet, R.W. Sadowski, H.J. Shaw, and R.H. Pantell, ‘Resonantly Enhanced Nonlinearity in Doped Fibers for Low-Power All-Optical Switching: A Review’. *Optical Fiber Technology* **3** (1), pp. 44–64 (1997) (cit. on pp. 33, 35).
- [Don95] L. Dong, J. L. Archambault, L. Reekie, P. St. J. Russell, and D. N. Payne, ‘Photoinduced absorption change in germanosilicate preforms: evidence for the color-center model of photosensitivity’. *Appl. Opt.* **34** (18), pp. 3436–3440 (1995) (cit. on p. 60).
- [Don09] L. Dong, H. A. McKay, L. Fu, M. Ohta, A. Marcinkevicius, S. Suzuki, and M. E. Fermann, ‘Ytterbium-doped all glass leakage channel fibers with highly fluorine-doped silica pump cladding’. *Opt. Express* **17** (11), pp. 8962–8969 (2009) (cit. on p. 8).
- [Ein16] A. Einstein, ‘Die Grundlage der allgemeinen Relativitätstheorie’. *Annalen der Physik* **354** (7), pp. 769–822 (1916) (cit. on p. 1).
- [Fan14] Q. Fang, W. Shi, Y. Qin, X. Meng, and Q. Zhang, ‘2.5 kW monolithic continuous wave (CW) near diffraction-limited fiber laser at 1080 nm’. *Laser Physics Letters* **11** (10), p. 105102 (2014) (cit. on p. 19).
- [Fot09] Andrei A. Fotiadi, Nikita Zakharov, Oleg L. Antipov, and Patrice Mégret, ‘All-fiber coherent combining of Er-doped amplifiers through refractive index control in Yb-doped fibers’. *Opt. Lett.* **34** (22), pp. 3574–3576 (2009) (cit. on p. 23).
- [Fuj15] A. Fujisaki, S. Matsushita, K. Kasai, M. Y., T. Hirooka, and M. Nakazawa, ‘An 11.6 W output, 6 kHz linewidth, single-polarization EDFA-MOPA system with a  $^{13}\text{C}_2\text{H}_2$  frequency stabilized fiber laser’. *Opt. Express* **23** (2), pp. 1081–1087 (2015) (cit. on pp. 16, 56).
- [Gre95] M. A. Green and M. J. Keevers, ‘Optical properties of intrinsic silicon at 300 K’. *Progress in Photovoltaics: Research and Applications* **3** (3), pp. 189–192 (1995) (cit. on p. 2).
- [Han10] Q. Han, J. Ning, and Z. Sheng, ‘Numerical Investigation of the ASE and Power Scaling of Cladding-Pumped Er-Yb Codoped Fiber Amplifiers’. *IEEE Journal of Quantum Electronics* **46** (11), pp. 1535–1541 (2010) (cit. on pp. 42, 43).
- [Han15] Q. Han, Y. Yao, Y. Chen, F. Liu, T. Liu, and H. Xiao, ‘Highly efficient Er/Yb-codoped fiber amplifier with an Yb-band fiber Bragg grating’. *Opt. Lett.* **40** (11), pp. 2634–2636 (2015) (cit. on p. 46).
- [Han01] J. Hansryd, F. Dross, M. Westlund, P. A. Andrekson, and S. N. Knudsen, ‘Increase of the SBS Threshold in a Short Highly Nonlinear Fiber by Applying a Temperature Distribution’. *J. Lightwave Technol.* **19** (11), p. 1691 (2001) (cit. on pp. 22, 53).
- [Hil08] M. Hildebrandt, S. Büsche, P. Weßels, M. Frede, and D. Kracht, ‘Brillouin scattering spectra in high-power single-frequency ytterbium doped fiber amplifiers’. *Opt. Express* **16** (20), pp. 15970–15979 (2008) (cit. on p. 52).



- [Hor97] M. Horowitz, A. R. Chraplyvy, R. W. Tkach, and J. L. Zyskind, ‘Broadband transmitted intensity noise induced by Stokes and anti-Stokes Brillouin scattering in single-mode fibers’. *IEEE Photonics Technology Letters* **9** (1), pp. 124–126 (1997) (cit. on pp. 21, 52).
- [Hua17] L. Huang, H. Wu, R. Li, L. Li, P. Ma, X. Wang, J. Leng, and P. Zhou, ‘414 W near-diffraction-limited all-fiberized single-frequency polarization-maintained fiber amplifier’. *Opt. Lett.* **42** (1), pp. 1–4 (2017) (cit. on p. 19).
- [Hwa00] B. C. Hwang, S. Jiang, T. Luo, J. Watson, G. Sorbello, and N. Peyghambarian, ‘Cooperative upconversion and energy transfer of new high  $\text{Er}^{3+}$ - and  $\text{Yb}^{3+}$ - $\text{Er}^{3+}$ -doped phosphate glasses’. *J. Opt. Soc. Am. B* **17** (5), pp. 833–839 (2000) (cit. on p. 19).
- [Jau12] C. Jauregui, T. Eidam, H.-J. Otto, F. Stutzki, F. Jansen, J. Limpert, and A. Tünnermann, ‘Temperature-induced index gratings and their impact on mode instabilities in high-power fiber laser systems’. *Opt. Express* **20** (1), pp. 440–451 (2012) (cit. on p. 55).
- [Jau13] C. Jauregui, H.-J. Otto, F. Stutzki, F. Jansen, J. Limpert, and A. Tünnermann, ‘Passive mitigation strategies for mode instabilities in high-power fiber laser systems’. *Opt. Express* **21** (16), pp. 19375–19386 (2013) (cit. on p. 55).
- [Jeb14] M. A. Jebali, J. N. Maran, and S. LaRochelle, ‘264 W output power at 1585 nm in Er-Yb codoped fiber laser using in-band pumping’. *Opt. Lett.* **39** (13), pp. 3974–3977 (2014) (cit. on pp. 8, 56).
- [Jet08] S. Jetschke, S. Unger, A. Schwuchow, M. Leich, and J. Kirchhof, ‘Efficient Yb laser fibers with low photodarkening by optimization of the core composition’. *Opt. Express* **16** (20), pp. 15540–15545 (2008) (cit. on p. 60).
- [Jia03] C. Jiang, W. Hu, and Q. Zeng, ‘Numerical analysis of concentration quenching model of  $\text{Er}^{3+}$ -doped phosphate fiber amplifier’. *IEEE J. Quantum Electron.* **39** (10), pp. 1266–1271 (2003) (cit. on p. 8).
- [Jud62] B. R. Judd, ‘Optical Absorption Intensities of Rare-Earth Ions’. *Phys. Rev.* **127**, pp. 750–761 (1962) (cit. on p. 13).
- [Kar97] M. Karasek, ‘Optimum design of  $\text{Er}^{3+}$ - $\text{Yb}^{3+}$  codoped fibers for large-signal high-pump-power applications’. *IEEE Journal of Quantum Electronics* **33** (10), pp. 1699–1705 (1997) (cit. on p. 18).
- [Kir15] N. V. Kiritchenko, L. V. Kotov, M. A. Melkumov, M. E. Likhachev, M. M. Bubnov, M. V. Yashkov, A. Yu Laptev, and A. N. Guryanov, ‘Effect of ytterbium co-doping on erbium clustering in silica-doped glass’. *Laser Physics* **25** (2), p. 025102 (2015) (cit. on p. 8).
- [Kob10] A. Kobayakov, M. Sauer, and D. Chowdhury, ‘Stimulated Brillouin scattering in optical fibers’. *Adv. Opt. Photon.* **2** (1), pp. 1–59 (2010) (cit. on p. 20).

- [Kop08] J. Koponen, M. Laurila, and M. Hotoleanu, ‘Inversion behavior in core- and cladding-pumped Yb-doped fiber photodarkening measurements’. *Appl. Opt.* **47** (25), pp. 4522–4528 (2008) (cit. on p. 60).
- [Kop07] J. Koponen, M. Söderlund, H. J. Hoffman, D. Kliner, and J. Koplow, ‘Photodarkening measurements in large mode area fibers’. Vol. 6453, pp. 6453 - 6453 - 11 (2007) (cit. on p. 60).
- [Kov05] V. I. Kovalev, R. G. Harrison, J. Nilsson, Y. Jeong, V. Hernandez-Solis, and J. K. Sahu, ‘Analytic modeling of Brillouin gain in rare-earth doped fiber amplifiers with high-power single-frequency signals’. Vol. 5, p. 5709 (2005) (cit. on p. 21).
- [Kuh11] V. Kuhn, D. Kracht, J. Neumann, and P. Wessels, ‘Er-doped photonic crystal fiber amplifier with 70 W of output power’. *Opt. Lett.* **36** (16), pp. 3030–3032 (2011) (cit. on p. 49).
- [Kwe07] P. Kwee, F. Seifert, B. Willke, and K. Danzmann, ‘Laser beam quality and pointing measurement with an optical resonator’. *Review of Scientific Instruments* **78** (7), p. 073103 (2007) (cit. on pp. 48, 51).
- [Kwe09] P. Kwee, B. Willke, and K. Danzmann, ‘Shot-noise-limited laser power stabilization with a high-power photodiode array’. *Opt. Lett.* **34** (19), pp. 2912–2914 (2009) (cit. on p. 53).
- [Kyo93] M. Kyoto, Y. Ohoga, S. Ishikawa, and Y. Ishiguro, ‘Characterization of fluorine-doped silica glasses’. *Journal of Materials Science* **28** (10), pp. 2738–2744 (1993) (cit. on p. 13).
- [Lar06] M. Laroche, S. Girard, J. K. Sahu, W. A. Clarkson, and J. Nilsson, ‘Accurate efficiency evaluation of energy-transfer processes in phosphosilicate Er<sup>3+</sup>-Yb<sup>3+</sup>-codoped fibers’. *J. Opt. Soc. Am. B* **23** (2), pp. 195–202 (2006) (cit. on p. 19).
- [Lay77] C. B. Layne, W. H. Lowdermilk, and M. J. Weber, ‘Multiphonon relaxation of rare-earth ions in oxide glasses’. *Phys. Rev. B* **16**, pp. 10–20 (1977) (cit. on pp. 14, 31).
- [Li14] N. Li, S. Yoo, X. Yu, D. Jain, and J. K. Sahu, ‘Pump Power Depreciation by Photodarkening in Ytterbium-Doped Fibers and Amplifiers’. *IEEE Photonics Technology Letters* **26** (2), pp. 115–118 (2014) (cit. on p. 60).
- [Lie03] A. Liem, J. Limpert, H. Zellmer, and A. Tünnermann, ‘100-W single-frequency master-oscillator fiber power amplifier’. *Opt. Lett.* **28** (17), pp. 1537–1539 (2003) (cit. on p. 7).
- [Lim17] J. R. Limongelli, S. D. Setzler, and D. Creeden, ‘Experimental and numerical analysis of high power Er:Yb co-doped fiber amplifiers’. Vol. 10083, pp. 10083 - 10083 - 8 (2017) (cit. on p. 43).
- [Liu13] Y. Liu, J. Cao, H. Xiao, S. Guo, L. Si, and L. Huang, ‘Study on the output properties of fiber lasers operating near 980 nm’. *J. Opt. Soc. Am. B* **30** (2), pp. 266–274 (2013) (cit. on p. 55).

- [Mar77] D. Marcuse, ‘Loss analysis of single-mode fiber splices’. *The Bell System Technical Journal* **56** (5), pp. 703–718 (1977) (cit. on p. 57).
- [Nil93] J. Nilsson, B. Jaskorzynska, and P. Blixt, ‘Performance reduction and design modification of erbium-doped fiber amplifiers resulting from pair-induced quenching’. *IEEE Phot. Tech. Lett.* **5** (12), pp. 1427–1429 (1993) (cit. on p. 8).
- [Nis14] R. Nishiuchi and K. Suzuki, ‘Present status of the laser system’. *KAGRA F2F Meeting*. (2014) (cit. on p. 2).
- [Nod86] J. Noda, K. Okamoto, and Y. Sasaki, ‘Polarization-maintaining fibers and their applications’. *Journal of Lightwave Technology* **4** (8), pp. 1071–1089 (1986) (cit. on p. 47).
- [Nuf15] Nufern, *Selecting the Optimal Er/Yb Doped Optical Fiber: Design Considerations and System Performances*. Published on 2015. Visited on Dec. 2017. Application Note. Available at <http://www.nufern.com/library/getpdf/id/483> (2015) (cit. on p. 59).
- [Ofe62] G. S. Ofelt, ‘Intensities of Crystal Spectra of Rare-Earth Ions’. *The Journal of Chemical Physics* **37** (3), pp. 511–520 (1962) (cit. on p. 13).
- [Ola10] C. B. Olausson, A. Shirakawa, M. Chen, J. K. Lyngsø, J. Broeng, K. P. Hansen, A. Bjarklev, and K. Ueda, ‘167 W, power scalable ytterbium-doped photonic bandgap fiber amplifier at 1178nm’. *Opt. Express* **18** (16), pp. 16345–16352 (2010) (cit. on p. 8).
- [Reb97] M. A. Rebolledo, S. Jarabo, M. Hotoleanu, M. Karasek, E. Grolmus, and E. Jaunart, ‘Analysis of a technique to determine absolute values of the stimulated emission cross section in erbium-doped silica fibres from gain measurements’. *Pure and Applied Optics: Journal of the European Optical Society Part A* **6** (3), p. 425 (1997) (cit. on p. 43).
- [Rob18] T. Robin, T. Gotter, A. Barnini, P. Guitton, R. Montron, G. Mélin, C. Ranger, A. Laurent, and B. Cadier, ‘Evidence of photo-darkening in co-doped erbium-ytterbium double-clad fibers operated at high-output power’. Vol. 10528, pp. 10528 - 10528 - 9 (2018) (cit. on p. 60).
- [Sab70] V. De Sabbata, P. Fortini, C. Gualdi, and S. Petralia, ‘A Proposal for Combined Efforts Regarding Geophysical Research and Detection of Gravitational Waves’. *Annals of Geophysics* **23** (1), pp. 21–25 (1970) (cit. on p. 1).
- [San93] F. Sanchez, P. Le Boudec, P. François, and G. Stephan, ‘Effects of ion pairs on the dynamics of erbium-doped fiber lasers’. *Phys. Rev. A* **48**, pp. 2220–2229 (1993) (cit. on pp. 14, 31).
- [Sch09] C. Schwarz et al., ‘Cryogenic Setup for Q-factor measurements on bulk materials for future gravitational wave detectors’. *Proc. ICEC22-ICMC2008* (2009) (cit. on p. 2).

- [Sef04] G. A. Sefler, W. D. Mack, G. C. Valley, and T. S. Rose, ‘Secondary energy transfer and nonparticipatory Yb<sup>3+</sup> ions in Er<sup>3+</sup>-Yb<sup>3+</sup> high-power amplifier fibers’. *J. Opt. Soc. Am. B* **21** (10), pp. 1740–1748 (2004) (cit. on p. 19).
- [She05] D. Y. Shen, J. K. Sahu, and W. A. Clarkson, ‘Highly efficient Er,Yb-doped fiber laser with 188 W free-running and >100 W tunable output power’. *Opt. Express* **13** (13), pp. 4916–4921 (2005) (cit. on p. 46).
- [Sob11] G. Sobon, P. Kaczmarek, A. Antonczak, J. Sotor, and K. M. Abramski, ‘Controlling the 1  $\mu$ m spontaneous emission in Er/Yb co-doped fiber amplifiers’. *Opt. Express* **19** (20), pp. 19104–19113 (2011) (cit. on p. 41).
- [Ste14a] M. Steinke, A. Croteau, C. Paré, H. Zheng, P. Laperle, A. Proulx, J. Neumann, D. Kracht, and P. Wessels, ‘Co-seeded Er<sup>3+</sup>:Yb<sup>3+</sup> single frequency fiber amplifier with 60 W output power and over 90 % TEM<sub>00</sub> content’. *Opt. Express* **22** (14), pp. 16722–16730 (2014) (cit. on pp. 8, 20, 49).
- [Ste14b] M. Steinke, A. Croteau, C. Paré, H. Zheng, P. Laperle, A. Proulx, J. Neumann, D. Kracht, and P. Wessels, ‘Co-seeded Er<sup>3+</sup>:Yb<sup>3+</sup> single frequency fiber amplifier with 60 W output power and over 90 % TEM<sub>00</sub> content’. *Opt. Express* **22** (14), pp. 16722–16730 (2014) (cit. on p. 46).
- [Ste18] M. Steinke, J. Neumann, D. Kracht, and P. Wessels, ‘A stochastic model for the energy transfer in Er<sup>3+</sup>:Yb<sup>3+</sup>-codoped fibers’. *To be submitted* (2018) (cit. on p. 43).
- [Ste15] M. Steinke, J. Neumann, D. Kracht, and P. Wessels, ‘Gain dynamics in Er<sup>3+</sup>:Yb<sup>3+</sup> co-doped fiber amplifiers’. *Opt. Express* **23** (11), pp. 14946–14959 (2015) (cit. on pp. 8, 23, 50).
- [Sup13] V. R. Supradeepa and J. W. Nicholson, ‘Power scaling of high-efficiency 1.5 $\mu$ m cascaded Raman fiber lasers’. *Opt. Lett.* **38** (14), pp. 2538–2541 (2013) (cit. on p. 55).
- [Sup12] V. R. Supradeepa, J. W. Nicholson, and K. Feder, ‘Continuous wave Erbium-doped fiber laser with output power of >100 W at 1550 nm in-band core-pumped by a 1480nm Raman fiber laser’. *2012 Conference on Lasers and Electro-Optics (CLEO)*, pp. 1–2 (2012) (cit. on pp. 8, 16, 20).
- [Tea11] ET Science Team, *Einstein gravitational wave Telescope Conceptual Design Study*. (2011) (cit. on pp. 2, 65).
- [The16] T. Theeg, C. Ottenhues, H. Sayinc, J. Neumann, and D. Kracht, ‘Core-pumped single-frequency fiber amplifier with an output power of 158W’. *Opt. Lett.* **41** (1), pp. 9–12 (2016) (cit. on pp. 7, 56).
- [The12a] T. Theeg, H. Sayinc, J. Neumann, and D. Kracht, ‘All-Fiber Counter-Propagation Pumped Single Frequency Amplifier Stage With 300 W Output Power’. *Phot. Tech. Lett. IEEE*, **24** (20), pp. 1864–1867 (2012) (cit. on pp. 7, 22).

- [The12b] T. Theeg, H. Sayinc, J. Neumann, L. Overmeyer, and D. Kracht, ‘Pump and signal combiner for bi-directional pumping of all-fiber lasers and amplifiers’. *Opt. Express* **20** (27), pp. 28125–28141 (2012) (cit. on p. 45).
- [Trä07] F. Träger, *Springer Handbook of Lasers and Optics*. 1st ed. Springer (2007) (cit. on p. 12).
- [Tün12a] H. Tünnermann, Y. Feng, J. Neumann, D. Kracht, and P. Weßels, ‘All-fiber coherent beam combining with phase stabilization via differential pump power control’. *Opt. Lett.* **37** (7), pp. 1202–1204 (2012) (cit. on p. 23).
- [Tün11] H. Tünnermann, J. Neumann, D. Kracht, and P. Weßels, ‘All-fiber phase actuator based on an erbium-doped fiber amplifier for coherent beam combining at 1064 nm’. *Opt. Lett.* **36** (4), pp. 448–450 (2011) (cit. on pp. 23, 31).
- [Tün12b] H. Tünnermann, J. Neumann, D. Kracht, and P. Weßels, ‘Frequency resolved analysis of thermally induced refractive index changes in fiber amplifiers’. *Opt. Lett.* **37** (17), pp. 3597–3599 (2012) (cit. on pp. 32, 33).
- [Tün12c] H. Tünnermann, J. Neumann, D. Kracht, and P. Weßels, ‘Gain dynamics and refractive index changes in fiber amplifiers: a frequency domain approach’. *Opt. Express* **20** (12), pp. 13539–13550 (2012) (cit. on p. 9).
- [Var17a] O. de Varona, W. Fittkau, P. Booker, T. Theeg, M. Steinke, D. Kracht, J. Neumann, and P. Wessels, ‘Single-frequency fiber amplifier at 1.5  $\mu\text{m}$  with 100 W in the linearly-polarized TEM<sub>00</sub> mode for next-generation gravitational wave detectors’. *Opt. Express* **25** (21), pp. 24880–24892 (2017) (cit. on p. 41).
- [Var17b] O. de Varona, W. Fittkau, M. Steinke, T. Theeg, D. Kracht, J. Neumann, and P. Wessels, ‘Characterization of a 110W single-frequency monolithic fibre-amplifier at 1.5  $\mu\text{m}$  for next-generation gravitational wave detectors’. *2017 European Conference on Lasers and Electro-Optics and European Quantum Electronics Conference*. Optical Society of America, CJ-9-1 (2017) (cit. on p. 41).
- [Var16] O. de Varona, M. Steinke, D. Kracht, J. Neumann, and P. Wessels, ‘Influence of the third energy level on the gain dynamics of EDFAs: analytical model and experimental validation’. *Opt. Express* **24** (22), pp. 24883–24895 (2016) (cit. on pp. 14, 23).
- [Var18a] O. de Varona, M. Steinke, D. Kracht, J. Neumann, and P. Wessels, ‘Single-frequency and single-mode fiber amplifier at 1.5  $\mu\text{m}$  core-pumped at 1018 nm (Conference Presentation)’. *Proc. SPIE*. Vol. 10512 (2018) (cit. on p. 56).
- [Var18b] O. de Varona, M. Steinke, J. Neumann, and D. Kracht, ‘All-fiber, single-frequency, and single-mode Er<sup>3+</sup>:Yb<sup>3+</sup> fiber amplifier at 1556 nm core-pumped at 1018 nm’. *Opt. Lett.* **43** (11), pp. 2632–2635 (2018) (cit. on pp. 20, 56).
- [Wag93] J. L. Wagener, P. F. Wysocki, M. J. F. Dignonnet, H. J. Shaw, and D. J. DiGiovanni, ‘Effects of concentration and clusters in erbium-doped fiber lasers’. *Opt. Lett.* **18** (23), pp. 2014–2016 (1993) (cit. on p. 17).

- [Wan13] R. Wang, Y. Liu, J. Cao, S. Guo, L. Si, and J. Chen, ‘Experimental study on the all-fiberized continuous-wave ytterbium-doped laser operating near 980 nm’. *Appl. Opt.* **52** (24), pp. 5920–5924 (2013) (cit. on p. 55).
- [War12] B. Ward, C. Robin, and I. Dajani, ‘Origin of thermal modal instabilities in large mode area fiber amplifiers’. *Opt. Express* **20** (10), pp. 11407–11422 (2012) (cit. on pp. 8, 55).
- [Web60] J. Weber, ‘Detection and Generation of Gravitational Waves’. *Phys. Rev.* **117**, pp. 306–313 (1960) (cit. on p. 1).
- [Wei72] R. Weiss, ‘Electromagnetically coupled broadband gravitational antenna’. *Quarterly Progress Report, Research Laboratory of Electronics MIT* (1972) (cit. on p. 1).
- [Wie07] S. Wielandy, ‘Implications of higher-order mode content in large mode area fibers with good beam quality’. *Opt. Express* **15** (23), pp. 15402–15409 (2007) (cit. on p. 48).
- [Win11] L. Winkelmann, O. Puncken, R. Kluzik, C. Veltkamp, P. Kwee, J. Poeld, C. Bogan, B. Willke, M. Frede, J. Neumann, P. Wessels, and D. Kracht, ‘Injection-locked single-frequency laser with an output power of 220 W’. *Appl. Phys. B* **102** (3), pp. 529–538 (2011) (cit. on p. 7).
- [Wys18] M. Wyszomolek, C. Ottenhues, T. Pulzer, T. Theeg, H. Sayinc and M. Steinke, U. Morgner, J. Neumann, and D. Kracht, ‘Micro-structured fiber cladding light stripper for kW-class laser systems’. *Appl. Opt.* **57** (25) (2018) (cit. on p. 45).
- [Yeh90] C. Yeh, *Handbook of Fiber Optics: Theory and Applications*. 4th ed. Academic Press (1990) (cit. on pp. 12, 13).
- [Yos93] N. Yoshizawa and T. Imai, ‘Stimulated Brillouin scattering suppression by means of applying strain distribution to fiber with cabling’. *Journal of Lightwave Technology* **11** (10), pp. 1518–1522 (1993) (cit. on pp. 22, 53).
- [Zha93] F. Zhang and J. W. Y. Lit, ‘Temperature and strain sensitivity measurements of high-birefringent polarization-maintaining fibers’. *Appl. Opt.* **32** (13), pp. 2213–2218 (1993) (cit. on p. 47).
- [Zha11] J. Zhang, V. Fromzel, and M. Dubinskii, ‘Resonantly cladding-pumped Yb-free Er-doped LMA fiber laser with record high power and efficiency’. *Opt. Express* **19** (6), pp. 5574–5578 (2011) (cit. on p. 16).
- [Zho17] P. Zhou, H. Xiao, J. Leng, J. Xu, Z. Chen, H. Zhang, and Z. Liu, ‘High-power fiber lasers based on tandem pumping’. *J. Opt. Soc. Am. B* **34** (3), A29–A36 (2017) (cit. on p. 55).

---

## List of Figures

---

3.1	Total reflection in step-index optical fibers . . . . .	11
3.2	Most relevant energy levels and transitions in $\text{Er}^{3+}$ -doped fiber amplifiers . .	14
3.3	$\text{Er}^{3+}$ absorption and emission cross sections and gain spectra versus inversion level . . . . .	15
3.4	Atomic transitions involved in the gain process in $\text{Er}^{3+}$ -doped amplifiers . .	16
3.5	Typical absorption and emission cross sections of $\text{Yb}^{3+}$ -doped and $\text{Er}^{3+}$ -doped fibers . . . . .	17
3.6	Atomic transitions involved in the gain process of $\text{Er}^{3+}:\text{Yb}^{3+}$ -codoped amplifiers . . . . .	18
3.7	Spontaneous Brillouin scattering in optical fibers . . . . .	20
3.8	Typical backward propagating signal below and above the SBS threshold . .	22
4.1	Experimental setup to measure the pump-to-output-signal transfer function of an $\text{Er}^{3+}$ -doped fiber amplifier . . . . .	29
4.2	Measured pump-to-output-signal transfer functions for different output power levels . . . . .	30
4.3	Pump-to-output-signal transfer function with an output power of 250 mW and model fit . . . . .	31
4.4	Evolution of $\omega_1$ with output power . . . . .	32
4.5	Experimental setup to measure the pump-to-phase-shift transfer function . .	32
4.6	Magnitude of the pump-to-phase-shift transfer function . . . . .	34
4.7	Evolution of $\omega_1$ , $\omega_2$ and $\omega_3$ with output power and seed wavelength . . . . .	36
4.8	Evolution of $P_{\text{th}1}$ and $P_{\text{th}2}$ with seed wavelength . . . . .	37
4.9	Computed pump-to-output-signal transfer functions in an $\text{Er}^{3+}$ -doped fiber amplifier for different seed wavelengths at different $\omega$ regimes . . . . .	38
5.1	Simulation results of the $\text{Er}^{3+}:\text{Yb}^{3+}$ -codoped fiber amplifier pumped at 915 nm, 940 nm and 976 nm . . . . .	44
5.2	Experimental setup of the $\text{Er}^{3+}:\text{Yb}^{3+}$ -codoped fiber amplifier <i>off-peak</i> pumped at 940 nm . . . . .	45
5.3	Optical-to-optical slope and spectrum of the <i>off-peak</i> pumped $\text{Er}^{3+}:\text{Yb}^{3+}$ -codoped fiber amplifier . . . . .	46
5.4	Power and PER stability . . . . .	47
5.5	Experimental setup to measure the modal content . . . . .	48
5.6	Modescan at the maximum output power level . . . . .	49
5.7	Evolution of the $\text{TEM}_{00}$ mode content with output power . . . . .	49
5.8	Experimental setup to measure the relative power noise . . . . .	50

5.9	Relative power noise of the seed source at 2 W and the amplifier at 55 W and 110 W . . . . .	51
5.10	Frequency noise and calculated linewidth of the seed source at 2 W and the amplifier at 55 W and 110 W . . . . .	52
5.11	Relative power noise up to 60 MHz at different output power levels . . . . .	52
6.1	Experimental setup of the fiber amplifier core-pumped at 1018 nm . . . . .	57
6.2	Optical slopes and spectra of the $\text{Er}^{3+}:\text{Yb}^{3+}$ -codoped fiber amplifiers core-pumped at 1018 nm for different active fibers . . . . .	58
6.3	Evolution of the output power versus time and the power drop versus light intensity at 1556 nm for the different active fibers . . . . .	59
6.4	Output power and residual light vs. the pump power available in the fiber for different length of the sample TC1500Y . . . . .	60
6.5	Comparison between the amplifier core-pumped at 1018 nm and an amplifier cladding-pumped at 976 nm . . . . .	61
6.6	Relative power noise up to 50 MHz at different output power levels of the $\text{Er}^{3+}:\text{Yb}^{3+}$ -codoped fiber amplifier seeded with 5 mW . . . . .	62
6.7	Output power and unabsorbed pump light vs. available pump power in the $\text{Er}^{3+}$ -doped $\text{Yb}^{3+}$ -free fiber amplifier for seed power levels of 12 mW, 54 mW and 598 mW . . . . .	63
6.8	Gain and pump absorption of the $\text{Er}^{3+}$ -doped $\text{Yb}^{3+}$ -free fiber amplifier . . .	64



---

## List of Tables

---

4.1	Effective lifetimes $\tau_1$ and $\tau_2$ for each measured output signal power level, corresponding to the energy levels ${}^4I_{13/2}$ and ${}^4I_{11/2}$ . . . . .	30
4.2	Fiber parameters used in the computation of $P_{th1}$ , $P_{th2}$ and transfer functions . . . . .	37
5.1	Parameters used in the simulation of the <i>off-peak</i> pumped $Er^{3+}:Yb^{3+}$ -codoped fiber amplifier . . . . .	43
6.1	Fibers under test in the $Er^{3+}:Yb^{3+}$ -codoped fiber amplifier core-pumped at 1018 nm . . . . .	57



---

## Publications

---

### Journals

1. **O. de Varona**, W. Fittkau, P. Booker, T. Theeg, M. Steinke, D. Kracht, J. Neumann, and P. Wessels, ‘Single-frequency fiber amplifier at 1.5  $\mu\text{m}$  with 100 W in the linearly-polarized  $\text{TEM}_{00}$  mode for next-generation gravitational wave detectors’. *Opt. Express* **25** (21), pp. 24880–24892 (2017).
2. **O. de Varona**, M. Steinke, D. Kracht, J. Neumann, and P. Wessels, ‘Influence of the third energy level on the gain dynamics of EDFAs: analytical model and experimental validation’. *Opt. Express* **24** (22), pp. 24883–24895 (2016).
3. **O. de Varona**, M. Steinke, J. Neumann, and D. Kracht, ‘All-fiber, single-frequency, and single-mode  $\text{Er}^{3+}:\text{Yb}^{3+}$  fiber amplifier at 1556 nm core-pumped at 1018 nm’. *Opt. Lett.* **43** (11), pp. 2632–2635 (2018).
4. M. Steinke, H. Tünnermann, V. Kuhn, T. Theeg, M. Karow, **O. de Varona**, P. Jahn, P. Booker, J. Neumann, P. Weßels, and D. Kracht, ‘Single-Frequency Fiber Amplifiers for Next-Generation Gravitational Wave Detectors’. *IEEE Journal of Selected Topics in Quantum Electronics* **24** (3), pp. 1–13 (2018).

### Conferences

1. P. Booker, **O. de Varona**, P. Wessels, M. Steinke, J. Neumann, and D. Kracht, ‘Numerical investigations of off-resonant pumped  $\text{Er}^{3+}:\text{Yb}^{3+}$ -codoped fibre amplifiers’. *2017 European Conference on Lasers and Electro-Optics and European Quantum Electronics Conference*. Optical Society of America, CJ-P-12 (2017).
2. S. Hochheim, F. Wellmann, T. Theeg, **O. de Varona**, P. Booker, P. Wessels, M. Steinke, J. Neumann, and D. Kracht, ‘Monolithic fiber amplifiers for the next generation of gravitational wave detectors’. *Proc. SPIE*. Vol. 10683, p. 7 (2018).
3. **O. de Varona**, W. Fittkau, M. Steinke, T. Theeg, D. Kracht, J. Neumann, and P. Wessels, ‘Characterization of a 110 W single-frequency monolithic fibre-amplifier at 1.5  $\mu\text{m}$  for next-generation gravitational wave detectors’. *2017 European Conference on Lasers and Electro-Optics and European Quantum Electronics Conference*. Optical Society of America, CJ-9-1 (2017).
4. **O. de Varona**, J. A. Rabadán, J. F. Rufo, A. Perera, and R. Pérez, ‘Sistema de Transmisión de Audio Streaming para Comunicaciones Ópticas en Visible (VLC)’. *VII Reunión Española de Optoelectrónica*. S1 - Fibra, comunicaciones y sensores **22**, p. 11 (2011).

5. **O. de Varona**, M. Steinke, D. Kracht, J. Neumann, and P. Wessels, ‘Single-frequency and single-mode fiber amplifier at 1.5  $\mu\text{m}$  core-pumped at 1018 nm (Conference Presentation)’. *Proc. SPIE*. Vol. 10512 (2018).
6. F. Wellmann, P. Booker, S. Hochheim, T. Theeg, **O. de Varona**, W. Fittkau, L. Overmeyer, M. Steinke, P. Weßels, J. Neumann, and D. Kracht, ‘Recent progress on monolithic fiber amplifiers for next generation of gravitational wave detectors’. *Proc. SPIE*. Vol. 10512, p. 7 (2018).

#### As co-author in the LIGO Scientific Collaboration

1. ANTARES Collaboration, IceCube Collaboration, The LIGO Scientific Collaboration, and The Virgo Collaboration, ‘Search for multi-messenger sources of gravitational waves and high-energy neutrinos with Advanced LIGO during its first observing run, ANTARES and IceCube’. *Submitted to The Astrophysical Journal Letters* (2018).
2. LIGO Scientific Collaboration and Virgo Collaboration, ‘Estimating the Contribution of Dynamical Ejecta in the Kilonova Associated with GW170817’. *The Astrophysical Journal Letters* **850** (2), p. L39 (2017).
3. LIGO Scientific Collaboration and Virgo Collaboration, ‘First narrow-band search for continuous gravitational waves from known pulsars in advanced detector data’. *Phys. Rev. D* **96**, p. 122006 (2017).
4. LIGO Scientific Collaboration and Virgo Collaboration, ‘Full band all-sky search for periodic gravitational waves in the O1 LIGO data’. *Phys. Rev. D* **97**, p. 102003 (2018).
5. LIGO Scientific Collaboration and Virgo Collaboration, ‘GW170608: Observation of a 19 Solar-mass Binary Black Hole Coalescence’. *The Astrophysical Journal Letters* **851** (2), p. L35 (2017).
6. LIGO Scientific Collaboration and Virgo Collaboration, ‘GW170814: A Three-Detector Observation of Gravitational Waves from a Binary Black Hole Coalescence’. *Phys. Rev. Lett.* **119**, p. 141101 (2017).
7. LIGO Scientific Collaboration and Virgo Collaboration, ‘GW170817: Implications for the Stochastic Gravitational-Wave Background from Compact Binary Coalescences’. *Phys. Rev. Lett.* **120**, p. 091101 (2018).
8. LIGO Scientific Collaboration and Virgo Collaboration, ‘GW170817: Observation of Gravitational Waves from a Binary Neutron Star Inspiral’. *Phys. Rev. Lett.* **119**, p. 161101 (2017).
9. LIGO Scientific Collaboration and Virgo Collaboration, ‘On the Progenitor of Binary Neutron Star Merger GW170817’. *The Astrophysical Journal Letters* **850** (2), p. L40 (2017).

10. LIGO Scientific Collaboration and Virgo Collaboration, ‘Search for High-energy Neutrinos from Binary Neutron Star Merger GW170817 with ANTARES, IceCube, and the Pierre Auger Observatory’. *The Astrophysical Journal Letters* **850** (2), p. L35 (2017).
11. LIGO Scientific Collaboration and Virgo Collaboration, ‘Search for Post-merger Gravitational Waves from the Remnant of the Binary Neutron Star Merger GW170817’. *The Astrophysical Journal Letters* **851** (1), p. L16 (2017).
12. LIGO Scientific Collaboration and Virgo Collaboration, ‘Search for Tensor, Vector, and Scalar Polarizations in the Stochastic Gravitational-Wave Background’. *Phys. Rev. Lett.* **120**, p. 201102 (2018).
13. LIGO Scientific Collaboration, Virgo Collaboration, Fermi Gamma-ray Burst Monitor, and INTEGRAL, ‘Gravitational Waves and Gamma-Rays from a Binary Neutron Star Merger: GW170817 and GRB 170817A’. *The Astrophysical Journal Letters* **848** (2), p. L13 (2017).
14. The LIGO Scientific Collaboration and The Virgo Collaboration, ‘A Fermi Gamma-ray Burst Monitor search for electromagnetic signals coincident with gravitational-wave candidates in Advanced LIGO’s first observing run’. *Submitted to The Astrophysical Journal Letters* (2018).
15. The LIGO Scientific Collaboration and The Virgo Collaboration, ‘Constraining the p-mode–g-mode tidal instability with GW170817’. *Submitted to Phys. Rev. Lett.* (2018).
16. The LIGO Scientific Collaboration and The Virgo Collaboration, ‘GW170817: Measurements of neutron star radii and the equation of state’. *Phys. Rev. Lett.* **121**, p. 161101 (2018).
17. The LIGO Scientific Collaboration and The Virgo Collaboration, ‘Properties of the binary neutron star merger GW170817’. *Submitted to Phys. Rev. X* (2018).
18. The LIGO Scientific Collaboration and The Virgo Collaboration, ‘Properties of the binary neutron star merger GW170817’. *Submitted to Phys. Rev. X* (2018).
19. The LIGO Scientific Collaboration and The Virgo Collaboration, ‘Search for gravitational waves from a long-lived remnant of the binary neutron star merger GW170817’. *Submitted to The Astrophysical Journal Letters* (2018).
20. The LIGO Scientific Collaboration and The Virgo Collaboration, ‘Search for sub-solar mass ultracompact binaries in Advanced LIGO’s first observing run’. *Accepted by Phys. Rev. Lett.* (2018).
21. The LIGO Scientific Collaboration and The Virgo Collaboration, ‘Tests of General Relativity with GW170817’. *To be Submitted* (2018).

22. LIGO Scientific Collaboration and Virgo Collaboration and IceCube Collaboration and IPN Collaboration and The Insight-HXMT Collaboration and ANTARES Collaboration and The Swift Collaboration and The Dark Energy Camera GW-EM Collaboration and the DES Collaboration and The DLT40 Collaboration and GRAWITA: GRAvitational Wave Inaf TeAm and The Fermi Large Area Telescope Collaboration and ATCA: Australia Telescope Compact Array and Las Cumbres Observatory Group and OzGrav, DWF (Deeper, Wider, Faster program), AST3 and CAASTRO Collaborations and The VINROUGE Collaboration and MASTER Collaboration and J-GEM and GROWTH, JAGWAR, Caltech-NRAO, TTU-NRAO, and NuSTAR Collaborations and TZAC Consortium and KU Collaboration and Nordic Optical Telescope and ePESSTO and Texas Tech University and SALT Group and TOROS: Transient Robotic Observatory of the South Collaboration and The BOOTES Collaboration and MWA: Murchison Widefield Array and The CALET Collaboration and IKI-GW Follow-up Collaboration and LOFAR Collaboration and LWA: Long Wavelength Array and HAWC Collaboration and ALMA Collaboration and Euro VLBI Team and The Chandra Team at McGill University and DFN: Desert Fireball Network and High Time Resolution Universe Survey and SKA South Africa/MeerKAT, ‘Multi-messenger Observations of a Binary Neutron Star Merger’. *The Astrophysical Journal Letters* **848** (2), p. L12 (2017).
23. The LIGO Scientific Collaboration and The Virgo Collaboration, The 1M2H Collaboration, The Dark Energy Camera GW-EM Collaboration and the DES Collaboration, The DLT40 Collaboration, The Las Cumbres Observatory Collaboration, The VINROUGE Collaboration and The MASTER Collaboration, ‘A gravitational-wave standard siren measurement of the Hubble constant’. *Nature* **551**, pp. 85–88 (2017).

---

## Curriculum Vitae

---

### Personal data

Name Omar Enrique de Varona Ortega  
Date of birth 09.04.1986  
Place of birth Las Palmas de Gran Canaria  
Nationality Spanish

### University Education

2004 - 2011 Telecommunication Engineering at Universidad de Las Palmas de Gran Canaria  
Diploma thesis: *"Sistema de Transmisión de Audio Estéreo Digital en Tiempo Real a Través de un Enlace Óptico no Guiado en el Espectro Visible"*  
2011 - 2014 Master in Telecommunication Engineering at Universidad Carlos III de Madrid and Univesitá Degli Studi di Firenze  
Master thesis: *"Methods of Speaker Recognition for Voice Biometrics"*  
2015 Entrance exam to Leibniz Uiversität Hannover  
2015 - present PhD. candidate in physics at the Leibniz Universität Hannover

### Education

2002 - 2004 High school degree at Instituto de Educación Secundaria de Arguineguín and spanish University entrance qualification

### Professional Affiliations

2012 - 2015 Research assistant at Grupo de Optoelectrónica y Tecnología Láser at Universidad Carlos III de Madrid  
2015 - present Research scientist at Laser Zentrum Hannover e.V





---

## Acknowledgments

---

First of all I would like to express my sincere gratitude to Prof. Detlev Ristau for supervising this thesis and to Prof. Benno Willke and Prof. Volker Quetschke for accepting its evaluation.

I acknowledge Dr. Dietmar Kracht and Dr. Jörg Neumann for giving me the opportunity to work in Laser Zentrum Hannover e.V and for fostering a stimulating and friendly work environment.

I am deeply grateful to Michael Steinke and Peter Weßels for providing their support whenever I needed it, answering hundreds of questions (most of them stupid) and advising me countless times. Without their guidance, this thesis would not have been possible.

Since the first day I have felt accepted, supported and valued by the members of the Laser Development Department at Laser Zentrum Hannover. I feel fortunate to be part of a team that works with dedication and professionalism. I firmly believe that every member of this team can be proud of their work. Thanks to Sven Hochheim, Felix Wellmann, Paul Repgen, Fabian Kranert, Axel Rühl, Stefan Spiekermann, Sergii Iakushev, Moritz Hinkelmann and Mateusz Wyszomolek because, in a way or another, they all contributed in the completion of this thesis. I want to specially thank to Christoph Ottenhues, Thomas Theeg, Tony Pulzer, Katharina Hausmann and Sebastian Böhm for the fantastic help with the cleavers and splicers as well as for fabricating all the customized fiber components I needed.

I can't forget the great help from Willy Fittkau in the setup and characterization of the *off-peak* pumped high power fiber amplifier, and the invaluable contribution of Phillip Booker providing simulation scripts, fresh ideas and very interesting discussions. Success becomes easier when one is surrounded by the right people.

I especially want to thank Oliver Puncken, Gabriel Pelegrina, David Mendoza (El Chingón!) and Andreas Wienke for the priceless support they provided, not only professional but also personal.

I'd like to make a special mention to Dr. Michele Punturo, Dr. Elena Cuoco and Dr. Erika Morucci for their conscientious work, that led to the success of the GraWIToN project.

I want to thank my parents, who have always supported my decisions even when they didn't understand them very well. This thesis is the result of a very long-term project that they initiated. And to my sister Iris, whose courage and tenacity are a truly role model.

Last but not least, I don't find the words to thank Sara for what she has given me these years. She has been always by my side, making my life and myself better, and inspiring me every single day.

